2017

SEMICONDUCTOR PHOTOCATALYSIS: MECHANISMS, PHOTOCATALYTIC PERFORMANCES AND LIFETIME OF REDOX CARRIERS

Ruixin Zhou

University of Kentucky, ruixin.zhou@uky.edu
Author ORCID Identifier:
https://orcid.org/0000-0002-2405-4893
Digital Object Identifier: https://doi.org/10.13023/ETD.2017.394

Recommended Citation

SEMICONDUCTOR PHOTOCATALYSIS: MECHANISMS, PHOTOCATALYTIC
PERFORMANCES AND LIFETIME OF REDOX CARRIERS

DISSERTATION

A dissertation submitted in partial fulfillment of the requirements for
the degree of Doctor of Philosophy in the College of Arts and Sciences
at the University of Kentucky

By

Ruixin Zhou

Lexington, Kentucky

Director: Dr. Marcelo Guzman, Associate Professor of Chemistry

Lexington, Kentucky

2017

ABSTRACT OF DISSERTATION

SEMICONDUCTOR PHOTOCATALYSIS: MECHANISMS, PHOTOCATALYTIC PERFORMANCES AND LIFETIME OF REDOX CARRIERS

Photocatalytic reactions mediated by semiconductors such as ZnS, TiO_2, ZnO, etc. can harvest solar energy into chemical bonds, a process with important prebiotic and environmental chemistry applications. The recycling of CO_2 into organic molecules (e.g., formate, methane, and methanol) facilitated by irradiated semiconductors such as colloidal ZnS nanoparticles has been demonstrated. ZnS can also drive prebiotic reactions from the reductive tricarboxylic acid (rTCA) cycle such as the reduction of fumarate to succinate. However, the mechanism of photoreduction by ZnS of the previous reaction has not been understood. Thus, this thesis reports the mechanisms for heterogeneous photocatalytic reductions on ZnS for two model reactions in water with sulfide hole scavenger. First the reduction of CO_2 is carried out under variable wavelength of irradiation and proposed to proceed thorough five steps resulting in the exclusive formation of formate. Second the reduction of the double bond of fumaric acid to succinic acid is reported in detail and compared to the previous conversion of CO_2 to formic acid. Both reactions are carried out under variable wavelength of irradiation and proposed to proceed thorough one electron transfer at a time. In addition, a new method to measure the bandgap of colloidal ZnS suspended in water is established. Furthermore, the time scales of electron transfer and oxidizing hole loss during irradiation of ZnS for both reactions are reported and interpreted in terms of the Butler-Volmer equation.

The sunlight promoted production of succinate introduced above, provides a connection of this prebiotic chemistry work to explore if central metabolites of the rTCA cycle can catalyze the synthesis of clay minerals. Clay minerals are strong adsorbents that can retain water and polar organic molecules, which facilitate the polymerization of biomolecules and conversion of fatty acid micelles into vesicles under prebiotic conditions relevant to the early Earth. While typical clay formation requires high temperatures and pressures, this process is hypothesized herein to be accelerated by central metabolites. A series of synthesis are designed to last only 20 hours to study the crystallization of sauconite, an Al- and Zn-rich model clay, at low temperature and ambient pressure in the presence of succinate as a catalyst. Succinate promotes the formation of the trioctahedral 2:1 layer silicate at $\geq$ 75 °C, $6.5 \leq pH \leq 14$, [succinate] $\geq$

0.01 M. Cryogenic and conventional transmission electron microscopies, X-ray diffraction, diffuse reflectance Fourier transformed infrared spectroscopy, and measurements of total surface area and cation exchange capacity are used to study the time evolution during the synthesis of sauconite.

While the studies with ZnS presented above advanced the fundamental understanding of photocatalysis with single semiconductors, the environmental applications of this material appear limited. A common limitation to photocatalysis with single semiconductors is the rapid recombination of photogenerated electron-hole pairs, which reduces significantly the efficiency of the process that in the case of ZnS also suffers from photocorrosion in the presence of air. In order to overcome the fast charge recombination and the limited visible-light absorption of semiconductor photocatalysts, an effective strategy is developed in this work by combining two semiconductors into a nanocomposite. This nanocomposite is solvothermally synthesized creating octahedral cuprous oxide covered with titanium dioxide nanoparticles (Cu_2O/TiO_2). The nanocomposite exhibits unique surface modifications that provide a heterojunction with a direct Z-scheme for optimal CO_2 reduction. The band structure of the nanocomposite is characterized by diffused reflectance UV-visible spectroscopy, X-ray photoelectron spectroscopy (XPS) and ultraviolet photoelectron spectroscopy. The photoreduction of $CO_2(g)$ to $CO(g)$ on the nanocomposite is investigated in the presence water vapor as the hole scavenger that generates the quantifiable hydroxyl radical ($HO^\bullet$). The quantum efficiency of CO production under irradiation at $\lambda \geq 305$ nm with the nanocomposite is 2-times larger than for pure Cu_2O. The detection of $HO^\bullet$ and XPS analysis contrasting the stability of Cu_2O/TiO_2 vs Cu_2O during irradiation prove that TiO_2 prevents the photocorrosion of Cu_2O.

Overall, the studies of photocatalytic reductions on single component semiconductors reveal new knowledge needed for developing future photocatalytic application for fuel production, wastewater treatment, reducing air pollution, and driving important prebiotic chemistry reactions. Furthermore, the design of a photocatalyst operating under a Z-scheme mechanism provides a new proof of concept for the design of systems that mimic photosynthesis. Finally, this work also demonstrates how molecules obtained by mineral mediated photochemistry can catalyze clay formation; highlighting the important role that photochemistry may have played for the origin of life on the early Earth and other rocky planets.

KEYWORDS: semiconductor, photocatalysis, CO_2 photoreduction, rTCA cycle, sauconite, heterojunction.

Student's signature: <u>Ruixin Zhou</u>

Date: <u>August 31, 2017</u>

SEMICONDUCTOR PHOTOCATALYSIS: MECHANISMS, PHOTOCATALYTIC
PERFORMANCES AND LIFETIME OF REDOX CARRIERS

By

Ruixin Zhou

Dr. Marcelo I. Guzman
Director of Dissertation

Dr. Mark A. Lovell
Director of Graduate Studies

08/31/17

TABLE OF CONTENTS

LIST OF TABLES

LIST OF FIGURES

LIST OF SCHEMES

Chapter 1 Introduction

1.1 Background

Two of the most important challenges faced by society now and for the next 50 years are the shortage of energy supply and the severe emission of environmental pollution.[1] According to estimates, nonrenewable fossil fuels including coal, oil, and natural gas account for ~80% of the total global energy supply, as depicted in Figure 1.1.[1] The burning of fossil fuels is a major source of pollutants that contributes to smog, acid rain, climate change, and other health, environmental and economic concerns.[1] Pollutants that come from the combustion of fossil fuels include carbon dioxide (CO_2), sulfur dioxide (SO_2), nitrogen oxides (NO_X), and a number of other species.

Carbon dioxide contributes largely to global climate change because it is one of the main greenhouse gases that are present in the atmosphere. It takes part in raising the global temperature through absorption of infrared light and re-emitting it back to the Earth. In 2014, global CO_2 emissions from fossil fuel use into the atmosphere were 35.9 gigatonnes (Gt).[2] Based on the report from National Oceanic and Atmospheric Administration (NOAA) Mauna Loa Observatory in Hawaii, the concentration of atmospheric CO_2 has been increasing steeply from 1958 (~ 315 ppm) to 2017 (400 ppm). The last report from the Intergovernmental Panel on Climate Change (IPCC) has predicted that the atmospheric concentration of CO_2 could reach up to 590 ppm by the year of 2050 and the global mean temperature would rise by 1.9 ºC.[3] As energy generation by fossil fuel combustion dominates CO_2 emission, fossil fuel will be inevitably depleted. Therefore, it is urgent to find clean, renewable, cheap, and

1

sustainable energy sources to replace fossil fuels, mitigate the effect of global warming and satisfy the increased energy demand.[1]
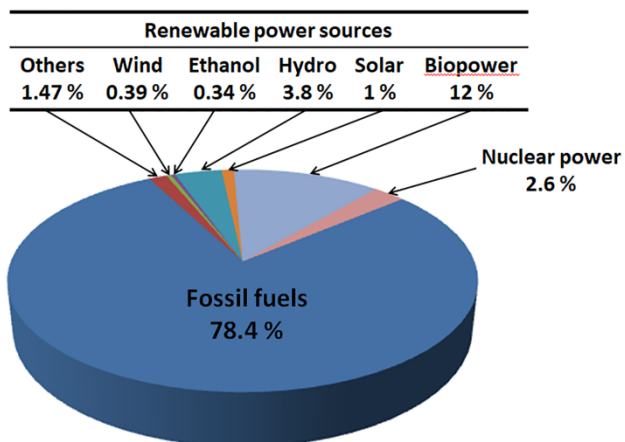
Figure 1.1 Total world energy consumption by source (2014).[1]

1.2 Semiconductor Photocatalysts

In response to satisfying present and future global energy demands, and to address environmental issues associated with the use of fossil fuels, semiconductor photocatalysis has attracted much attention because it can recycle CO_2 into highly energetic compounds such as formate ($HCOO^-$), methane (CH_4), methanol (CH_3OH), and ethanol (CH_3CH_2OH) by using solar energy. In semiconductor photocatalysis, the basic operating mechanism can be broken down into three steps: (1) the formation of photogenerated electron-hole pairs, (2) interfacial electron transportation, (3) and chemical reactions to convert primary redox intermediates into the final products.[4] As shown in Scheme 1.1, the photoexcitation of a semiconductor is initiated by the absorption of photons with equal or greater energy than its bandgap energy (E_{BG}). Then, the electrons are excited from the valence band (VB), the highest energy band occupied by electrons, to the

conduction band (CB), the lowest energy band with no electron on the ground state.[5] The electrons and holes can undergo recombination and release heat. Alternatively, the electrons can migrate to the surface of the semiconductor and react with surface adsorbed species (e.g. CO_2), if recombination happens slower than the reactions of interest.[6] The rates for transferring charge carriers to CB and VB are in competition with the rate of electron-hole pair separation. If the electrons can be utilized by the acceptor efficiently, the rate of the reaction will be faster.
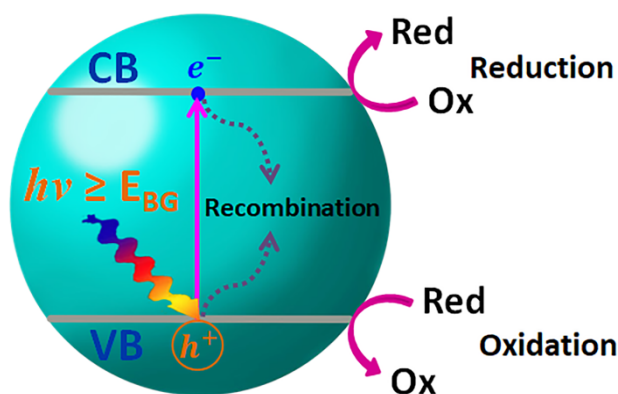
Scheme 1.1 Mechanism for photocatalytic reduction and oxidation processes on the surface of heterogeneous photocatalyst.

The photoreduction of CO_2 is a complicated and thermodynamically unfavorable process because it requires a high reduction potential to reduce the linear-shaped CO_2 to bent $CO_2^{\bullet-}$ ($E°$ ($CO_2/CO_2^{\bullet-}$) = -1.90 eV).[7] Although a single electron transfer to CO_2 is energetically unfavorable, it is a preferred pathway for a proton-assisted transfer for multiple electrons.[8] Scheme 1.2 shows some examples of CO_2 photoreduction using semiconductor photocatalysts.[8] Among all of these semiconductors, ZnS exhibits excellent reduction potential on its conduction band (E_{CB} = -1.04 eV),[9] which is sufficient for CO_2 photoreduction. The valence band energy (E_{VB}) of ZnS is 2.56 eV,[9] which is

sufficiently energetic to oxidize a range of inorganic and organic molecules. The reported E_{BG} of ZnS is 3.59 eV (λ = 345 nm), and the value can be varied in the range of 3.71 $\pm$ 0.13 eV (λ = 334 $\pm$ 12 nm) based on different physical properties.[9] ZnS is a low cost semiconductor that naturally occurs as mineral-sphalerite and -wurtzite. It is stable compared with Cu_2O, which easily undergoes photocorrosion to either Cu(0) or Cu(II). Also, ZnS is environmentally less toxic compared to CdS.[10] There are a few studies focused on the photoreduction of CO_2 using colloidal ZnS suspension as the photocatalyst by harvesting sunlight. The major products are $HCOO^-$, CO(g), and CH_3OH, depending on the different experimental conditions.[11-12] However, the mechanism of CO_2 reduction has never been deeply investigated. For example, one could wonder whether CO_2 accepts two electrons sequentially from the conduction band of a photoexcited semiconductor to form $HCOO^-$ through $CO_2^{\bullet-}$ as an intermediate, or if it takes two electrons at once to generate $HCOO^-$ directly. Another important problem that has been ignored relates to the time scale of redox processes: how fast are electrons transferred to an acceptor on the surface of a photoexcited semiconductor? Is electron transfer from the conduction band faster than the loss of valence band holes? In order to tackle these problems, sphalerite ZnS is chosen as a model semiconductor to study the mechanism of photocatalytic reductions. The work in chapter 2 presents the fundamental aspects of photoreduction reaction of CO_2 on ZnS colloidal suspension in the presence of sodium sulfide (Na_2S) hole scavenger.[9] The study develops a new method to measure the bandgap of a semiconductor suspended in a solvent by measuring the rate of reaction under irradiation at different wavelengths. The reactive species during photoirradiation are explored under different pH values. The quantum yield of formate production

(Φ_{HCOO^-}) under continuous irradiation at $\lambda = 330$ nm is reported. Finally, the lifetimes of redox carriers during the photocatalytic reaction are characterized by studying the dependence of Φ_{HCOO^-} on different initial concentration of Na_2S under periodic irradiation at $\lambda = 330$ nm.
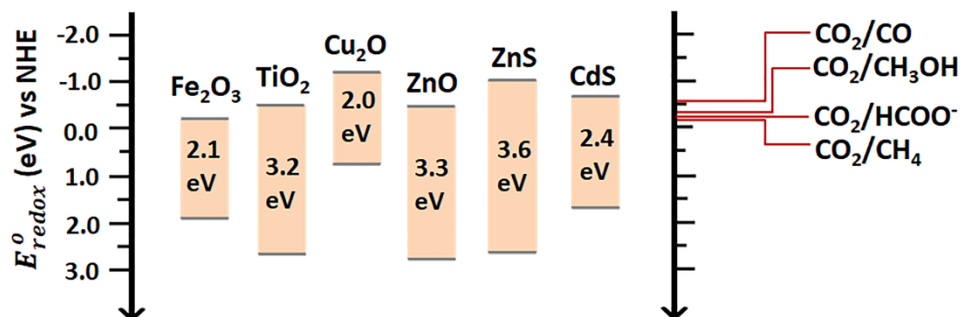
Scheme 1.2 Conduction band, valence band potentials, and bandgap energies of various semiconduction photocatalysts relative to the redox potentials at pH = 7 of energetic semiconductors of interest for CO_2 reduction.[8]

1.3 Photocatalysis and Prebiotic Chemistry

In addition to the energy and environmental applications discussed above, prebiotic chemists have found that semiconductor photocatalysis may play a crucial role in cycling small organic molecules that are essential for the origin of life.[13-17] How prebiotic metabolic systems could have evolved and functioned before the emergence of enzymatic networks remains a critically important challenge in the context of the origin of life.[14] Some prebiotic cycles are considered as necessary platforms to develop more advanced biotic systems. For example, the reductive tricarboxylic acid (rTCA) cycle has attracted much attention because it provides an important central biosynthetic pathway that fixes CO_2 into carboxylic acids.[14] It has been proven that mineral ZnS can drive some reductions of the rTCA cycle in the presence of reduced sulfide species.[14] Of the five

reduction reactions tested using ZnS as a model mineral semiconductor, the conversions of oxaloacetate to malate, fumarate to succinate, and 2-oxoglutarate to oxalosuccinate, were accomplished with 75 %, 95 %, and 2.5 % efficiency, respectively.[14] However, the mechanisms of these photocatalytic reactions remain unknown, demanding an explanation that could provide clues to overcome the negative results for the conversions of succinate to 2-oxoglutarate and oxalosuccinate to isocitrate. Therefore, the work in chapter 3 investigates the mechanism of photoreduction of fumarate to succinate on irradiated ZnS in the presence of Na_2S hole scavenger. The E_{BG} of ZnS colloids suspended in water is determined by measuring the rate of succinate production (R_S) under irradiation at different wavelengths ($\lambda_{cut-off}$), the method that has been developed during the previous work of CO_2 reduction.[9] The primary electron acceptor during the photocatalytic reaction is studied by measuring the dependence of R_S on pH. The lifetimes of the redox carriers are studied and compared with previous CO_2 reduction under identical experimental conditions based on the measurement of the apparent quantum yield of succinate production (Φ_S) at $\lambda = 325 \pm 20$ nm under periodic illumination with variable initial concentration of Na_2S. The outcome of this work provides a better understanding of the possible pathways that prebiotic metabolism emerged through photocatalysis by semiconductor.[18]

1.4 Clay Minerals and the Origin of Life

The work in chapters 2 and 3 demonstrates the connection of semiconductor photocatalysis and prebiotic chemistry and that succinate can be formed on ZnS by sunlight.[18] The following work in chapter 4 has been focused on the association of the prebiotic rTCA cycle and the formation of clay minerals. The potential role of clay

6

minerals in the origin of life has been the subject of ongoing debate for the past several decades. As strong adsorbents, clay minerals can retain water and polar organic molecules.[19-20] It has been proven that clay minerals (e.g. montmorillonite) can lead the polymerization of complex biomolecules like RNA from nucleotides, and the conversion of fatty acid micelles into vesicles on the early Earth.[21-22] Thus, learning the process of clay formation can help to understand the possible roles of these minerals in the origin of life. In general, clay formation requires high temperature (> 1000 °C) and pressure (> 20 atm).[19] Importantly, chapter 4 reveals that clay formation can proceed by photogenerated central metabolites of the rTCA cycle. Central metabolites such as succinate are used as the catalyst to synthesize sauconite, an Al- and Zn-rich, trioctahedral 2:1 layer silicate from a silicate gel at 90 °C and 1 atm in only 20 hours. Experiments are designed to enhance nucleation and accelerate the formation of sauconite by optimizing the synthesis conditions at different temperature, pH, and catalysts with variable concentrations. Cryogenic and conventional transmission electron microscopies, X-ray diffraction, diffuse reflectance Fourier transformed infrared spectroscopy, and measurements of total surface area and cation exchange capacity are performed to fully characterize sauconite, and study the process of crystallization of clay formation.[23]

1.5 Photocatalysis with a Heterostructured Semiconductor

One of the major challenges of using a single semiconductor for photocatalytic reactions is the low product yield due to the rapid recombination of photogenerated electron-hole pairs, which significantly limits the energy-conversion efficiency. Effective strategies for improving photocatalytic activity and visible light absorption have been proposed by combining the semiconductor properties of two (i.e., *p*- and *n*-type)

materials or introducing structural modifications by doping and coating with a metal such as α-Fe_2O_3/Cu_2O[24] and TiO_2/CdS[25] to develop a heterojunction.

Among the numerous heterojunction photocatalysts, the *p-n* heterostructured system with a staggered (Type II) band alignment has attracted much attention because of their efficient charge separation.[26] Common mechanisms for interfacial charge across the *p-n* junctions of Type II heterojunctures are 1) double-charge transfer, in which the photogenerated electrons transfer downhill to one semiconductor with less negative CB while holes transfer to one with less positive VB; 2) Z-scheme type, in which the charge transfer directly quenches the less energetic reductive electrons and oxidative holes. Compared to the Z-scheme mechanism, the double-charge transfer mechanism is less favorable because it leads to the CB with less reduction potential for CO_2 reduction. Z-schemes have been reported including various photocatalytic reactions with water splitting, hydrogen evolution, and pollutant degradation.[24, 27-29] However, Z-scheme systems for CO_2 reduction have been scarcely reported. Apart from the Z-scheme, most photocatalyst materials contain metal complexes that are easily oxidized, resulting in poor stability and decreased efficiency of reduction. Therefore, it is highly desirable to design novel Type II heterostructures with a Z-scheme to improve the energy-conversion efficiency and stability of photocatalysts. Transition metal oxides have been commonly used for photocatalytic applications.[24] For example, Cu_2O is a *p*-type semiconductor (E_{BG} = 2−2.2 eV) that absorbs light up to 600 nm.[24] The narrow bandgap coupling with its energetic conduction band (E_{CB} = −1.4 eV)[24] makes it an excellent candidate as a photocatalyst[30] or co-catalyst[31-32] for CO_2 reduction. Unfortunately, Cu_2O is easily oxidized and photocorroded. An effective way to address this issue is to couple Cu_2O

with an *n*-type semiconductor such as TiO_2 to construct a direct Z-scheme electron transfer.

Besides the interfacial charge transfer, the intrinsic physical and chemical properties of semiconductors such as bandgap, band edge positions and morphology can also affect the photocatalytic performance of these materials. For heterojunction semiconductors, it is important to determine the conduction and valence band offsets, which directly affect the charge carrier separation and localization.[33] However, the interface band alignment of henterojunction studies have barely been reported. In chapter 5, p-type Cu_2O and n-type TiO_2 are chosen as components to design an efficient photocatalyst for CO_2 reduction. Type II heterostructured Cu_2O/TiO_2 photocatalyst is synthesized by a solvothermal method and its photocatalytic performance for CO_2 reduction to produce CO in the presence of water vapor is evaluated under irradiation ($\lambda \geq 305$ nm). The band alignment of the nanocomposite is characterized by diffuse reflectance UV-visible spectroscopy, X-ray photoelectron spectroscopy (XPS) and ultraviolet photoelectron spectroscopy. The quantum efficiency of CO production under irradiation at $\lambda \geq 305$ nm and the stability of the nanocomposite during the photocatalytic reaction are studied. Compared to pure Cu_2O, the synthesized Cu_2O/TiO_2 exhibits highly improved photostability and photocatalytic performance. The enhanced catalytic activity is attributed to the efficient charge separation originated from the Type II band structure, and a Z-scheme charge transfer mechanism is confirmed.[34]

Chapter 2. CO₂ Reduction under Periodic Illumination of ZnS
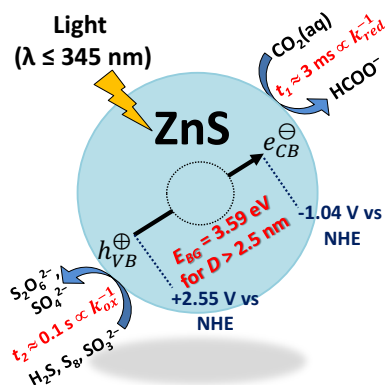
Scheme 2.1 Synopsis TOC

2.1 Synopsis

The photoreduction of CO_2 to formate ($HCOO^-$) in sphalerite (ZnS) aqueous suspensions is systematically studied in the presence of Na_2S hole scavenger. A series of cut-on filters at $\lambda_{cut-on} \geq 280, 295, 305, 320$, and 400 nm is used to measure the reaction rate of formate production. The dependence of the measured reaction rates on λ_{cut-on} indicates that a wavelength of $\lambda = 345$ nm is associated to the actual bandgap of the semiconductor nanocrystallites suspended in water. The results from apparent quantum yield measurements during periodic illumination experiments suggest that 1) valence-band holes on the surface of ZnS disappears within deciseconds due to the oxidation of the scavenger while simultaneously pumping electrons to the conduction band, 2) excited electrons in the conduction band of ZnS are transferred to CO_2 to produce the intermediate $CO_2^{\cdot-}$, 3) $CO_2^{\cdot-}$ abstracts a proton from water and undergoes further photoreduction on the surface of ZnS in an overall timescale for steps 2 + 3 of a few milliseconds. The separation of both process merges at ~29 ms, because it decreases exponentially with a drop in $[Na_2S]$ accompanied by a less negative surface potential. The behavior of the reaction rate at variable pH resembles the fraction of dissolved CO_2, discarding the direct participation of bicarbonate and carbonate in the reaction. Combined chromatographic, mass spectrometry, and spectroscopic studies provide new insights to understand the role of surface chemistry on the photoreduction of CO_2 on ZnS nanocrystals.

2.2 Introduction

Studying the reduction of CO_2 to organic compounds is an interesting problem that attracts the attention of groups that (1) aim to decrease the level of this abundant greenhouse gas in the atmosphere while simultaneously producing fuel feedstock,[35-37] or (2) pursue a mechanism of prebiotic carbon fixation through abiotic reactions.[15, 17, 38] The industrial scale conversion of CO_2 into fuels and the convenience of homogeneous or heterogeneous catalysis have been the subject of recent review articles.[39-40] The photocatalytic reduction of CO_2 in water can mainly produce formate ($HCOO^-$), formaldehyde (H_2CO), methanol (CH_3OH), and methane (CH_4), when semiconductor minerals such as ZnS, ZnO, CdS, or TiO_2 are used.[41-42] Among these minerals, the excellent reduction potential of ZnS, and its low cost of production make it a viable candidate to promote CO_2 photoreduction in the atmospheric optical window. ZnS is a semiconductor, whose oxidizing valence-band holes are not mobile like the reducing conduction-band electrons.[43] A sacrificial reducing agent such as a sulfur containing species, e.g., H_2S or SO_3^{2-}, both available byproducts from coal combustion, can be used to complete the electric circuit of ZnS photocatalyst for the reduction of CO_2 to $HCOO^-$. However, limited progress has been made in this field due to the inertness of CO_2 and thermodynamic impediments. A typical reaction scheme for the photoreduction of CO_2 in ZnS colloidal suspensions involves 1) photoexcitation of ZnS to produce excited electrons (e^-) and positive holes (h^+) (reaction 1), which can be thermally lost (reaction 2), 2) photoexcited holes can be converted by H_2S hole scavenger to sulfate (reaction 3), and finally, 3) adsorbed CO_2 molecules can accept an electron on the surface of ZnS to

produce a radical anion intermediate (reaction 4) that is further reduced to HCOO⁻ (reactions 5):

$$ZnS \xrightarrow{h\nu} e^- + h^+ \tag{1}$$

$$e^- + h^+ \rightarrow heat \tag{2}$$

$$H_2S + 4\,H_2O \xrightarrow{ZnS^*} SO_4^{2-} + 10\,H^+ + 8\,e^- \tag{3}$$

$$CO_2(aq) + e^- \xrightarrow{ZnS^*} CO_2^{\cdot-} \tag{4}$$

$$CO_2^{\cdot-} + H^+ + e^- \xrightarrow{ZnS^*} HCOO^- \tag{5}$$
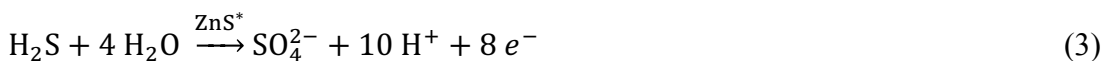
The initial reduction of CO_2 proceeds through a single electron transfer to produce $CO_2^{\cdot-}$ and is accompanied by a large energy redistribution from a linear molecule to a bent radical anion.[44] The nucleophilic carbon in the surface-adsorbed radical anion abstracts a proton from water, forming a weaker acid-base pair than for the unviable oxygen radical.[44] Finally, the HCOO⁻ radical accepts an electron to produce HCOO⁻.[44] The overall two-electron transfer to convert CO_2 to HCOO⁻ requires a reduction potential E^o = -0.29 V *vs.* the normal hydrogen electrode (NHE) given in Table S1 (Supporting Information). In comparison, the conduction-band electron of ZnS is poised at -1.04 V *vs.* NHE, and the valence-band hole is +2.55 V *vs.* NHE.[45] The bandgap of ZnS is 3.59 eV and varies with physical properties in the range 3.71 ± 0.13 eV (λ = 334 ± 12 nm).[45] Therefore, the theoretical energy input required from light for this surface-mediated reaction is achievable for photons with wavelength $\lambda \leq 345$ nm.

A few previous studies of the photoreduction of CO_2 to HCOO⁻ in aqueous suspensions of cubic ZnS nanocrystals exist.[42, 46-47] However, they have not explored the photocatalytic activity of ZnS deeply. Further work is needed to understand the

significance of this reduction from carbon with oxidation state +IV to +II, and to provide information needed for theoretical studies of ZnS nanoparticles.[48] We report measurements of reaction rates of formate production (R_{HCOO^-}), light intensities (I_o), apparent quantum yields of formate production at $\lambda = 330$ nm (Φ_{HCOO^-}), and simultaneously characterize the mineral during the reaction. Continuous and periodic illumination experiments yield the timescale in which reducing electrons and oxidizing holes of ZnS are transferred. The dependence of the reaction rate on the wavelength of irradiation provides a method to determine the bandgap energy of synthesized colloidal photocatalysts suspended in water. Finally, sulfide photooxidation intermediates and products are identified by high performance liquid chromatography mass spectrometry and Raman spectroscopy, and the effect of pH in the photochemical process is shown to depend on the availability of dissolved CO_2.

2.3 Experimental Details

2.3.1 Catalyst Preparation

Colloidal ZnS suspensions were prepared based on a previous method.[49] The dropwise addition of 100 mL of 50 mM Na_2S (99.1% assay, Sigma Aldrich) to 100 mL of 50 mM $ZnSO_4$ ($ZnSO_4 \cdot 7\ H_2O$, EMD, 99.5% assay) took place under stirring and purging with $N_2(g)$ (UHP, Scott-Gross). Ultrapure water (18.2 MΩ cm, Elga Purelab Flex, Veolia) purged with $N_2(g)$ was used in every step. Sulfide concentrations were determined at 1:100 dilution in a 50% volume of 2 M NaOH (99.3% assay, Fisher Chemicals) using a sulfide ion selective electrode (Thermo, Orion 94-16). The potentiometric titration with a 0.1000 M $Cd(NO_3)_2$ standard (cadmium nitrate

14

tetrahydrate, Aldrich $\geq$ 99.0 %) was used to standardize the sulfide stock employed in calibration curves. The ZnS colloidal suspension was centrifuged at 4400 rpm for 5 min (Eppendorf 5702) and rinsed twice with water to remove excess sulfate prior to irradiation.

2.3.2 Catalyst Characterization

Hydrodynamic particle size distributions and zeta potential (ζ) measurements were determined at variable pH using a DLS apparatus and ZetaPlus zeta potential analyzer (90 Plus/BI-MAS, Brookhaven Instruments). For pH adjustment, 1 mL of fresh ZnS supernatant was diluted in 70 mL of 1 mM Na_2S solution to bring the pH to 12, and then 0.02 M HCl (EMD Chemicals, GR ACS) was used to adjust the pH of ZnS suspensions. Undiluted samples were used for different measurements of ζ under variable $[Na_2S]$ at pH = 7.0. The surface potential of ZnS is taken as equivalent to ζ for unchanged permittivity and viscosity in the electrical double layer.[50-51]

The absorption spectrum of scattering ZnS in water was obtained with a UV-visible spectrophotometer (Evolution 220, ISA-220 accessory, Thermo Scientific) using a built-in 10 mm silicon photodiode with a 60 mm Spectralon sphere. A 10-mm thick fused silica cuvette with water was used in the reference compartment in combination with a 1-mesh filter to subtract the background. The ISA-220 accessory was used in an alternative configuration to register the diffuse reflectance spectrum of dry ZnS powder as a Kubelka-Munk function against the certified Spectralon standard.

2.3.3 Photochemical Experiments

The colloidal suspensions for the photochemistry experiments were prepared just prior to use as indicated above. The addition of 0.5 mL saturated Na_2S stock solution provided the valence-band hole scavenger and prevented any adventitious O_2 to enter the reactor. The adjusted Na_2S concentration in the suspension was *ca.* 8 mM, and the loading of ZnS particles was 2.3 g L^{-1}. The suspension pH was adjusted to 7 by bubbling CO_2 (UHP, Scott-Gross) before sealing the vessel containing 200 mL of the suspension. The customized fused silica photochemical apparatus consisted of a 210-mL reaction vessel outfitted with a water jacket held at 288 K (Thermo Scientific bath circulator A25). For irradiation, a collimated 1 kW high-pressure Hg(Xe) arc lamp was used after removing infrared radiation with a water filter (Scheme S1, Supporting Information). Different optical filters (all from Newport) were used when indicated. The high loading of ZnS ensures the maximum saturation of light absorption.[52] The 2.3 g L^{-1} of ZnS used in the photoreactor served as an efficient loading for the suspended particles to absorb more than 99 % of the incident photon rate. The scattered photon rate measured with the detector at angles of 180º (forward scattered light), ±45º, ±90º, and ±135º is below 0.8 % relative to the incident photon rate.

Measurements of the photon flux at 330 nm, performed by ferrioxalate actinometry,[53-54] were used to normalize the output of a calibrated air-cooled thermopile detector (Newport Corporation Model 818P-010-12) connected to an optical power meter (Newport Corporation Model 1918-C). This procedure has been previously demonstrated,[54-55] and made possible the use of the detector to measure the light intensity of individual experiments. Factory calibration of the thermopile performed at 1064 nm

using NIST standards assures a linear response of the detector within a 4.0% error for the interval $190 \leq \lambda \leq 2100$ nm, which is automatically adjusted by a correction factor preloaded in the meter program. The values of Φ_{HCOO^-} at $\lambda = 330$ nm were calculated from measurements of R_{HCOO^-} and I_0 using a series of filters: (1) a neutral density filter transmitting only 34% of the light, (2) a broad band optical filter absorbing in the infrared, (2) a cut-on filter at 320 nm, and (4) a band-path filter transmitting only $\lambda = 330 \pm 10$ nm. Because the measurements do not account for photon scattering, Φ values are lower limits of the quantum yields.[56] The generation of light pulses was possible by means of a combined mechanical shutter and optical chopper (Newport 75159) set by a controller (Newport model 75160) with three different blades (models 75162, 75163 and 75164). The shutter mode was used for pulsing between 0.02 and 0.5 Hz (1–25 s on period), and the chopper mode for the 10 and 2400 Hz regime (0.208–50 ms on period). A second chopper and controller (SRS model SR540) was used for pulsing in the intermediate range, between 1 and 10 Hz (0.05–0.5 s on period).

2.3.4 Analysis of Products

After irradiation for a selected time period, 5 mL of suspension was withdrawn from the reaction vessel through a septum, centrifuged (5 min at 4400 rpm), and the supernatant was filtered (IC Acrodisc 0.2-µm pore size; Pall Corp.). Analyses of products in the filtrate and in samples processed by solid-phase extraction (Hypersep C18, 1 mL, 100 mg) were performed by ion chromatography (IC). The second water eluent fraction of SPE cartridges preconditioned with water and methanol were injected with an autosampler (Dionex AS) into the IC system (Dionex ICS-2000). The IC was equipped with an IonPac AS11-HC analytical column (2 × 250 mm), an IonPac AG11-HC guard

column (2 × 50 mm), an ASRS-300 (2-mm) suppression module, an eluent generator (EGC III) with KOH cartridge, an anion trap column (CR-ATC), and a conductivity detector used to match the retention times of standards. The gradient separation applied a flow of 0.38 mL min^{-1} with an initial mobile phase of 1 mM KOH for 8 min followed by three linear increases of 1) 1.4 mM min^{-1} up to 15 mM, 2) 1.5 mM min^{-1} up to 30 mM, and 3) 3 mM min^{-1} up to 60 mM. After IC separation, a mass spectrometer detector (Thermo MSQ Plus) interfaced with an electrospray ionization (ESI) probe (450 °C and 70 psi N_2 nebulizing gas, 1.9 kV needle voltage, and 50 V cone voltage, operated in the negative mode) identified the mass-to-charge ratio (*m/z*) of species. An auxiliary pump (Lab Alliance) provided a flow of 0.12 mL min^{-1} methanol (Fisher Optima) mixed through a T connector with the eluent flow before aerosolization in the ESI chamber. Chromeleon and Excalibur software were used to control and process data from both systems. Concentrations were obtained from calibration curves and/or using the method of standard addition. Standards included solutions of sodium formate (Acros Organics, 99%), sodium sulfite (Fisher Chemicals, 99.9% assay) in 1 % methanol, sodium sulfate (Fisher Chemicals, 99.9% assay), and sodium thiosulfate (EM Science, 97% assay).

Sulfide concentrations were potentiometrically quantified with the calibrated sulfide ion selective electrode described above. The decay of sulfide was monitored during periodic illumination experiments at λ = 330 nm to extract the decay rate constant (k_{-H_2S}). Samples withdrawn from the reactor were immediately centrifuged at 4400 rpm for 5 min, and the supernatant was treated with an equal volume of 2.0 M NaOH. The time series of sulfide decay followed first-order kinetics with correlation coefficients $r^2 \geq$ 0.990.

2.4 Results and Discussion

2.4.1 ZnS Characterization

The characterization of the aqueous suspensions of ZnS by dynamic light scattering (DLS), measurements of zeta potential (ζ), and the UV-visible absorption spectrum included below provides direct information to understand the surface photoreactions of interest. The findings in this paper indicate that surface species dominate the reduction of CO_2 and the oxidation of the hole scavenger.

Noninvasive DLS reports particle sizes such as those present during the experiments in aqueous conditions (Figure 2.1), avoiding filtering and drying preparation steps needed in XRD and TEM, which could result in the oxidation and change in the surface charge of ZnS. The effect of acidification on particle size and surface charge in ZnS colloidal suspensions –sequential addition of acid reduced the pH of these suspensions from 12.0 to 2.3– is also shown in Figure 2.1. The measurements applied DLS to compare the diffusion of particles in the colloidal suspension. In addition, the crystallite size D from the XRD pattern (Figure S2.1, Supporting Information) and transmission electron microscopy (TEM) images are not exactly the same of the particle size obtained by DLS (Figure 2.1) because ZnS particles in suspension are made up of several different crystallites.
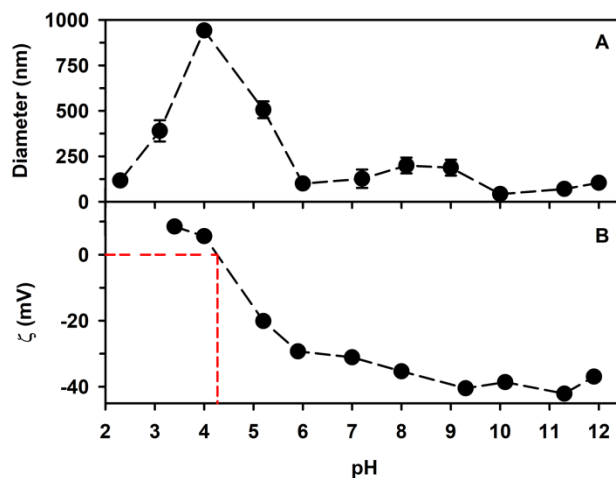
Figure 2.1. (A) Particle size distribution (diameter) and (B) zeta potential (ζ) of synthesized ZnS colloidal suspensions at 20 °C and variable pH.

The intensity correlation function of each sample was measured over three runs at a scattering angle of 90° from the incident laser (λ = 658 nm) beam. Particles with size between 35 and 950 nm were detected at pH 10 and 4, respectively (Figure 2.1A). The particle size is described by a unimodal distribution for the whole pH-range. The synthesized ZnS at 20 °C initially experiences slight changes of aggregate size but the distribution remains unimodal with diameters of 40-200 nm down to pH 5.9. It should be noted that further acidification led to considerable larger particles for the pH range 3.1-5.1, and peaks at pH = 4.0 to a value of 940 nm. No considerable difference in the particle size distribution was observed for ZnS synthesized at 5, 20, or 40 °C.

The negative values for the zeta potential in Figure 2.1B with magnitude larger than the boundary of -30 mV, in the range of pH 7.0-12.0, indicate that the particles of ZnS repeal each other and there is no tendency to flocculate. As the pH drops below 5.9 the suspension becomes less stable, the zeta potential becomes increasingly less than -30 mV, thus there is no force to prevent the particles coming together and flocculation occurs. The continuous addition of dilute HCl eventually neutralizes the negative charge at the

isoelectric point of pH = 4.2 ± 0.1 obtained by interpolation (red dashed line in Figure 2.1B). Further addition of acid results in a buildup of positive charge. For the syntheses at 5 and 40 °C, the isoelectric point is within the ±0.1 range of pH measured at 20 °C.

The characterization of dry ZnS by other techniques could be affected by processes occurring in bulk and aggregated catalyst. This information for X-ray diffraction (XRD) patterns (Figure S2.1, Supporting Information) and Raman spectroscopy (Figure S2.2, Supporting Information) during the reaction, transmission electron microscopy (TEM) and energy-dispersive X-ray spectroscopy (EDS) (Figure S2.3, Supporting Information), and Brunauer-Emmett-Teller (BET) measurements can be found in the accompanying Supporting Information document.

2.4.2 Identification of Products

Figure 2.2 shows the species identified as anions in the chromatogram for irradiation at $\lambda > 200$ nm. Peaks elute in the following order: Formate ($HCOO^-$, $m/z = 45$), bicarbonate (HCO_3^-, $m/z = 61$), bisulfite (HSO_3^-, $m/z = 81$), bisulfate (HSO_4^-, $m/z = 97$), hydrogen thiosulfate ($HS_2O_3^-$, $m/z = 113$), and hydrogen dithionate ($HS_2O_6^-$, $m/z = 161$). The same products were observed for irradiation with the different cut-on filters ($\lambda_{cut-on} \geq$ 280, 295, 305, 320) and for monochromatic light ($\lambda = 330$ nm). Control experiments that demonstrate the heterogeneous photoproduction of formate on the surface of the ZnS semiconductor were carried out in the presence of one or more of colloid (ZnS), ultraviolet light (hv; $\lambda > 200$ nm), carbon dioxide (CO_2), and sulfur-based hole scavenger (S_T). In the absence of ZnS, there is no production of formate (control A). The negative result for the production of formate under dark conditions (control B) indicates that a thermal mechanism is not the cause of this reaction. No formate production was observed

unless CO_2 as an electron acceptor (control C) and sulfide hole scavenger as an electron donor (control D) were present.
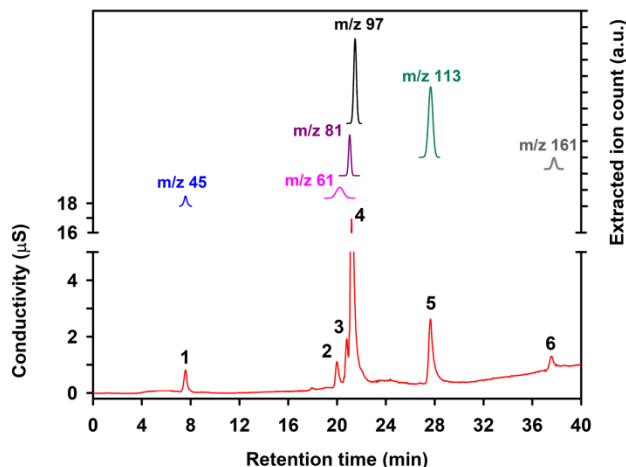
Figure 2.2 Ion chromatogram of a sample photolyzed ($\lambda > 200$ nm) during 1.5 h showing peaks of (1) formate ($HCOO^-$, m/z = 45), (2) bicarbonate (HCO_3^-, m/z = 61), (3) bisulfite (HSO_3^-, m/z = 81), (4) bisulfate (HSO_4^-, m/z = 97), (5) hydrogen thiosulfate ($HS_2O_3^-$, m/z = 113), and (6) hydrogen dithionate ($HS_2O_6^-$, m/z = 161).

The oxidation of sulfide hole scavenger during the reaction also produces a small amount of yellow colloid visually observed during irradiation and identified as elemental (rhombic) sulfur, S_8, in the Raman spectrum (Figure S2.2, Supporting Information).[57] This species is not derived from the catalyst that remains intact as shown by XRD and TEM data (Supporting Information). Rhombic sulfur is as an oxidation intermediate produced by the sulfide hole scavenger. The simultaneous photooxidation and substitution mechanism below protects the integrity of ZnS, consumes solution-phase sulfide ions in the system, and produces elemental sulfur:[58]

$$ZnS + 2\,h^+ \rightarrow Zn^{2+} + S \tag{5}$$

$$Zn^{2+}S + HS^- \rightarrow ZnS + S + H^+ \tag{6}$$

$$2\,h^+ + HS^- \rightarrow S + H^+ \tag{7}$$

Given the dissociation of H_2S (pK_{a1} = 7.05 and pK_{a2} = 14.92 at 25 °C),[59] both available acidic species at pH = 7 (dissociation fraction α_{H_2S} = 0.53 and α_{HS^-} = 0.47) may participate as initial hole scavenger. However, neutral H_2S should be the main reductant because HS⁻ is repelled by the negatively charged surface of ZnS for higher pH than the isoelectric point of ZnS (pH = 4.2, Figure 2.1). CO_2 is reduced to HCOO⁻ in the conduction band of ZnS, while all involved sulfur species participate in oxidation reactions at the valence band. S_8, $S_2O_3^{2-}$, SO_3^{2-}, and $S_2O_6^{2-}$ (Scheme 2.2) are formed as intermediate products during the oxidation of sulfide towards SO_4^{2-} with the possible transfer of electrons summarized in Table S2 (Supporting Information).
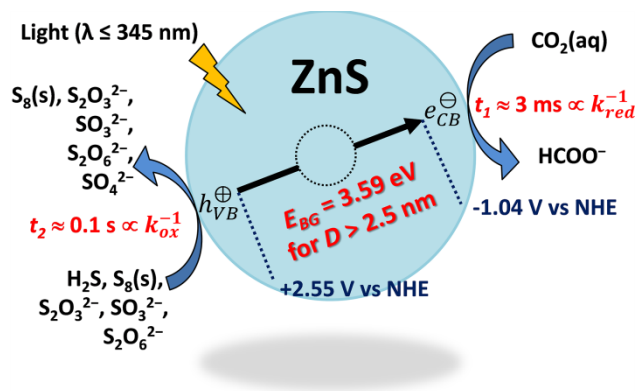
Scheme 2.2 Representation of the heterogeneous photocatalysis on ZnS nanoparticles in water.

$S_2O_3^{2-}$ is assumed to be an oxidation intermediate directly formed at the valence band. S_8 may react with H_2 to regenerate H_2S, while the formation of dithionate ($S_2O_6^{2-}$) may also be the result of SO_3^{2-} oxidation.[59-60] A summary of the redox potentials for some of the reactions observed is given in Table S1 (Supporting Information). The photoexcited state ZnS* can reduce any of the species on the left-hand side of the equations in Table S1, as well as to oxidize any of the species on the right-hand side.

2.4.3 Bandgap from Chemical Measurements and Identification of CO_2 as the Reactive Species

The production of HCOO⁻ vs. time, in the presence of sulfide hole scavenger, is shown in Figure 2.3 These experiments utilized different cut-on filters at wavelengths $\lambda_{cut-on} \geq 280$, 295, 305, 320 and 400 nm. For $\lambda_{cut-on} \geq 400$ nm, no HCOO⁻ production occurred.
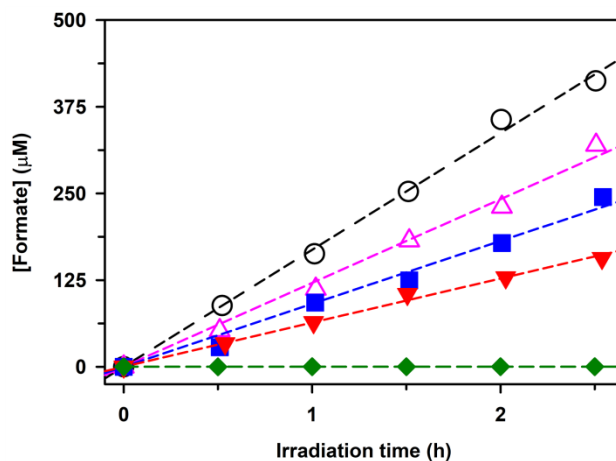
Figure 2.3 Formate production at variable cut-on wavelength of irradiation (λ_{cut-on}). The reaction rate at $\lambda_{cut-on} \geq 280$ (○), 295 (Δ), 305 (■), and 320 nm (▼), is 162.07, 120.29, 95.48, and 63.61 µM h⁻¹, respectively. No formate production observed for $\lambda_{cut-on} \geq 400$ nm (♦).

Upon dissolution of gaseous CO_2 in water at 15 °C (Henry's law constant $K_H =$ $[CO_2(aq)]/P_{CO_2} = 0.0260$ mol L^{-1} atm^{-1} at 15 °C)[61] several species coexist in equilibrium:

$$CO_2(g) \rightleftharpoons CO_2(aq) \tag{8}$$

$$CO_2(aq) + H_2O \rightleftharpoons H_2CO_3 \tag{9}$$

$$H_2CO_3 \rightleftharpoons HCO_3^- + H^+, pK_{a1} = 6.42^{62} \tag{10}$$

$$HCO_3^- \rightleftharpoons CO_3^{2-} + H^+, pK_{a2} = 10.43^{62} \tag{11}$$

and only a negligible amount of all dissolved CO_2 (CO_2(aq) + H_2CO_3) is in the form H_2CO_3. The species present in the previous equilibrium system (Figure 2.4) depend on pH as follows: 1) At pH < pK_{a1} = 6.42 dissolved CO_2 is dominant, 2) at pH > pK_{a2} = 10.43 carbonate is dominant, while 3) for intermediate pH values (pK_{a1} < pH < pK_{a2}) bicarbonate is the main species. The dependance of R_{HCOO^-} on pH. (Figure 2.4) under full lamp irradiation resembles the fraction of total dissolved CO_2 present in equilibrium, indicating that CO_2 is the only species that controls the process. The charged species (HCO_3^- and CO_3^{2-}) are not primary reagents undergoing photoreduction.
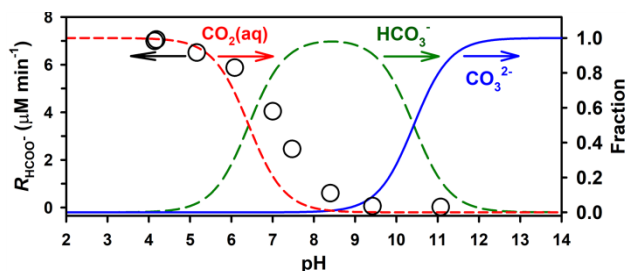
Figure 2.4 Rate of formate production (R_{HCOO^-}) and fraction of dissolved CO_2, HCO_3^-, and CO_3^{2-} present in equilibrium vs. pH at 15 °C.

This observation agrees with a model of reactive surface species adsorbed to the negatively charged surface of ZnS (Langmuir-Hinshelwood mechanism), which prefers the interaction with neutral dissolved CO_2 over the electrostatic repulsion to HCO_3^- and CO_3^{2-} anions. However, an Eley-Rideal mechanism cannot be completely discarded.[63-65]

A narrow particle size distribution is confirmed by the sharp drop observed in the reflectance spectrum of dry ZnS powder with reflection edge at $\lambda = 300$ nm (Figure 2.5). The associated valence band of the dry ZnS powder has a bandgap of 3.76 eV ($\lambda = 330$ nm), which is blue-shifted from the absorption edge of wet (bulk) ZnS at $\lambda = 345$ nm (Figure 2.5). The absorption band edge is centered at $\lambda = 312$ nm in the ZnS suspension in water (Figure 2.5). Although the particles could experience quantum size effects,[66] the experiments take place in water, and the absorption spectrum of ZnS colloidal suspensions is needed to estimate the bandgap energy under actual experimental conditions. The slopes in Figure 2.3 give the R_{HCOO^-} values plotted in Figure 2.5 vs. specific $\lambda_{\text{cut-on}}$ of irradiation. The bandgap of ZnS colloidal suspensions can be better determined from the extrapolated straight line in Figure 2.5.
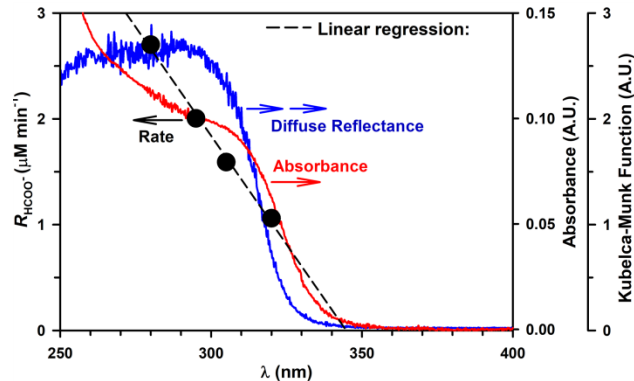
Figure 2.5 Rate of formate production (R_{HCOO^-}) vs. cut-on wavelength of irradiation at pH = 7.0. Absorption spectrum of ZnS in water (red line and internal right axis) and diffuse reflectance spectrum of dry ZnS powder (blue line and external right axis).

This is the first time that such a determination of the bandgap is made based on the measurement of reaction rates and irradiation wavelengths. The equation for the linear regression in Figure 2.5 is R_{HCOO^-} (µM min^{-1}) = 14.152 – 0.0410 × λ_{cut-on}, (nm) with a coefficient of correlation r^2 = 0.995. The reaction rate falls to zero (R_{HCOO^-} = 0) for an extrapolated cut-on wavelength λ_{cut-on} = 345 nm. The value of λ_{cut-on} = 345 nm is in excellent agreement with the absorption spectrum for the ZnS colloidal suspension (red line in Figure 2.5), registered from the supernatant remaining in solution after centrifugation of the 2.3 g L^{-1} ZnS colloidal suspension (DLS yields D = 51 ± 2 nm). Remarkably, the absorption spectrum in Figure 2.5 falls to zero above the same λ_{cut-on}. The bandgap energy for ZnS suspension in water is calculated using the equation $E_{BG} = h\ c\ \lambda_{cut-on}^{-1}$ = 5.74 × 10^{-19} J ≡ 3.59 eV, where h = 6.626 × 10^{-34} J s is the Planck constant, and c = 3.0× 10^8 m s^{-1} is the speed of light. The measured E_{BG} for nanoparticles in water is within the range of previous reports for ZnS[45] and it does not display quantum size effects, as expected for diameters larger than the Bohr radius of ZnS (2.50 nm).[67]

For continuous monochromatic irradiation at $\lambda = 330$ nm, the ratio of $R_{HCOO^-} = 5.92 \times 10^{-9}$ mol L^{-1} s^{-1} to $I_o = 4.10 \times 10^{-7}$ Einstein L^{-1} s^{-1} (measured by actinometry), yields $\Phi_{HCOO^-} = 1.44$ % as a lower limit of the quantum yield, because light is extinguished both by absorption of the photocatalyst and by light scattering from the particles in suspension.[56] This monochromatic Φ_{HCOO^-} should not be compared to those larger values also reported by ferrioxalate actinometry (e.g., for ZnS and MnS)[47, 68] employing broadband irradiation (200-400 nm). Care must also be taken when comparing our measurement to the higher $\Phi_{HCOO^-} = 20$ % at $\lambda = 280$ nm.[69] More importantly, several factors could affect Φ_{HCOO^-} in different experimental setups, making the comparison of Φ_{HCOO^-} by different groups difficult.[70] Particularly, experimental systems could have different 1) intensity of monochromatic illumination, 2) pH, 3) mass transport (e.g., stirring rate in the reactor), and 4) cell geometry.[70] In addition, the structure and associated catalyst properties could vary to considerably affect the observed Φ_{HCOO^-}.[70] For example, whether the experimental preparation skipped the final steps after the synthesis (centrifugation, washing and rinsing of the catalyst with water), the reaction rate at $\lambda = 330$ nm increased to $R_{HCOO^-} = 3.72 \times 10^{-8}$ M s^{-1}, representing a 6.3 times more efficient process with $\Phi_{HCOO^-} = 9.07$ %. The Φ_{HCOO^-} values reported are useful to compare the set of reactions occurring under similar conditions for the specific structure characterized. Overall, the information derived from the Φ_{HCOO^-} values in the section below is of general application to the photocatalyst and enabled the determination of the lifetime of surface redox carriers.

2.4.4 Lifetime of Redox Carriers on the Surface of Photoexcited ZnS

Figure 2.6A shows the changes in Φ_{HCOO^-} (at pH = 7.0) under periodic illumination with alternate and equally lasting bright (τ_L) and dark (τ_D) intervals. In Figure 6A, for the upper limit chopper frequencies examined, $\Phi_{L \to 0}$ merges with the value measured under continuous illumination (Φ_{HCOO^-} = 1.44 %). However, two well-resolved inflexion points are observed when transitioning from $\Phi_{L \to 0}$ to the lower limit chopper frequencies ($\Phi_{L \to \infty}$), which correspond to redox carriers with different reactivity.[71] The two inflexion points fitted with a nonlinear least squares regression for a double sigmoid curve occur at t_1 = 3.3 ms and t_2 = 0.13 s (Figure 2.6A) for $[Na_2S]_o$ = 2.0 mM and pH = 7.0 and can be associated with the transfer of reducing conduction-band electrons and the oxidizing valence-holes acting over sulfide, respectively. Close values of t_1 = 2.4 ms and t_2 = 0.14 s (to those obtained by measuring $\Phi_{HCOO^-} = R_{HCOO^-}/I_o$) are potentiometrically determined from the first-order rate constant for sulfide decay (k_{-H_2S}), a stable species in dark controls (Figure 2.6B).
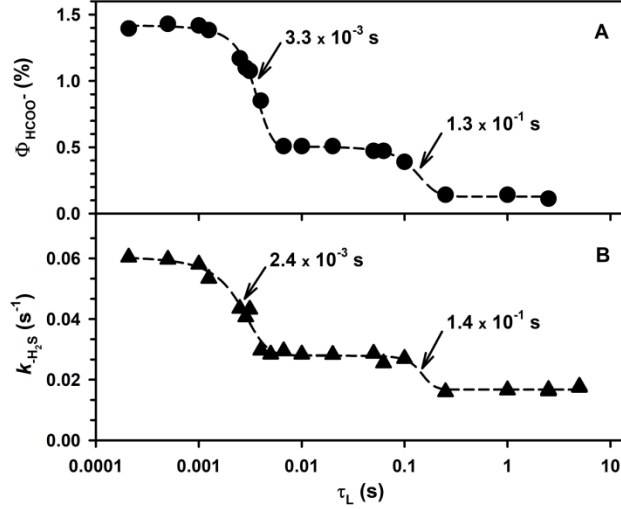
Figure 2.6 (A) Apparent quantum yield of formate production (Φ_{HCOO^-}) and (B) first-order rate constant of sulfide decay k_{-H_2S} vs. the bright interval time under periodic illumination (τ_L) at pH = 7.0 and $[Na_2S]_o$ = 2.0 mM.

Experiments at variable initial $[Na_2S]$ are useful to investigate which transition corresponds to oxidizing and reducing species. The measured surface area of ZnS assures experimental conditions of submonolayer coverage by the hole scavenger for $[Na_2S] < 65$ mM. Both transitions t_1 and t_2 are still observed in the range $0.50 \leq [Na_2S] \leq 16.9$ mM. These experiments provided a method to relate the two transitions with the concentration of the reducing species and the measured surface potential,[50-51, 71-72] by assuming that the Butler-Volmer (BV) equation[50-51, 71-72] holds for illuminated ZnS colloids. The faster photon absorption rate by ZnS than the loss of reducing electrons and oxidizing holes by ZnS* creates an excess redox potential (E) and surface charge. The previous imbalance affects the half-reduction and half-oxidation rate constants of ZnS[39,40] $k_{red} = k_0\, e^{-\left[\frac{\alpha_{red}\, n\, F}{RT}\right](E-E^o)}$ and $k_{ox} = k_0\, e^{\frac{\alpha_{ox}\, n\, F}{RT}(E-E^o)}$, respectively, where E^o is the standard redox potential, R is the gas constant, F is the Faraday constant, T is the absolute temperature, n_{red} and n_{ox} are the number of electrons transferred in each half-reaction, k_0 is the standard heterogeneous rate constant, and α_{red} and α_{ox} are the dimensionless charge

30

transfer coefficients.[71-72] In our experiments, the potential is affected by changing the concentration of the reducing species in the range $0.50 \leq [Na_2S]_o \leq 16.9$ mM, what modifies the surface potential of ZnS (Figure S2.5, Supporting Information) as represented by ζ for unchanged permittivity and viscosity in the electrical double layer.[50-51]

Figure 2.7A shows, as expected, both transitions t_1 and t_2 have opposite trends with increasing $[Na_2S]$. Analogously, Figure 2.7B indicates the same kind of dependance for the transitions on ζ. The experimental information in Figure 2.7A demonstrates how the two photoredox transitions observed are related to the rate constants k_{red} and k_{ox}, which are reciprocal to t_1 and t_2, respectively: $t_1 \propto k_{red}^{-1}$ and $t_2 \propto k_{ox}^{-1}$. Given the previous inverse relationships, and the positive exponential form of k_{ox}, an increase in the concentration of hole scavenger (or the potential) predicts an increase in the value of t_2 with $[Na_2S]$ in Figures 2.7A, and its decrease in Figure 2.7B with ζ. The intersection point of both regression lines in Figure 2.7B predicts that both transitions become undistinguishable for a surface potential of -16 mV at 29 ms. On the contrary, the measured t_1 value decreases with $[Na_2S]$ and increases for larger ζ (Figure 2.7B) due to the negative exponential form describing k_{red}. This interpretation of t_1 being related to k_{red} is in agreement with the recently reported higher rate of reduction for $H_2(g)$ generation in CdS nanocrystals.[73] The higher rate of $H_2(g)$ production observed followed an exponential function for more negative potentials.[73]
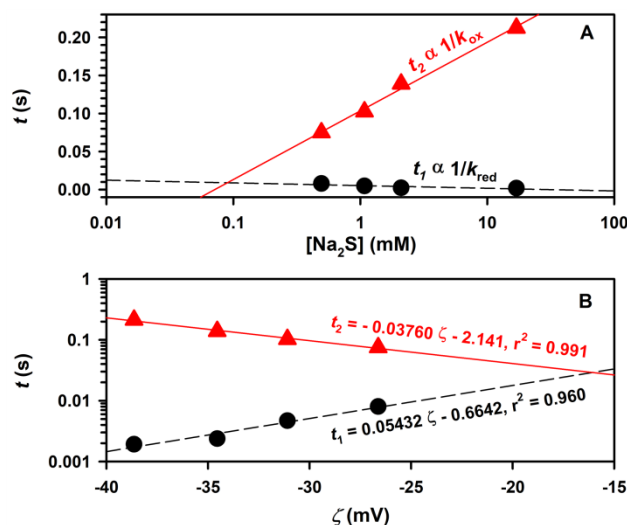
Figure 2.7 Transitions (●) t_1 and (▲) t_2 vs. (A) variable $[Na_2S]_o$ and (B) zeta-potential (ζ). The red and black-dashed lines show the linear least square regressions, which intercept for (A) a coverage of $[Na_2S] = 90$ μM, corresponding to (B) an extrapolated $\zeta = -16$ mV and $t = 29$ ms.

2.5 Conclusions

Remarkably, the reactive intermediates in the photoexcited semiconductor exist for relative long times,[71] as observed here for ZnS*. Characteristic surface carriers remain active for less than 10 and 215 milliseconds for the transfer of mobile electrons and loss of fixed holes, respectively. In other words, the reactive carriers can be detected for longer timescales than the range explored (e.g., 150 fs ≤ $\tau_{1/2}$ < 100 μs)[74] during time-resolved spectroscopy studies of semiconductors. The photoreduction of CO_2 to $HCOO^-$ in aqueous colloidal suspensions of ZnS in the presence of Na_2S, directly consumes dissolved CO_2 as the reactive species adsorbed to the surface of ZnS. A new method to report the bandgap of the semiconductor in the actual hydrated state is demonstrated based on the dependence of the reaction rate on the wavelength of irradiation. The measurement of quantum yields under periodic illumination offers mechanistic information that provides the timescale (10^{-3}–10^{-1} s) of redox processes on the surface of

ZnS, which occur at several orders of magnitude slower than excitation of ZnS. Further studies of this system are underway with the goals of comparing catalyst stability, improving efficiency, and replacing the sacrificial electron donor by other species.

2.6 Acknowledgement

2.7 Supporting Information for CO$_2$ Reduction under Periodic Illumination of ZnS

Additional Results and Discussion

Crystal Structure and Properties of ZnS.

The crystal structure of fresh and photo-processed ZnS dried under vacuum was identified by powder X-ray diffraction (XRD) with a D8 Advance Bruker AXS (Cu K$_\alpha$ radiation, λ = 1.5418 Å) diffractometer. XRD data from 10° to 80° was collected at a scan rate of 1° min^{-1}, background corrected by subtracting the signal of the empty sample holder, and normalized to the maximum sample intensity. In addition of providing confirmation of the crystal structure of dry ZnS by XRD, Raman Spectroscopy was also used (see below). The XRD patterns of the synthesized colloidal particles before and after 1, 2, and 3 hours of irradiation appears to be identical (Figure S2.1A-D). ZnS remains in the pure cubic sphalerite phase for nanocrystallites that produce broad spectral peaks. The peaks at 2θ values of 28.71°, 47.95°, and 56.80° correspond to the respective crystal planes (111), (220), and (311) of faced centered cubic ZnS (JCPDS No. 00-005-0566).
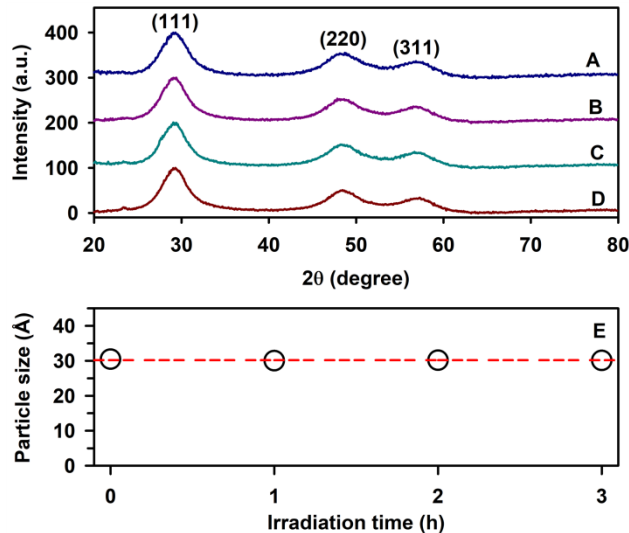
Figure S2.1 XRD patterns for ZnS (A) before and after (B) 1, (C) 2, and (D) 3 hours of irradiation. (E) Particle size vs. irradiation time from Scherrer's equation for the peak at 28.71° (D = 30.19 ± 0.19 Å).

The lattice constant $a = 5.381$ Å calculated from the (111) plane of freshly synthesized ZnS is within the error range of the standard literature value ($a = 5.406$ Å). Applying the Scherrer equation for submicrometer size particles, $D = k \lambda/(\beta \cos \theta)$, to the full width at half maximum (FWHM) of the (111) peak in Figure S2.1A-D, the average grain size of the nanocrystallites is $D = 30.19 \pm 0.19$ Å. The Scherrer constant used is $k = 0.9$, λ is the wavelength of the Cu K_α line applied, β is the FWHM of the peak in radians, and θ is the diffraction angle of the (111) peak. The diameter remains practically constant before and after irradiation (Figure S2.1E). The absence of any wurtzite ZnS structure is expected because this hexagonal phase requires a synthesis at higher temperature and pressure. A comparison of panels A-D in Figure S2.1 indicates that the crystal phase and size of ZnS remains identical during the reaction.

Analysis by nitrogen adsorption–desorption isotherms at 77 K with the Brunauer-Emmett-Teller (BET) method (Micromeritics ASAP 2020 Physisorption Analyzer) was performed for samples before and after 1 h of irradiation with the total output of the UV lamp. Although dry ZnS may not be representative of the actual conditions of the catalyst in water, the small variation of the specific surface area and total pore volume of both samples suggests the system was stable during the reaction. A small 5% change is observed in the BET surface areas for the ZnS colloidal suspensions before (180 m^2 g^{-1}) and after 1 h of UV irradiation (190 m^2 g^{-1}). Similarly, the total pore volume of ZnS remained within a 3% difference before irradiation (0.102 cm^3 g^{-1}) and after 1 h photolysis (0.105 cm^3 g^{-1}).

A Raman microscope (DXR, Thermo Scientific) registered the Raman spectra of samples mounted and dried under a nitrogen atmosphere on glass slides by applying 5 mW (λ_{laser} = 532 nm) to register 128 scans with 2 cm^{-1} resolution. Figure S2.2 shows the Raman spectra of ZnS in the cubic phase, in agreement with the XRD data in Figure S2.1 The main Raman lines in Figure S2.2A occur at 269, 349, 423, and 612 cm^{-1}, and they are associated to the transverse optical phonon (TO) at the Γ point, the longitudinal optical phonon (LO) at the Γ point, the sum combination bands for the LO and the transverse acoustic phonon (LO + TA), and the overtone from the combination of two different TO phonons.[57] The oxidation of sulfide hole scavenger during the reaction produces a small amount of yellow colloid during irradiation, identified as elemental (rhombic) sulfur, S_8, in the Raman spectrum (Figure S2.2B-D). This species is not derived from the catalyst that remains intact as shown by XRD and TEM data. Rhombic sulfur is as an oxidation intermediate produced by the sulfide hole scavenger with Raman peaks at 220, 439 and

473 cm^{-1} that become more intense with longer irradiation time. The three peaks differ less than ±2 cm^{-1} from the previous assignment for the Raman active species of molecular S$_8$ with D$_{4d}$ symmetry.[75]
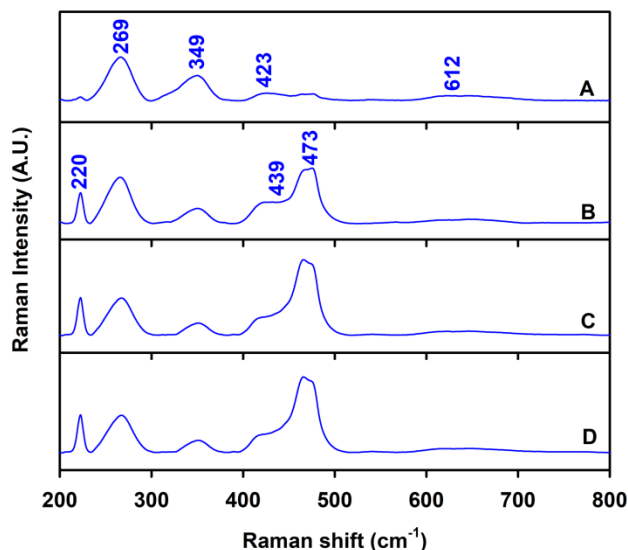
Figure S2.2 Raman spectra (λ_{laser} = 532 nm) for an experiment with a colloidal suspension of ZnS (A) before and after (B) 1, (C) 2, and (D) 3 hours of irradiation.

Since the XRD measurements showed that the crystallites phase and grain size were not significantly affected during photolysis, the particle sizes and morphologies before and after irradiation were expected to be similar. Thus, only freshly synthesized ZnS samples were analyzed by transmission electron microscopy (TEM). Samples for TEM were transferred to a 300-mesh Formvar-carbon coated copper grid and dried under nitrogen gas. The morphology of highly dispersed ZnS nanoparticles on the copper grid was visualized by TEM in a JEOL 2010F field emission electron microscope. The JEOL 2010F unit equipped with an Oxford INCA detector also provided energy-dispersive X-ray spectroscopy (EDS) measurements.

The TEM images in Figures S2.3A and B show aggregates of irregular shaped fine nanoparticles. Integration of the areas under the *K* lines in the EDS spectrum of Figure S2.3C indicates that the precipitated colloids are comprised of Zn and S elements with a Zn:S percentage ratio of 50.9:49.1. This ratio agrees with the 1:1 stoichiometry expected from the synthesis, and was also observed after one hour of irradiation. The presence of elemental C and Cu is due to the carbon coated copper grid used to hold the nanoparticles as confirmed by registering its EDS spectrum alone. A trace of oxygen peak (not indicated) in the EDS spectrum probably originates from the unavoidable surface-adsorption of oxygen onto the samples from exposure to air during sample processing.
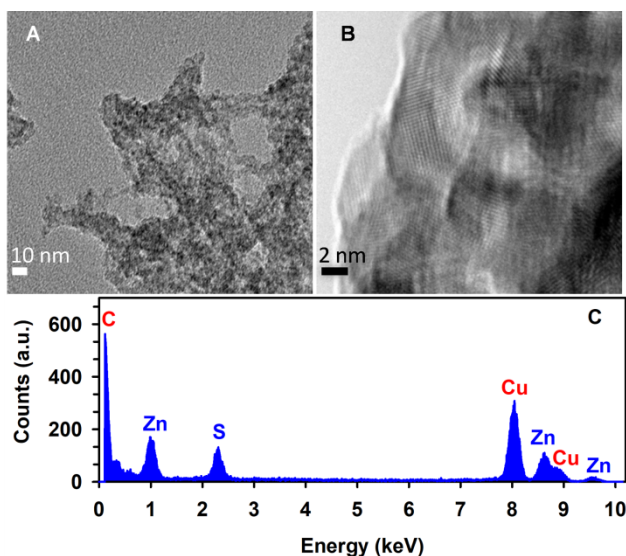
Figure S2.3 TEM images of ZnS with a scale of (**A**) 10 nm and (**B**) 2 nm. (**C**) EDS spectrum of ZnS.

Control experiments (Table S2.3) confirm that the production of formate is due to the irradiation of the ZnS colloidal suspension in the presence of sulfide hole scavenger.

Figure S2.4 shows the photoluminescence spectrum of a colloidal suspension of ZnS excited at λ_{exc} = 300 nm, which contains a broad peak centered at $^M\lambda_{em}$ =420 nm maximum emission wavelength. The plot to the left of Figure S2.4 contains the integrated photoluminescence intensity (area under the emission curve) for excitation wavelengths, λ_{exc}, values of 290, 300, 305, 310, 320, and 330 nm. The largest emission area in Figure S2.4 corresponds to a maximum excitation wavelength $^M\lambda_{exc}$ = 300 nm, which agrees well with the reflection edge observed for ZnS powder in Figure 2.5 of the main text. The observed photoluminescence band with $^M\lambda_{em}$ =420 nm, and FWHM of ~85 nm, originates from the recombination of electrons and holes in trapped surface states located in the forbidden region of the bandgap due to sulfur vacancies.[76] This photoexcited ZnS* decays a 90% within $\tau_{\lambda_{em}=420\,nm}$ ~30 ns.[69] The emission in the photoluminescence spectrum is Stokes shifted by ~108 nm with respect to the absorption band edge in Figure 2.5 (λ = 312 nm).
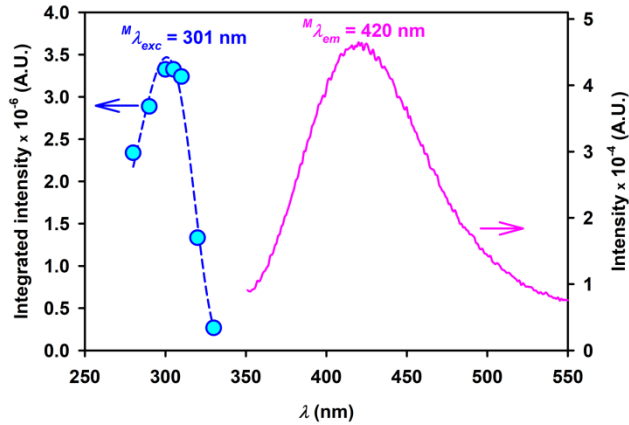
Figure S2.4 Photoluminescence spectrum of colloidal ZnS suspension excited at λ_{exc} = 300 nm (pink trace and right axis) and integrated photoluminescence intensities for 290 ≤ λ_{exc} ≤ 320 nm (blue circles and left axis).
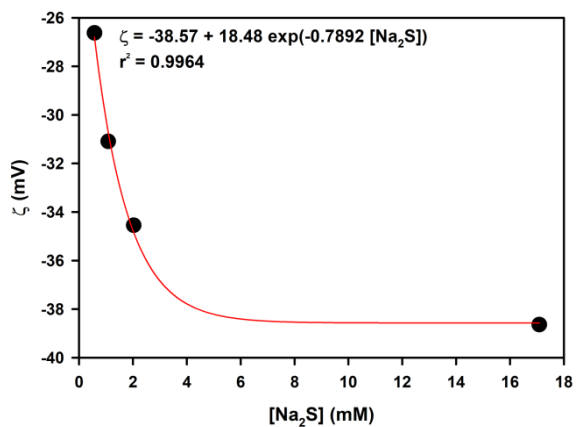
Figure S2.5 Zeta-potential (ζ) vs. increasing $[Na_2S]$ for undiluted samples under the same experimental conditions of Figure 7 (pH = 7.0). The red line shows the nonlinear least square regression for the equation given in the plot.
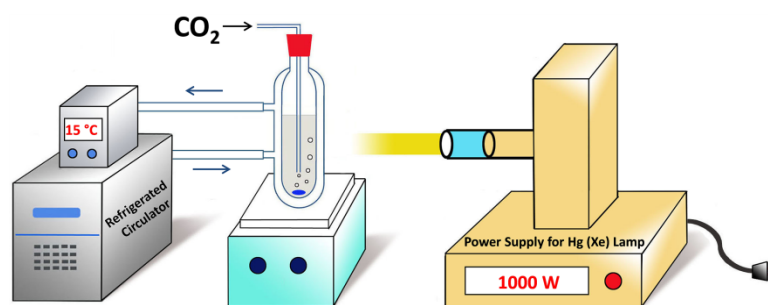
Scheme S2.1 Simplified diagram of photochemical setup.

Table S2.1 Reduction potentials for some half-reactions of interest

Reduction half-reaction	$E^o_{1/2}$ (V)	Ref.
$\emptyset_{ZnS} + e^- \rightleftarrows e^-_{CB(Zns^-)}$	-1.04	[45]
$CO_2(g) + H^+ + 2\ e^- \rightleftarrows HCOO^-$	-0.29	[77]
$2\ SO_4^{2-} + 2\ e^- + 4\ H^+ \rightleftarrows S_2O_6^{2-} + 2\ H_2O$	-0.25	[78]
$SO_4^{2-} + 2\ e^- + 2\ H^+ \rightleftarrows SO_3^{2-} + H_2O$	-0.10	[79]
$2\ H^+ + 2\ e^- \rightleftarrows H_2$	0.00	[77]
$S_2O_6^{2-} + 2\ e^- \rightleftarrows 2\ SO_3^{2-}$	0.04	[78]
$S(s, \text{rhombic}) + 2\ e^- + 2\ H^+ \rightleftarrows H_2S(aq)$	0.17	[77]
$SO_4^{2-} + 8\ e^- + 9\ H^+ \rightleftarrows HS^- + 4\ H_2O$	0.25	[77]
$2\ SO_4^{2-} + 8\ e^- + 10\ H^+ \rightleftarrows S_2O_3^{2-} + 5\ H_2O$	0.29	[79]
$SO_4^{2-} + 8\ e^- + 10\ H^+ \rightleftarrows H_2S(aq) + 4\ H_2O$	0.31	[77]
$SO_4^{2-} + 6\ e^- + 8\ H^+ \rightleftarrows S(s, \text{rhombic}) + 4\ H_2O$	0.36	[77]
$h^+_{VB(ZnS^+)} + e^- \rightleftarrows \emptyset_{ZnS}$	2.55	[45]

Reduction potentials for standard states versus the normal hydrogen electrode (NHE). The relationship $E^o_{1/2} = 0.05916\ pe^o$ was used to convert the reference values.[77, 79]

Table S2.2 Electrons loss by sulfide sequential oxidation at the valence band of ZnS

Initial oxidation state		Intermediate or final oxidation state				
		0	+II	+IV	+V	+VI
		S	$S_2O_3^{2-}$	SO_3^{2-}	$S_2O_6^{2-}$	SO_4^{2-}
-II	S^{2-}	-2	-4	-6	-7	-8
0	S		-2	-4	-5	-6
+II	$S_2O_3^{2-}$			-2	-3	-4
+IV	SO_3^{2-}				-1	-2
+V	$S_2O_6^{2-}$					-1

Table S2.3 Experiments and controls to demonstrate the heterogeneous production of formate

	Conditions				Product
	ZnS	UV	CO_2	Hole scavenger	$HCOO^-$
Experiment	+	+	+	+	+
Control A	−	+	+	+	−
Control B	+	−	+	+	−
Control C	+	+	−	+	−
Control D	+	+	+	−	−

Table entries of "+" and "−" indicate the presence or absence of a species, respectively.

Chapter 3. Photocatalytic Reduction of Fumarate to Succinate on ZnS Mineral Surfaces
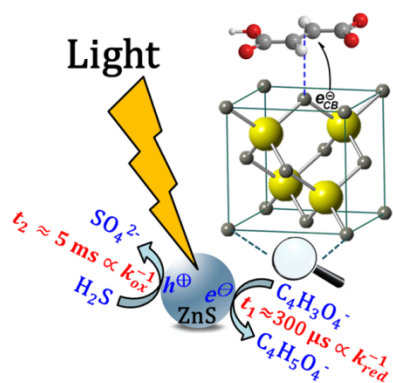
Scheme 3.1 Synopsis TOC

3.1 Synopsis

The reductive tricarboxylic acid (rTCA) cycle is an important central biosynthetic pathway that fixes CO_2 into carboxylic acids. Among the five reductive steps in the rTCA cycle, the 2-electron reduction of fumarate to succinate proceeds nonenzymatically on the surface of photoexcited sphalerite (ZnS) colloids suspended in water. This model reaction is chosen to systematically study the surface photoprocess occurring on ZnS in the presence of [Na_2S] (1-10 mM) hole scavenger at 15 °C. Experiments at variable pH (5-10) indicate that monodissociated fumaric acid is the primary electron acceptor forming the monoprotic form of succinic acid. The following reaction scheme is proposed: (1) Photoexcitation of ZnS generates conduction band electrons and valence band holes, (2) the hole scavenger donates electrons while producing sulfur-containing intermediates en route to sulfate formation, (3) a first electron transfer occurs at the conduction band converting chemisorbed monoprotic fumaric acid at surface zinc sites into an adsorb radical anion, (4) the radical anion accepts a second electron and forms an adsorbed carbanion, which (5) abstracts two protons consecutively from either hydronium ion (acidic condition) or water (neutral and basic condition) to be desorbed as monodissociated succinic acid. The apparent quantum yield measurement of succinate production (Φ_s) under periodic irradiation at $\lambda \geq 305$ nm shows that the timescale of electron transfer on the conduction band (t_1) and valance band hole loss (t_2) are in the order of hundred microseconds and a few milliseconds, respectively. These transitions (t_1 and t_2) become undistinguishable at 520 μs for a zeta potential $\zeta = -22.09$ mV corresponding to [Na_2S] = 0.57 mM. Overall, this work provides new insights to model

heterogeneous processes such as the reduction of CO_2 occurring on the surface of photocatalysts and advance present understanding of photocatalytic reactions.

3.2 Introduction

The photocatalytic harvesting of solar photons can potentially address the growing demand of energy supply faced worldwide.[80] In this context, photocatalytic studies have largely focused their attention in producing renewable $H_2(g)$ from water splitting,[81] while more recently the reduction of CO_2 has regained attention as a possible mechanism to fix this atmospheric greenhouse gas and produce useful hydrocarbon fuels.[9, 82-83] In general, the reported difficulty for promoting the photocatalytic reduction of CO_2 is the high initial energy cost of the one-electron reduction to produce $CO_2^{\bullet-}$, which has a standard reduction potential $E^0 = -1.85$ V at pH 7[83]. Efforts to improve the low quantum yield of typical reductions have proposed to control the properties of photocatalysts to increase the number of photoexcited carriers on the surface where the reaction takes place.[2] Surface modifications that activate the semiconductor also facilitate charge separation,[2] suggesting the importance of measuring the lifetimes of surface excited states. Recently, various doping of nanostructures, combinations of semiconductors, and the addition of sensitizers were explored.[83] However, a central physical chemistry concept that has been ignored[83] until our previous publication[9] is that the effective transfer of electrons to adsorbed substrates occurs in relatively slow timescales.[9]

In addition to the energy applications discussed above, prebiotic chemists have been interested in the use of photocataysis to drive a cycle of carbon fixation inspired in the reductive tricarboxylic acid (rTCA) cycle relevant to the origin of life.[14, 17, 38, 84-85] The

origin of life is one of the most important unsolved questions of science,[86] which combines several diverse disciplines, including physical chemistry. A further discussion to context of this research in the origin of life field is presented in the accompanying Supporting Information. Photocatalyzed reactions have been proposed as fundamental for the origin of life[14, 17, 38, 47, 84-85, 87-88] by directly providing carboxylic acids to the rTCA cycle.[14, 17, 38, 85] The photoexcitation of mineral semiconductors by sunlight opens new reaction pathways through the generated excited-state species and radicals.[14] For example, three out of five reductions from the rTCA cycle can be driven by photocatalysis on the surface of ZnS colloids suspended in water using Na_2S hole scavenger.[14, 85] The stoichiometric yields of the conversion from oxaloacetate to malate, fumarate to succinate, and 2-oxoglutarate to oxalosuccinate were 75, 95, and 2.5 %, respectively.[14] The low yield for the reductive carboxylation of 2-oxoglutarate to oxalosuccinic acid, its consecutive reduction to form cis-aconitic acid, as well as the reductive carboxylation of succinic acid to 2-oxoglutaric acid have been difficult to achieve.[14] Furthermore, the actual photocatalytic mechanism of the working reductive steps has remained unexplored.[84]

The focus of this study on ZnS factors in that the photocatalyst was indicated as an excellent mineral present in Hadean environments due to its stability with respect to $ZnCO_3$.[14, 47] The conduction-band electrons of the semiconductor have a sufficiently negative reduction potential (-1.04 V versus NHE) to drive all the reductions steps in the rTCA cycle.[14, 47] Moreover, ZnS can harvest energy from sun's photons to promote the reaction under study, which is slow by thermal chemistry alone.[14, 47] In our previous work, the reduction of CO_2 to formate ($HCOO^-$) was reported in great detail using

illuminated aqueous suspensions of ZnS semiconductor as the catalysts.[9] The work

developed new methods to study photoreductions reactions,[9] and pointed out that to

enable any progress in this field, further understanding of the photocatalytic processes

and the associated surface mechanisms are needed. In this context, the production of C-C

coupling dimers in a mixture of 2,5-dihydrofuran and tetrahydrofuran on irradiated ZnS

indicates the surface reactivity of adsorbates with double bonds.[89]

In this work, the efficient and specific reduction of fumarate to succinate is purposely

chosen as a model reaction to study the heterogeneous mechanism on ZnS. In this system,

the reaction is not governed by the equilibrium thermodynamics, as for biological

systems, because it should proceed favorably ($E° = +0.031$ V pH 7.0 and 298 K).[90]

Instead the reaction is sluggish due to kinetics limitations that can be reversed without the

generation of side products upon irradiation of ZnS to proceed efficiently. This work

aims to gain new fundamental understanding of the photocatalytic process, compare it to

that of CO_2 reduction,[9] and provide insights conducting to improving the efficiency for

the reductive carboxylation reactions on ZnS, e.g., for 2-oxoglutarate. The determination

of the bandgap of synthesized ZnS nanocrystallites suspended in water is explored by

quantifying the rate of succinate production R_s at different cut-off wavelengths of

irradiation ($\lambda_{cut-off}$). After studying the effect of pH on R_s, the apparent quantum yields of

succinate production (Φ_s) at $\lambda = 325 \pm 20$ nm are determined under continuous and

periodic irradiation. The dependence of Φ_s on [Na_2S] yields information to distinguish

the timescales for hole loss and electron transfer for the model system. Finally, all

observations are summarized in a proposed reaction mechanism showing the importance

of adsorption processes as a limiting factor regulating the transfer time scale of charge

carriers in photocatalysis.

3.3 Experimental Details

3.3.1 Catalyst Preparation.

ZnS photocatalyst was freshly prepared at a loading of 2.3 g L^{-1} by dropwise addition

of 100 mL of 50 mM Na$_2$S (99.1 % assay, Sigma-Aldrich) to 100 mL of 50 mM ZnSO$_4$

(ZnSO$_4$·7H$_2$O, Sigma-Aldrich ReagentPlus, 99.0 %) under continuous N$_2$(g) (UHP,

Scott-Gross) sparging.[9] Degassed ultrapure water (18.2 MΩ cm, Elga Purelab Flex,

Veolia) was used in all experiments. The concentration of stocked sulfide solution was

measured after a 1:100 dilution with 2.00 M NaOH (99.3 % assay, Fisher Chemicals)

using a sulfide ion selective electrode (Thermo, Orion 94-16).[9] The previously diluted

sulfide solution was further diluted with an equal volume of 2.00 M NaOH, and then

titrated with 100 mM cadmium nitrate (cadmium nitrate tetrahydrate, Aldrich ≥ 99.0 %).[9]

The concentration of sulfide hole scavenger during photoirradiation was

potentiometrically quantified using a calibration curve. The decrease of sulfide

concentration followed a first order decay curve with a correlation coefficients $r^2 > 0.998$.

3.3.2 Photoirradiation Experiments.

Experiments were performed by placing 100 mL of ZnS suspension in a 200 mL

customized cylindrical quartz photoreactor surrounded with a water jacket.[9] The

temperature was kept at 15 °C by flowing water through the photoreactor from a

circulating bath (Thermo Scientific SC100-A25).[9] A 1 kW high-pressure Hg(Xe) arc

lamp provided with a water filter, to remove infrared radiation, was used in combination

with a cut-off optical filter. Optical filters with a cut off wavelength $\lambda_{cut\text{-}off}$ = 280, 295, 305, 320, and 400 nm were used in selected experiments.[9] Results report the average of duplicate experiments with one standard deviation. In a typical experiment, the reduction of fumarate to succinate in an aqueous suspension of ZnS was conducted under continuous irradiation at $\lambda \geq 305$ nm. A volume of 0.25 mL of $[Na_2S]$ = 3.270 M was added to the colloidal suspension, which was augmented with 1.0 mmol sodium fumarate (Alfa Aesar, 99.6 % assay). The initial concentration of sulfide was ~ 8.0 mM (pH $\approx$ 12.10) and dropped to ~ 2.0 mM upon adjustment to pH ~ 7.05 with H_2SO_4 (Acros Organics, 98.0 %).

Φ_s was determined under continuous and periodic illumination from the ratio of rate of succinate production to the effective photon flux. The effective photon flux for the wavelength range 325 ± 20 nm was determined by potassium ferrioxalate actinometry after convoluting the spectrum of the actinometer[91] with that reported for the catalyst in water.[9] Light modulation by pulses from 0.02 to 2400 Hz, for illuminated periods lasting τ_L = 0.208 ms – 25 s on, were provided by a mechanical shutter and optical choppers as described previously.[9] Aliquots (5 mL) were extracted from the reactor every 20 min and centrifuged at 4400 rpm for 5 min in the dark. Sulfide concentrations were monitored with the ion selective electrode as described above for experiments with initial $[Na_2S]_0$ = 1.03, 2.03, 5.07, and 10.07 mM.

Control experiments (Table 3.1) were designed to prove that the only operative mechanism for fumarate reduction was photocatalysis. Each control tested whether succinate production proceeded or not in the absence of one of the following conditions: ZnS (control A), light ($h\nu$) (control B), fumarate (control C), and hole scavenger (controls

D). Alternatively, the use of 8.0 mM sodium sulfite (99.9 % assay, Fisher chemicals) instead of Na$_2$S as the hole scavenger was assayed in control E.

Table 3.1 Control experiments to demonstrate the photocatalytic production of succinate.

	Conditions				Product
	ZnS	UV	Fumarate	Hole scavenger	Succinate
Experiment	+	+	+	+	+
Control A	-	+	+	+	-
Control B	+	-	+	+	-
Control C	+	+	-	+	-
Control D	+	+	+	-	-
Control E	+	+	+	+[a]	+

[a] 8.0 mM Na$_2$SO$_3$ was used instead of Na$_2$S

3.3.3 Analysis of Products

All samples were centrifuged at 4400 rpm for 5 min, filtered (IC Acrodisc 0.2-μm pore size; Pall Corp.) to discard the precipitate, and diluted 8-times for analysis with a Dionex ICS-2000 Ion Chromatography system.[9] This system was equipped with an AS autosampler (Dionex), a suppressor, a hydroxide (OH⁻) eluent generator (KOH cartridge EGC III, 0.38 mL/min as the flow rate), an anion trap column (CR-ATC), and a conductivity detector. Chromatographic separation of anions was carried out with an IonPac AS11-HC analytical column (2 × 250 mm) coupled with an IonPac AG11-HC guard column (2 × 50 mm).[9] The initial 1 mM hydroxide concentration was kept constant for 8 min, and then increased linearly to 15 mM for 10 min, followed by a second

gradient to 30 mM [OH⁻] for 10 min, and a third increment to 60 mM for 10 min.[9] A 0.12

mL min⁻¹ flow of 0.42 mM formic acid (Fisher Optima LC-MS grade, 99.6 % assay) in

methanol (Fisher Optima LC/MS grade, 99.99 % assay) was mixed with the

chromatographic eluent through a Tee connection.[9] A mass spectrometer (Thermo MSQ

Plus) interfaced by an electrospray ionization probe operating in negative ion mode

allowed sample identification of the mass-to-charge ratio (m/z) of anions in the mixed

flow. The optimized mass spectrometry parameters were: needle voltage 1.9 kV, cone

voltage 50 V, probe temperature 450 °C, and nitrogen nebulizing 70 psi.[9] Anions

identified by mass spectrometry included fumarate (m/z 115), succinate (m/z 117),

bicarbonate (m/z 61), bisulfite (m/z 81), bisulfate (m/z 97), hydrogen thiosulfate (m/z

113), and hydrogen dithionite (m/z 129). Succinate was quantified from calibration

curves prepared with sodium succinate (Alfa Aesar, 99.75 % assay). In selected

experiments, the concentration of fumarate was also monitored based on the comparison

of integrated chromatographic peak areas to a calibration curve prepared using sodium

fumarate.

3.3.4 Mineral Characterization.

The characterization and stability of the mineral was assessed after drying samples of

ZnS as described before,[9] by powder X-ray diffraction (XRD) and Raman spectroscopies

as well as by transmission electron microscopy (TEM). In summary, XRD spectra and

TEM micrographs show the catalyst is the same before, during, after irradiation, and even

after a second round of photolysis experiments when reusing ZnS.[9]

The concentration of dissolved Zn^{2+} during photoirradiation experiments was

measured every 30 min by atomic absorption spectroscopy (Thermo Scientific iCE 3000

Series) at $\lambda = 213.9$ nm using a Zn hollow cathode lamp with a flame made of acetylene and air (both Scott Gross, UHP grade). A calibration curve was prepared with the same matrix using a non-irradiated sample under the same experimental conditions.

3.4 Results and Discussion

3.4.1 Identification of Products

Figure 3.1 shows the ion chromatogram of species identified as products during the reduction of fumarate on ZnS colloids irradiated for 2 h at $\lambda \geq 305$ nm. The separated chromatographic peaks correspond to anions eluting with m/z values with a retention time (t_r): succinic acid monoanion (m/z = 117, $t_r = 18.07$ min), , bisulfite (m/z = 81, $t_r = 18.85$ min), bicarbonate (m/z = 61, $t_r = 19.25$ min), bisulfate (m/z = 97, $t_r = 19.32$ min), fumaric acid monoanion (m/z = 115, $t_r = 20.06$ min), hydrogen thiosulfate (m/z = 113, $t_r = 24.52$ min), and hydrogen dithionite (m/z = 129, $t_r = 32.30$ min).
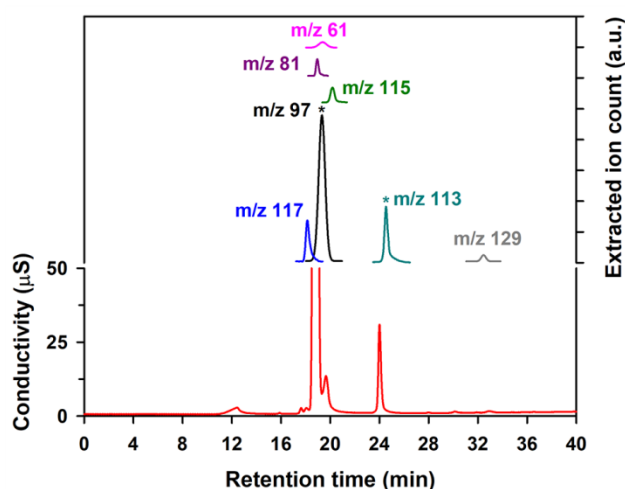
Figure 3.1 Ion chromatogram of a photolyzed ($\lambda \geq 305$ nm) sample of 1.0 mM fumarate in 2.3 g L^{-1} ZnS at pH 7.02 for 2 h in the presence of $[Na_2S]_0 = 2.0$ mM. Extracted anion peaks for succinate (m/z 117), bicarbonate (m/z 61), bisulfite (m/z 81), bisulfate (m/z 97), fumarate (m/z 115), hydrogen thiosulfate (m/z 113), and hydrogen dithionite (m/z 129) are displayed. Peaks (*) at m/z 97 and 113 are scaled down 10-times.

The black traces in Figure 3.2 show examples for the production of succinate versus time at (solid squares) pH 5.32 and (empty circles) 7.02. The linear fitting to the experimental data yields succinate production rates with time, t (min), of $R_s = 2.669$ μM min$^{-1} \times t$ ($r^2 = 0.992$) at pH 5.32, and $R_s = 0.464$ μM min$^{-1} \times t$ ($r^2 = 0.984$) at pH 7.02. Control experiments (Table 3.1) demonstrate that the reduction of fumarate to succinate proceeds by heterogeneous photocatalysis. Controls A-D showed no production of succinate. Specifically, the participation of any thermal reaction contributing to the reduction of fumarate in our system is discarded by control B in the absence of irradiation. Interestingly, succinate production was observed when substituting Na$_2$S by 8.0 mM sodium sulfite as the hole scavenger (Control E). These results confirms that the reduction of fumarate proceeds with high yield and that no alternative products are generated,[14] even when employing several cut-off irradiation filters ($\lambda_{cut-off} \geq 280$, 295, 305, and 320 nm) or varying the pH (5-10).
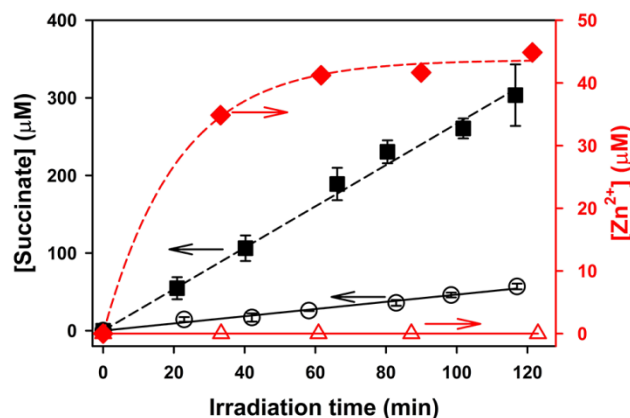
Figure 3.2 [Succinte] and dissolved [Zn^{2+}] during 2 h irradiation ($\lambda_{cut-off} \geq 305$ nm). Key: Empty black circle = [succinate] at pH 7.02, solid black square = [succinate] pH 5.32, empty red triangle = [Zn^{2+}] at pH 7.02, and solid red diamond = [Zn^{2+}] at pH 5.32. Other conditions as listed in Figure 1.

The integrity of ZnS at low pH is affected as the material starts to dissolve into Zn^{2+} and S^{2-} ions (Figure 3.2). For example, at pH 5.32, $[Zn^{2+}]$ rises exponentially with time according to $[Zn^{2+}] = 43.7 \times (1 - e^{-0.0473 \times t})$ ($r^2 = 0.997$) reaching a plateau after 1 h with maximum $[Zn^{2+}]_{max} = 43.7$ μM (Figure 3.2). Even for this low pH, the generated excess of Zn^{2+} and the adsorption of H_3O^+ on the surface of ZnS are not sufficient to overturn the negative zeta potential $\zeta_{pH = 5} = -20.12$ mV.[9, 92] This pH dependent dissolution of ZnS should not be confused with corrosion, which was observed in the absence of hole scavenger (e.g., $[Zn^{2+}] = 365.59$ μM at pH = 7.02 after irradiation for 2 h). The photodecomposition of ZnS can proceed via an irreversible reduction of lattice zinc ions by conduction band electrons and the oxidation of lattice sulfide ions by holes.[93] Therefore, the presence of dissolved sulfide ion hole scavenger in the experiment allows the reversal of photooxidation by providing a substitution mechanism that contributes to maintain the stability of ZnS during illumination.[93] At pH ≥ 7.0, no dissolved Zn^{2+} was observed during irradiation, as depicted in the experiment at pH 7.02 ($\zeta_{pH = 7} = -31.09$ mV) in Figure 3.2, proving the stability of the catalyst.

The production of elemental (rhombic) sulfur (S_8) during photoirradiation was observed as a slight yellow color developed over the white background colloidal suspension. Raman microspectroscopy provided a confirmation for the generation of S_8.[9] A photoxidation mechanism in presence of HS⁻ hole scavenger prevent the photodegradation of the photocatalyst by substituting S^{2-} to the photooxidized lattice sites.[93] As a result, S_8 is produced during irradiation from the oxidation of sulfide hole scavenger.

3.4.2 Identification of a Monoanion Intermediate as the Primary Electron Acceptor

Fumaric acid (pK_{a1} = 3.02 and pK_{a2} = 4.38 at 25 °C)[26] can dissociate twice as indicated by the sequence of equilibrium reactions (1) and (2):

$$HCOO-CH=CH-COOH \rightleftarrows HCOO-CH=CH-COO^- + H^+ \tag{1}$$

$$HCOO-CH=CH-COO^- \rightleftarrows {}^-COO-CH=CH-COO^- + H^+ \tag{2}$$

Based in the speciation of fumaric acid for pH < pK_{a1}, the diprotic form (H_2A) is the major species present in equilibrium, and the completely dissociated form (A^{2-}) is the dominant species for pH > pK_{a2}. For the intermediate pH-range bracketed between pK_{a1} and pK_{a2}, the monoanion form (HA^-) of fumaric acid becomes the main species in equilibrium. The same concept applies to describe the dissociation of succinic acid, as a diprotic acid (pK_{a1} = 4.21 and pK_{a2} = 5.64)[26] product. Figure 3.3 shows the dependence of the rate of succinate production R_s on pH and the speciation curves for the diprotic species succinic acid in the pH range 5.06-10.09. The direct correlation of the experimental R_s data to the calculated fraction of succinic acid monoanion (HA^-) suggests this preferred photoproduct is directly generated from adsorbed monoprotic furmaric acid. In consequence, adsorbed fumaric acid monoanion is reduced by the sequential transfer of two electrons. These results agree with the trend observed for a smaller number of experiments that also monitored the initial rate of fumaric acid loss at variable pH.
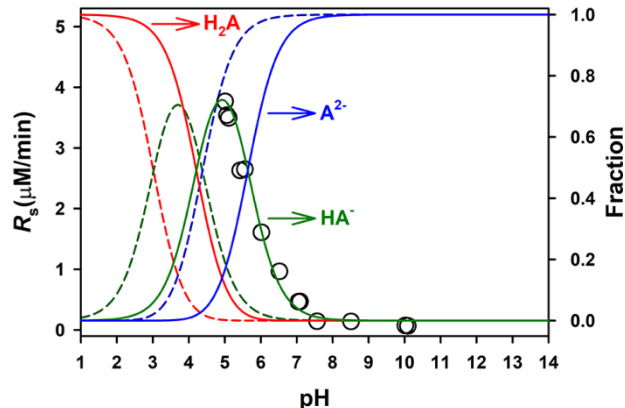
Figure 3.3 Rate of succinate production (R_s) for $\lambda \geq 305$ nm at variable pH and corresponding fractions of (dashed line) fumaric and (solid line) succinic acids available as diprotic acid (H_2A, red trace), monoanion (HA^-, green trace), and dianion (A^{2-}, blue trace) species. Other conditions as listed in Figure 1.

The resembling behavior of both R_s and the fraction of succinic acid monoanion with pH depicts the surface reaction of adsorbed fumaric acid monoanion to start through a weak π-bond interaction with an active zinc site. The undissociated –COOH group of fumaric acid monoanion is in closer proximity to the surface than the dissociated –COO$^-$ group. A lone pair of electrons in the C=O moiety of the –COOH group could facilitate this configuration by establishing a second weak interaction with a contiguous zinc site. Instead, the dissociated –COO$^-$ group of fumaric acid monoanion is initially repelled from the negatively charged surface of ZnS with a point of zero charge at pH 4.2.[9] The adsorption of the monoanion of fumaric acid by ZnS must occur reversibly[94] in an adsorption-desorption equilibrium that is quickly established. The fast equilibrium proposed is needed to justify the quantification of dissolved species in the bulk liquid. However, the interchange between adsorbed and dissolved species must be slow as compared to the generation of excited states during illumination.

As stated above, the pH regulates the strength of the electrostatic interactions between fumaric and succinic acids with the nanoparticles of ZnS. While the associated binding constants for the process considered remains unknown, they can be assumed to be quite small so that the interaction between both substrates and the particles are labile.[95] For low pH, the zeta-potential of ZnS becomes considerably less negative ($\zeta_{pH = 5}$ = -20 mV)[9] than at neutral conditions, while simultaneously the fraction of monodissociated carboxylic acid decreases as the concentration of the diprotic species growths. This intermediate protic form may also represent the optimized structure for succinic acid to be desorbed from the surface preventing the reverse charge transfer reaction between succinic acid and a hole. Therefore, the pH of the colloidal suspension plays a role for the optimum adsorption to balance out the surface charge of the nanoparticles and the availability of less repulsive substrates. Overall, the photocatalytic reduction of fumaric acid on the surface of ZnS proceeds through the most stable configuration of the intermediate formed on the surface. During the progression of the reaction, this intermediate is depleted and replenished on the surface by other molecules of fumaric acid available.

3.4.3 Bandgap Determination of ZnS in Water from Reaction Rates

The bandgap energy of ZnS colloidal suspensions in water was reported in our previous study based on the dependence of the reaction rate of formic acid production from CO_2 (R_{HCOO^-}) on the cut-of wavelength of irradiation.[9] This work serves as a new demonstration that measuring a reaction rate such as the reduction of fumarate to succinate on photo-excited ZnS reveals the bandgap energy of the semiconductor suspended in water. The measured rate of succinate production in units of $\mu M \times min^{-1}$ is R_s = 0.739 ± 0.020 (r^2 = 0.994), 0.600 ± 0.022 (r^2 = 0.986), 0.464 ± 0.002 (r^2 = 0.984),

and 0.298 ± 0.002 ($r^2 = 0.992$), for irradiation at $\lambda_{cut\text{-}off} \geq 280$, 295, 305, and 320 nm,

respectively. No production of succinate was observed for irradiation at $\lambda_{cut\text{-}off} \geq 400$ nm.

Figure 3.4 shows the linear regression fitting of the four quantifiable fumarate production

rates vs. $\lambda_{cut\text{-}off}$, in which R_s (μM min^{-1}) = 3.971 - 0.0115 $\times \lambda_{cut-off}$ ($r^2 = 0.999$) is

extrapolated to $R_s = 0$ to intercept the abscise at $\lambda_{cut\text{-}off} = 345$ nm. This extrapolated value

represents the minimum energy required to excite the mineral catalyst for the

photoreduction of fumarate to occur, which corresponds to E_{BG} for ZnS.
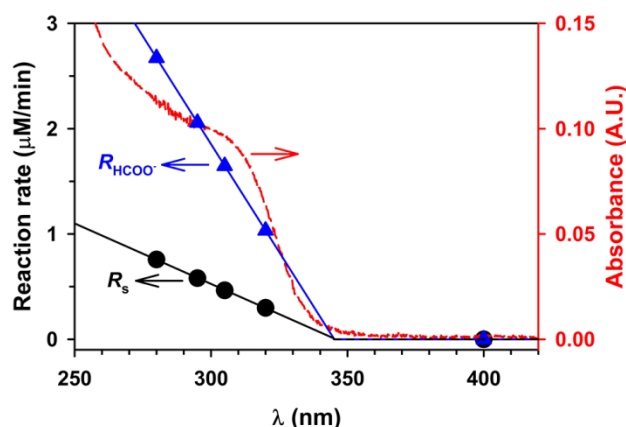
Figure 3.4 Reaction rate of (black circle) succinate (R_s) production vs. cut-off wavelengths of irradiation. Other conditions as listed in Figure 1. For comparison, the reaction rate of (blue triangle) formate production (R_{HCOO^-}) from CO_2 and the diffused reflectance absorption spectrum of ZnS in water from Ref. [9] are included.

The extrapolated value of $\lambda_{cut\text{-}off} = 345$ nm is in an excellent agreement with the

measured photoreduction rate of CO_2 to formate on ZnS R_{HCOO^-} ($\mu M/min$) = 14.152 –

0.0410 $\times \lambda_{cut\text{-}off}$ ($r^2 = 0.995$).[9] Thus, this wavelength can be used to obtain the bandgap of

the semiconductor accordingly to $E_{BG} = h\, c/\lambda_{cut\text{-}off} = 5.74 \times 10^{-19}$ J $\equiv 3.59$ eV, where h is

the Plank constant and c is the speed of light. Therefore, this bandgap value measured

during reactions in water confirms our previous finding and agrees well with the reported

absorption spectrum for a colloidal suspension of ZnS (Figure 3.4).[9]

3.4.4 Apparent Quantum Yields under Continuous and Periodic Illumination

The photoreduction of fumarate on ZnS was studied under continuous and periodic illumination experiments at $\lambda = 325 \pm 20$ nm. The effective photon flux (I_0) was obtained after correcting the actinometric measurement by convoluting the spectrum of ferrioxalate[91] with that for ZnS in water.[9] The calculation of the apparent quantum yield of succinate production at $\lambda = 325 \pm 20$ nm was directly derived from the ratio of the reaction rate to the effective photon flux: Φ_s (%) $= 100 \times R_s/I_0$. This Φ_s value represents a lower limit for the actual quantum yield, because light is extinguished by absorbing and scattering particles.[56] For example, experiments under continuous illumination of 2.3 g L^{-1} ZnS with 1.0 mM fumarate, $[Na_2S]_0 = 2.0$ mM, at 15 °C and pH 6.73, proceed with a reaction rate $R_s = 7.74 \times 10^{-9}$ mol L^{-1} s^{-1}, which combined to the measured $I_0 = 2.02 \times 10^{-7}$ einstein L^{-1} s^{-1} yields $\Phi_s = 3.85$ %.

Despite any factors that could affect the measured Φ_s values,[70] the information below if of general interest because it resolves the lifetime of redox carrier on the surface of photo-excited ZnS during the reduction of fumarate. For this purpose, a series of experiments applied monochromatic periodic illumination with equally lasting dark (τ_D) and bright (τ_L) cycles to study how Φ_s varies in the range 208 µs $\leq \tau_L \leq 1$ s. For example, Figure 5 shows the dependence of Φ_s on τ_L, for an initital hole scavenger concentration $[Na_2S]_0 = 2.00$ and pH $= 7.00$. For the fastest time intervals explored, as $\tau_L \rightarrow 0$ the apparent quantum yield under periodic illumination $\Phi_{L\rightarrow0}$ is practically identical to that measured under the continuous irradiation ($\Phi_s = 3.85$ %). When moving from the measured $\Phi_{L\rightarrow0}$ value to the right in Figure 5, for progressively longer bright intervals,

lower quantum yields are registered down to a minimum $\Phi_{L\to\infty} = 0.16$ % as $\tau_L \to \infty$.

During this transition from $\Phi_{L\to0}$ to $\Phi_{L\to\infty}$ in Figure 5, there are two inflection points

associated to redox carriers with different reactivity.[9, 71] After fitting a double sigmoid

curve to the data in Figure 5 using nonlinear least-squares regression, the infection points

are extracted from the second derivative are $t_1 = 320$ µs and $t_2 = 4.87$ ms.
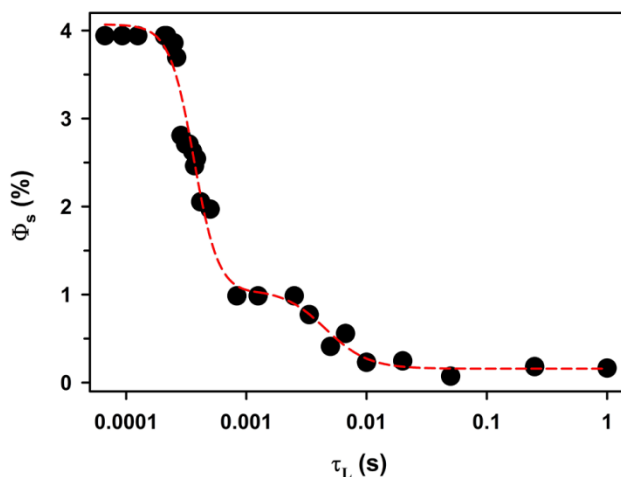
Figure 3.5 Apparent quantum yield of succinate production (Φ_s) vs. the bright interval time under periodic illumination (τ_L) of 2.3 g L^{-1} ZnS with 1.0 mM fumarate at pH = 7.0 and $[Na_2S]_0 = 2.03$ mM.

Similar values of $t_1 = 296$ µs (in the order of hundreds of microseconds) and $t_2 = 4.48$

ms (in the order of a few milliseconds) can also be obtained from the two inflexion points

measured when plotting the first-order rate constant of sulfide decay (k_{-H_2S}) vs. τ_L, as

described previously.[9] While sulfide was confirmed to remain stable in dark controls,

experiments under periodic illumination at variable $[Na_2S]_0$ allowed the assignment of t_1

to the transfer of reducing conduction band electrons to the monoanion of fumaric acid.

Accordingly, t_2 corresponds to the loss of oxidizing valence-band holes during the

photooxidation of hole scavenger species. The relationship of t_1 and t_2 to the redox

carriers is explained by their dependence on $[Na_2S]_0 = 1.03, 2.03, 5.07$, and 10.07 mM, all values involving initial concentrations of the hole scavenger < 65 mM[9] of submonolayer coverage of ZnS. The correlation of $[Na_2S]$ versus ζ follows an exponential function reported in our previous work.[9]

Considering that the surface potential of ZnS can be represented by ζ for unchanged permittivity and viscosity in the electrical double layer,[50-51] an increment of $[Na_2S]_0$, is associated to a more negative surface potential. Assuming that suspended ZnS particles under irradiation behave as microelectrodes, the surface potential of the mineral can be related to the half-reduction and half-oxidation rate constants from the Bulter-Volmer (BV) equation,[9, 71] which are $k_{red} = k_0\, e^{-\left[\frac{\alpha_{red}\, n_{red}F}{RT}\right](E-E^0)}$, and $k_{ox} = k_0\, e^{\left[\frac{\alpha_{ox}\, n_{ox}F}{RT}\right](E-E^0)}$, where n_{red} and n_{ox} are the number of electrons transferred in each half-reaction, k_0 is the standard heterogeneous rate constant, α_{red} and α_{ox} are the dimensionless charge transfer coefficients, E is the excess redox potential, E^0 is the standard redox potential of ZnS, R is the gas constant, F is the Faraday constant, and T is the absolute temperature.

Figure 3.6A shows the opposite trends that the lifetime for both redox transitions t_1 and t_2 have for increasing $[Na_2S]_0$. Figure 3.6B displays, as predicted by the expressions for the rate constants k_{red} and k_{ox}, the opposing trends for the dependence of t_1 and t_2 on ζ. Given the opposite signs in the exponential terms of the rate constants expressions (negative for k_{red} and positive for k_{ox}), and the reciprocal dependence between lifetimes on rate constants, it follows that the first transition $t_1 \propto k_{red}^{-1}$ and the second transition $t_2 \propto k_{ox}^{-1}$. Therefore, as the potential represented by ζ becomes more negative (for higher $[Na_2S]_0$) t_1 decreases while t_2 increases in Figure 3.6 This interpretation agrees with t_1

being related to k_{red} as reported for the reduction of CO_2 on ZnS[9] and the generation of gaseous H_2 on CdS.[73] In other words, t_1 represents the overall time needed to transfer conduction band electrons to reduce fumarate to succinate. These t_1 values (from 225 to 330 μs) are well in the order of the lifetime of conduction band electrons (~200 μS) observed for CdSe/CdS sensitized solar cells coated with two layers of ZnS for a photovoltage of 0.5 V.[96] Similarly, t_2 characterizes the slower loss of oxidizing valence-band holes. Figure 3.6B also includes the linear fittings to the semi-log plot: $log\ t_1 = 0.02079\ \zeta + 0.1785$ ($r^2 = 0.934$), and $log\ t_2 = -0.06809\ \zeta + 1.714$ ($r^2 = 0.981$). These transitions (t_1 and t_2) become undistinguishable at 520 μs for a zeta potential $\zeta = -22.09$ mV corresponding to $[Na_2S] = 0.57$ mM.
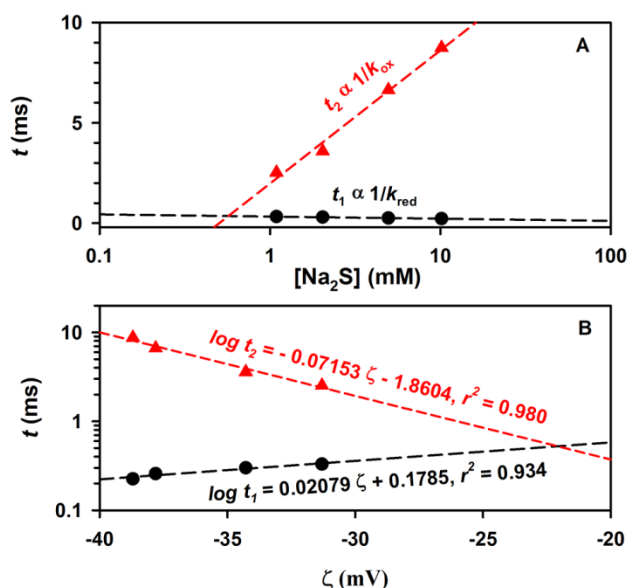
Figure 3.6 Transitions (●) t_1 and (▲) t_2 vs. (A) variable $[Na_2S]_0$ and (B) zeta potential (ζ). The red solid and black dashed lines show the linear least squares regressions, which intercept for a coverage of $[Na_2S] = 0.57$ mM, corresponding to $\zeta = -22.09$ mV and $t = 520$ μs.

The relatively long times linked to electron transfer and hole loss at the surface of the photoexited ZnS* semiconductor nanoparticles provides fundamental information to

understand the dynamic process of photocatalysis.[97] The measured transfer of surface

carriers are relatively long (>200 µs for the transfer of mobile electrons and a few

milliseconds for loss of fixed holes) when compared with the time scales explored by

time-resolved spectroscopy of semiconductors (e.g., 150 fs $\leq \tau_{1/2} <$ 100 µs).[97] Averages

values of $\overline{t_1} = 307 \pm 17$ µs and $\overline{t_2} = 4.68 \pm 0.28$ ms are obtained for $[Na_2S]_0 = 2.0$ mM at

pH 7 from the data in Figures 3.5 and by measuring k_{-H_2S} vs τ_L. The fact that $\overline{t_1}$ and $\overline{t_2}$

are 11 and 29 times shorter than the corresponding values for the reduction of CO_2 (using

pure inorganic reagents) to formate under the same conditions[9] indicates the structure of

the adsorbate modifies the lifetime of the surface-active center of ZnS*.[98] Overall, these

results reveal concepts that can be used to optimize applications of photocatalysis such as

wastewater treatment, abatement of air pollution, and energy production.[97]

3.4.5 Proposed Mechanism for the Reduction of Fumarate on ZnS

A strictly heterogeneous photoprocess is considered to propose in Scheme 3.1 a

reaction mechanism describing the kinetic behavior observed in experiments performed

under variable pH, $\lambda_{cut-off}$, τ_L and ζ. The previous assumption is useful to simplify the

mechanistic scheme proposed, which is not necessarily the concluding pathway for the

reactions.[98] Reaction R1 in Scheme 3.2 shows that upon absorption of a photon ($\lambda \leq 345$

nm) by ZnS, an oxidizing hole is created in the valence-band from where an electron is

promoted to the conduction band.[99] The electron-hole pair can undergo recombination

and release heat by reaction R2 (Scheme 3.2) in processes that likely involves the

trapping of charge carriers by defects and the carrier recombination that occurs through

such defects (recombination centers).[98] The sacrificial sulfide electron donor is oxidized

by valence band holes through several intermediates (S_8, $S_2O_3^{2-}$, SO_3^{2-}, and $S_2O_6^{2-}$) en

route to form sulfate by reaction R3 (Scheme 3.2).[9] Simultaneously, fumaric acid is chemisorbed in dynamic equilibrium at an active zinc surface center and accepts a first electron via reaction R4 (Scheme 3.2).[89]
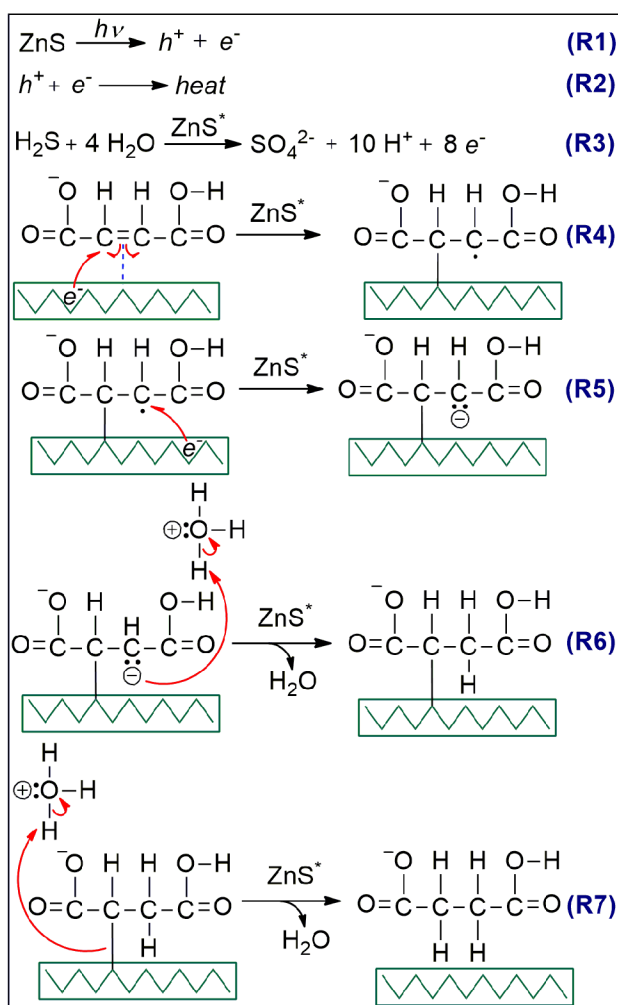
Scheme 3.2 Proposed mechanism for the reduction of fumurate to succinate on irradiated ZnS for the interval $5.06 \leq pH < 7.00$.

While the surface of ZnS can be considered as reversibly hydrated in an exchange that also allows adsorption of the organic molecules, this solvation process can affect the size as well as chemical and physical properties of ZnS. For example, if ZnS in aqueous suspensions adsorbs a proton or hydroxide ions, either positive or negative surface

charges are generated.[100] The hydration mechanism of aqueous ZnS in water can be explained at variable pH as follows:[101] 1) For pH < 4.2, the isoelectric point of ZnS, the surface becomes positively charged due to the neutralization of any negative charges from sulfide sites and that dissolution releases Zn^{2+} (Figure 3.2). 2) For the interval 4.2 < pH < 7.0, the acquisition of negative charge by the surface is proposed to be related to the Lewis acidity of zinc sites that forms $\equiv$SZnOH$^-$ and release protons to the medium. 3) For basic conditions (pH > 7.0), negative surface sites such as $\equiv$ZnOH$^-$ exist together with aqueous sulfide ions (HS$^-$, S^{2-}) in the bulk solution, all contributing to the observed negative zeta-potential of ZnS.[102] However, because Zn^{2+} is a borderline Lewis acid,[103] the exchange of adsorbed water or hydroxide ion by surface zinc occurs so fast that these active sites are continuously available for adsorption of fumaric acid.

Two additional problems that need to be approached are: 1) What is the most stable conformational isomer adsorbed to zinc sites? 2) How does adsorption occur? Based on the acid-base equilibria that optimizes the recognition of fumaric acid by the surface-active sites of ZnS*, the mechanism in Scheme 3.2 depicts the monoanion species as the primary electron acceptor adsorbed on the surface to the left side of reaction R4. Considering conformational isomerism is useful to identify the most stable monoanion species adsorbed on the mineral surface to undergo photoreduction to form succinic acid monoanion. The structures of two conformational isomers for the monoanion of fumaric acid are displayed in Scheme 3.3, where the carboxylate group is delocalized by resonance. These isomers differ mainly in the distance between the centers C_2 and O_4, which are calculated to be 3.56 ± 0.04 Å for isomer **A** and 2.75 ± 0.06 Å for isomer **B**.[104-105] The higher stability of isomer **A** is supported by a computational optimization of the

molecular geometry and zero-point energy of both isomers using Gaussian 09 with

B3LYP density functional theory methods[106-107] and a Gaussian 6-311G (d,p) basis set[108-109] we performed. Isomer **B** is predicted as less stable than isomer **A** due to steric

hindrance existing between the two π bonds.

(A)   (B)
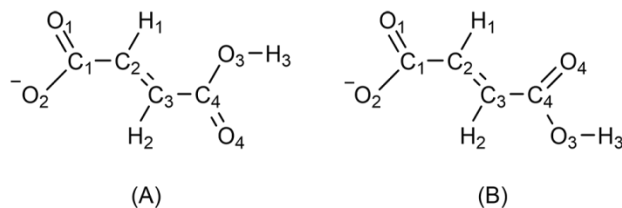
Scheme3.3 Structure of two conformational isomers of monodissociated fumaric acid.

The surface of synthesized ZnS exhibits a face-centered cubic structure with four

tetrahedral holes in each unit cell of length 5.39 ± 0.01 Å.[9] The calculated distance

between two zinc centers on the surface is 3.81 ± 0.01 Å (see powder XRD

measurements in Ref[9]). With all the previous considerations, Figure 3.7A depicts the

reversible adsorption of fumaric acid monoanion that likely results from a weak olefin π

bond interaction with an active zinc site (reactant of reaction R4, Scheme 3.2). Similarly,

the weak adsorption at a single zinc atom was observed for cyclic olefins on ZnS, which

occurs through the formation of a π-complex with an electron-deficient surface center.[89]

However, because the distance between two zinc sites (3.81 ± 0.01 Å) is only slightly

larger than the distance between C_2 and O_4 atoms for conformer **A** in Scheme 3.3 ($3.56 \pm$

0.04 Å), a double interaction with two zinc sites could arise from the π bond and a lone

pair from the O_4 atom in conformer **A** (Figure 3.7B). Therefore, the second adsorption

model involving a stable σ bond appears less favorable because desorption of the product

could be prevented.
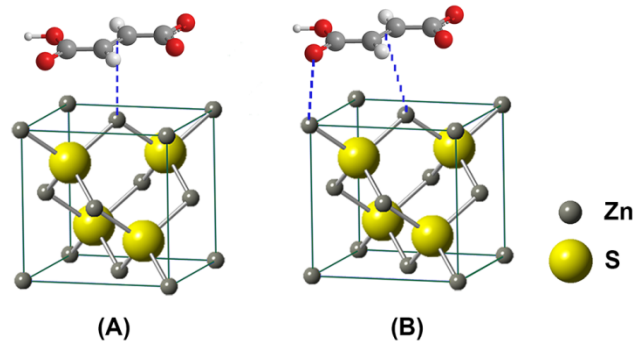
Figure 3.7 Adsorption of monodissociated fumaric acid on the surface of ZnS by interactions of (A) one zinc site to a π bond, and (B) two zinc sites to the π bond and a lone pair in a carbonylic oxygen atom.

Following the transfer of a first conduction band electron to the monoanion of fumaric acid, a short-lived radical centered on carbon C_3 of conformer **A** (Scheme 3.3) is produced by reaction R4 (Scheme 3.2). This adsorbed radical is stabilized by resonance with a carbonyl group. The transfer of a second electron to the previous radical intermediate also occurs on the surface of ZnS* facilitated by zinc sites to form an adsorbed carbanion depicted in reaction R5 (Scheme 3.2). The next steps are the sequential abstraction of protons from water (or hydronium for pH < 7) in reactions R6 and R7. Proton abstraction by reaction R7 occurs concomitantly to the surface desorption of succinic acid monoanion, as confirmed by the small rise in pH associated to the consumption of protons observed. Since the surface of ZnS is negatively charged at pH > 4.2,[9] the carboxylate group of the monoanions of fumaric and succinic acids are repelled from the surface, contributing to the desorption process of the product.

3.5 Conclusions

The data from experiments under periodic illumination demonstrate that the timespan needed to establish equilibrium condition between bulk and surface adsorbed fumaric acid monoanion is in the order of hundreds of microseconds. This conclusion is derived from modifying the period allowing replenishment of fumaric acid adsorption in the dark to contrast the depletion of reactive surface species during illumination. The simple zero-order kinetic behavior for the production of succinate indicates that the surface is quickly depleted of fumaric acid monoanion. The previous observation suggests that adsorption of fresh reagent limits (kinetic control) the zero-order rate of reaction. Therefore, the rate of electron transfer to the adsorbed species is limited by the rate of replenishment of fresh reactant from the solution. Further work should aim to advance this matter by studying the Langmuir isotherm derived from experiments at variable fumaric acid concentration that will change the surface coverage of ZnS.

Characteristic surface carriers remain active for several hundred microseconds for electron transfer and a few millisecond for the loss of oxidizing holes. This study confirms that reactive intermediates in a photoexcited semiconductor exist for relative long times, as observed before for adsorbed CO_2 undergoing reduction to $HCOO^-$ on the surface ZnS*,[9] when compared to the values measured by time-resolved spectroscopy of semiconductors (e.g., 150 fs $\leq \tau_{1/2} < 100$ μs).[97] The photoproduction of succinic acid in aqueous colloidal suspensions of ZnS in the presence of Na_2S directly consumes monodissociated fumaric acid as the adsorbed species. The reported bandgap of ZnS in water based on the dependence of R_s on $\lambda_{cut-off}$ agrees well with previous findings for the production of formate.[9] The measurement of Φ_s under periodic illumination provides

important evidence that the time scale of redox processes on the surface of semiconductors –the effective transfer of reactive carriers– is in the same order for sorption-desorption equilibrium. For the previous reason the structure of the adsorbate affects the lifetime of the surface-active center of the photocatalyst.[98] Overall, these results reveal new knowledge needed in the optimization of future applications of photocatalysis for fuel production, wastewater treatment, the abatement of air pollution, prebiotic chemistry, and abiotic photosynthesis.[84, 97]

3.6 Acknowledgement

3.7 Supporting Information for: Photocatalytic Reduction of Fumarate to Succinate on ZnS Mineral Surfaces

Context to the Origin of Life

The origin of life is one of the most important unsolved questions of science,[110] which combines several diverse disciplines, including physical chemistry. In this context, the large number of evolutionary scenarios that have been considered for the origin of life can be constrained by simultaneously considering bioenergetic, physical, and geological factors.[87] The connection between the origin of life and anabolism was recognized by Hartman, who introduced the concept of early metabolism by speculating a set of reactions conductive to the origin of life.[111] Before the discovery of the rTCA cycle, early metabolism was proposed as driven by UV light to fix $N_2(g)$ and $CO_2(g)$.[111] An autocatalytic rTCA cycle acting as a central biosynthetic pathway was introduced for a different model for driving redox reaction of thioacids powered by the oxidative formation of pyrite (FeS_2).[112] Despite the chemical energy source considered in those studies, the emerging concept of universal metabolism connecting all metabolic pathways is valid across all early metabolism models.[113-114] In addition, the autocatalytic rTCA cycle of thioacids powered by FeS_2 formation[112] was proposed as important for catalysis of slow reactions.[112] However, fast and efficient conversions within putative prebiotic metabolic systems for the rTCA cycle and redox systems lack any experimental support.[14] Instead, photocatalyzed reactions have been proposed as fundamental for the origin of life by directly providing carboxylic acids to the rTCA cycle.[14]

Our work advances a proposed evolutionary scenario that satisfies the known constraints for the emergence of life on Earth powered by UV solar radiation activating compartmentalized photocatalytic minerals such as sphalerite (ZnS) found around shallow water hydrothermal systems first proposed by Guzman and Martin.[15, 38] The Zn world hypothesis has improved such a system as the driver of CO_2 reduction to yield the building blocks for the first biopolymers, which serve as templates for the synthesis of longer biopolymers while acting as a protective shield that prevents photo-degradation.[87-88] In addition, predictions from the Zn world hypothesis about the role of Zn^{2+} ions in modern organisms have been successfully tested.[88] Several reactions of the rTCA cycle can be driven by illuminated ZnS at circumneutral pH and 288 K due to the reducing power of conduction-band electrons poised at -1 V vs NHE.[14] ZnS is believed to have been prevalent in the waters of early Earth[68] and possess a large band gap (E_{BG} = 3.59 eV).[9] Thermodynamically, ZnS has the potential to facilitate all reductions in the rTCA cycle (varying from −0.2 to +0.15 vs NHE)[90] to proceed in the presence of a scavenger to poise the valence-band hole at +2.6 V vs NHE. The photochemical model has the advantage to harvest energy from the sun to open new reaction pathways by the interactions of excited-state species and radicals. This work does not assume a direct utilization of photochemical energy to just boost reducing power from other pathways but highlights the unique role that photocatalysis may have played in the origin of life.

A final consideration is given to the problem of thermodynamic control, as given by the free-energy difference of the reaction. Thermodynamic control does not play a role in determining the formation of succinic acid during the photocatalyzed reduction of fumaric acid in ZnS colloidal suspensions. Instead, the reaction selected is kinetically

controlled, and the rate of formation of succinic acid is a key limitation. Furthermore, the reaction product is formed irreversibly, probably because succinic acid lacks the ability to interact with the surface of ZnS at the C_2-C_3 position for the reverse reaction to proceed. As a result, the consecutive removal of two hydrogens is mechanistically unfavorable.

Chapter 4. Catalyzed Synthesis of Zinc Clays by Prebiotic Central Metabolites

4.1 Synopsis

How primordial metabolic networks such as the reverse tricarboxylic acid (rTCA) cycle and clay mineral catalysts coevolved remains a mystery in the puzzle to understand the origin of life. While prebiotic reactions from the rTCA cycle were accomplished via photochemistry on semiconductor minerals, the synthesis of clays was demonstrated at low temperature and ambient pressure catalyzed by oxalate. Herein, the crystallization of clay minerals is catalyzed by succinate, an example of a photoproduced intermediate from central metabolism. The experiments connect the synthesis of sauconite, a model for clay minerals, to prebiotic photochemistry. We report the temperature, pH, and concentration dependence on succinate for the synthesis of sauconite identifying new mechanisms of clay formation in surface environments of rocky planets. The work demonstrates that seeding induces nucleation at low temperatures accelerating the crystallization process. Cryogenic and conventional transmission electron microscopies, X-ray diffraction, diffuse reflectance Fourier transformed infrared spectroscopy, and measurements of total surface area are used to build a three-dimensional representation of the clay. These results suggest the coevolution of clay minerals and early metabolites in our planet could have been facilitated by sunlight photochemistry, which played a significant role in the complex interplay between rocks and life over geological time.

4.2 Introduction

One of the major scientific questions that remains unresolved is how the origin of life occurred.[110] Within the prebiotic chemistry context of this interdisciplinary problem, recent work has shown the potential of ZnS promoted photocatalysis to harvest sunlight

energy into chemical bonds.[17] The mechanism of semiconductor promoted photochemistry may have played a major role in cycling small organic compounds essential for the origin of life.[84] For example, illuminated ZnS has successfully driven several reactions of the reverse tricarboxylic acid cycle (rTCA),[84] which is central to metabolism. Our latest work explored in detail the photoreduction of fumarate to succinate on the surface of ZnS,[115] which proceeds with a 95% yield.[14] The synergistic interaction between sunlight, photocatalysis, and organic acids in the prebiotic Earth[15, 38] could have promoted reactions otherwise not favoured, providing the foundation for present complex metabolism.[84]

Within the origin of life framework, a separate but relevant problem is the potential role of clay minerals, strong adsorbents of polar organic molecules,[116] to facilitate abiogenesis.[117] The catalytic power of clays can promote the polymerization of biomolecules and the conversion of fatty acid micelles into vesicles.[117] Indeed, the process of clay formation is key for developing an understanding of the possible roles of these minerals in the origin of life.[118] Recent work has proven the crystallization of saponite clays can proceed easily in only 20 h under relatively mild conditions in the presence of urea[119] as a catalyst. Interestingly, nowadays abundant oxalic acid, an endpoint oxidation product for all organic matter exposed to environmental oxidizers before their final conversion into formic acid and CO_2,[120-122] successfully substituted urea in the synthesis of saponite clays.[21] The role of oxalate as a chelating agent for aluminum atoms in the octahedral state has been previously studied.[123] Bare Al^{3+} has been proposed to retain the hexacoordination for crystalizing the phyllite structure when its complex with oxalate is decomposed in the presence of silicate.[123]

Despite the previous knowledge in both fields, the unanswered question remaining is whether a relevant clay formation mechanism could have proceeded catalyzed by photogenerated central metabolites[84] of the rTCA cycle. In this work, succinic acid (and other organic acids) is used as a probe from the intermediates of the rTCA cycle to catalyze the synthesis of sauconite, a model zinc trioctahedral clay mineral from the smectite family similar to saponite. The work hypothesizes that succinate accommodates in the interlayer space after catalyzing the incorporation of Al^{3+} into the precursor soluble gel, dominated by SiO_2, to create the tetrahedral layer. The work shows that sauconite crystallization is related to the ability of succinate to chelate bare Al^{3+}. Syntheses of sauconite are performed under variable initial concentration of sodium salts of carboxylic acids (e.g., $[succinate]_0$), pH, and temperature, to monitor during 20 h the nucleation process. Succinate is shown to catalyze the reaction of Al^{3+} with silicic acid, zinc and sodium compounds, yielding an authentic 2:1 clay mineral of the smectite group. The synthesis of Zn-clay material proceeds at low temperature (<100 °C) and ambient pressure (~1 bar) as demonstrated from the structural characterization displaying the early stages of the synthesis. This characterization is performed by a combination of techniques including: 1) Powder X-ray diffraction (XRD), 2) diffuse reflectance infrared Fourier transform (DRIFT) spectroscopy, 3) conventional transmission electron microscopy (TEM), and 4) cryogenic TEM (cryo-TEM).

4.3 Experimental Details

All syntheses are performed by duplicate. The analyses by the methods listed below are reported as mean values and standard deviations (± SD) from independent experiments.

4.3.1 Preparation of Sauconite.

The synthesis of $Na_{1.2}Zn_6 [Si_{6.8}Al_{1.2}]O_{20}(OH)_4 \cdot nH_2O$ started by diluting 4.0 g of Na_2SiO_3 solution (26.5 Wt. % SiO_2) in 10 mL water. A solution of $Al(OH)_4^-$ was prepared by dissolving 1.21 g of $Al(NO_3)_3 \cdot 9H_2O$ in 8 mL of 2.0 M NaOH. The addition of $Al(OH)_4^-$ solution to pre-diluted Na_2SiO_3 under continuous stirring, produced a cloudy gel that was left standing without stirring for 1 h before further use. The gel was stabilized with 1 mL of concentrated HNO_3 before addition of 4.81 g of $Zn(NO_3)_2 \cdot 6H_2O$ dissolved in 100 mL water. The synthesis was performed under reflux at 90 °C,[124] unless noted otherwise, by augmenting the gel with the sodium salt of succinic acid to reach a concentration in the range 0.010–1.0 M. Alternatively, formic acid, acetic acid, oxalic acid, or L-malic acid sodium salts were also employed (Supplementary Information). After 1 h of adding the organic salt, 2.0 M NaOH was used to vary the pH of gels with 0.10 M succinate in the range 6.4–13.9. The weight of sauconite obtained after 20 h under these conditions (0.10 M succinate at pH_0 7.0 and 90 °C) was 3.43 (± 0.01) g. In addition, for 0.10 M succinate, 20 h syntheses under stirring with reflux temperature from 70 to 90 °C every 5 °C were performed. Finally, the sauconite was centrifuged (5 min at 4400 rpm), triple washed with water, and dried overnight at 90 °C, unless noted otherwise.

4.3.2 Powder XRD Diffractograms.

A D8 Advance Bruker AXS diffractometer (Cu Kα, λ = 1.5418 Å) provided crystal structures. The diffractogram of samples mounted onto the sample holder was recorded from 2° to 90° at a scan rate of 0.01° s^{-1}. The distance of the 2:1 layer ($d_{0\,0\,1}$) was calculated using Bragg's law: $d_{0\,0\,1} = n\,\lambda/(2\,Sin\theta)$, where λ = 1.5418 Å (Cu Kα radiation) is the wavelength of X-ray, θ is the scattering angle, and the integer n is the order of the corresponding reflection. A traditional DIFFRAC method was applied to subtract the sharply increasing scattering of the incident beam from the background at low angle.[125] The method corrects the background by optimizing its maximum concavity, and enables the calculation of accurate $d_{0\,0\,1}$ values, e.g., 15.10 ± 0.09 Å. The application of this method is checked by measuring $d_{0\,0\,1}$ = 15.46 Å for a saponite standard $(Mg_2Al)(Si_3Al)O_{10}(OH)_2 \cdot 4H_2O$ from the Cuero Meteorite Crater in DeWitt Co. Texas (Excalibur Mineral Company). The diffractogram of the standard matches the pattern of saponite-15Å (ICDD PDF No. 00-030-0789).[126]

The preparation of oriented sauconite slides for XRD analysis in Figure S4.7 (Supplementary Information) was based on Drever's method.[127] Briefly, 25 mL of 0.50 M MgCl$_2$ was mixed in a 50 mL centrifuge tube with 200 mg of sauconite synthesized during 20 h with 1.0 M succinate at pH$_0$ 7.0 and 90 °C. After 1 min sonication and 5 min centrifugation (3000 rpm), the supernatant was discarded. This washing procedure was repeated by triplicate before a final wash with DI water to remove extra Mg^{2+}. The unflocculated suspension was filtered (0.45 μm pore size and 47 mm diameter) under vacuum. The sauconite sample was carefully transferred onto a glass slide (26 × 46 mm) as described in the filter-membrane peel technique.[127] The Mg-saturated glass slides were

analyzed by XRD from 2 to 40° 2θ degrees with a step scan of 0.07° (2θ) and a time per step of 4 s. Finally, the Mg-saturated sample was exposed to a vapor saturated glycerol atmosphere in a desiccator for 24 h before scanning by XRD. While the 2:1 layer structure is confirmed, the reversal in the intensities expected for both samples suggests there is no oriented stacking of layers, explaining the difficulties encountered during sample preparation.

4.3.3 DRIFT Spectra.

DRIFT spectra were recorded (200 scans) with a Nicolet 6700 FTIR spectrometer and analyzed with OMNIC32 software (both Thermo Fisher Scientific). A liquid nitrogen cooled MCT detector was employed in the range 600-4000 cm^{-1} with 4 cm^{-1} resolution. Oven dried samples of synthesized sauconite (30 mg) were homogenized with spectroscopic grade KBr (500 mg), and then poured into the smart collector diffuse reflectance accessory, which optics were continuously purged with $N_2(g)$. The incorporation of succinate over time was monitored by integrating the area under the C-H stretching (ν_{C-H}) between 2937 and 2991 cm^{-1}.

4.3.4 Measurement of TSA.

TSA is determined using the ethylene glycol monoethyl ether (EGME) method[128] for 0.5 g of sauconite synthesized 1) under variable [succinate] at pH_0 6.3, and 2) for pH_0 9.0 and 0.10 M succinate during the 20 h time series. Samples and a kaolinite standard (0.5 g each) were oven dried (90 °C) overnight, and analyzed following the standard procedure reported in the literature.[128]

4.3.5 Measurement of CEC.

For CEC measurements, 0.1 g of sauconite samples were washed with 20 mL of 0.5 M $MgCl_2$ during 10 s on a vortex stirrer, centrifugation at 8000 rpm for 5 min. The previous procedure was repeated, and similarly applied by duplicate after washing with 0.005 M $MgCl_2$. Finally, the Mg-saturated sauconite was washed twice with 1) 15 mL of 0.5 M $BaCl_2$ and 2) 20 mL 0.005 M $BaCl_2$, and the clear supernatant was discarded. The samples were dry in the oven (110 °C) overnight for analysis as indicated in the literature.[129-130]

4.3.6 TEM, EDS, and Cryo-TEM.

To image particle size and shape of the samples, aqueous suspensions (5 μL) from the synthesis were dispersed and pipetted onto a 200-mesh copper TEM grid with carbon support film (whole mount), and allowed to dry under air at room temperature. For high-resolution TEM (HRTEM), sampled from synthesis at different timepoints were embedded in EPON liquid epoxy resin. Approximately 10-20 mg of the sample was placed into 1.5 mL polypropylene Eppendorf micro-test tubes and dehydrated by adding 100% ethanol to remove adsorbed water. After centrifugation at 13000 rpm for 15 min, the supernatant was removed and the sample dispersed in a mixture of 10% EPON resin and 90% ethanol by ultrasonic treatment. These steps were repeated with mixtures containing 30, 50, 70, and 100% EPON.

To obtain complete dispersion of the material, the ethanol:resin mixtures were agitated in an ultrasonic bath for ~1 min. Each incubation step lasted 24 h with the samples placed onto a rotator to ensure continuous agitation. The resin-clay mineral mixture was transferred into embedding moulds after the fifth incubation step (100%

EPON resin). After a settling time of 1-2 h, the samples were polymerized by placing the moulds into an oven at 65 ºC for 48 h. Ultrathin sections (70-80 nm) were cut from the polymerized resin blocks using an ultramicrotome and transferred onto 200-mesh copper TEM grids with carbon support film. The samples on whole mounts and in ultrathin section were imaged with an FEI Tecnai G^2 F20 200 kV T EM equipped with a Gatan Ultrascan 4000 CCD Camera System Model 895 and EDAX Octane T Ultra W /Apollo XLT2 SDD and TEAM EDS Analysis System.

For cryo-TEM, 5 μL of the aqueous suspension of the synthesized sauconite (previous to the final drying and washing steps) was transferred onto a C-flat holey carbon sample support grid (R2/2; Protochips, Inc.). Excess fluid was blotted and the sample flash frozen hydrated by plunging into a bath of liquid nitrogen-cooled liquid ethane using the FEI Vitrobot Mk IV Grid Plunging System (FEI Co.). The grids were stored in liquid nitrogen until imaged in a FEI Titan Krios 300 kV Cryo-S/TEM equipped with a Falcon 2 direct electron detector (DED) (FEI, Inc). Images were collected at a magnification of 75k× corresponding to a pixel size of 1.41 Å and a defocus level ranging from −2.0 to −3.0 μm, under low dose conditions. Tomograms from the cryogenic and epoxy embedded samples were collected using FEI Batch Tomography Software version 4.0. The cryogenic tilt series was collected at a magnification of 59k× every 2º over a tilt range of ± 70º. The nominal pixel size was 0.14 nm with defocus of -2 μm.

4.3.7 Image Processing.

Images from the single-axis tomograms were aligned, filtered and reconstructed into a series of tomographic slices using IMOD (version 4.8.26).[131] The back projection method was used for reconstruction. The 3D visualization and surface models were created with

UCSF Chimera (version 1.10.1).[132]

4.4 Results and Discussion

The bottom-up synthesis of sauconite, with a theoretical full cell formula $Na_{1.2}Zn_6\{Si_{6.8}Al_{1.2}\}(O_{20})(OH)_4 \cdot nH_2O$,[116, 124] is performed from a silicic acid gel in contact with Zn^{2+}, Al^{3+}, and succinate^{2-} ions. The synthesis can be easily altered to vary the components integrated into the structure. Aiming at enhancing nucleation and to accelerate the formation of clay minerals, we designed a s vet of experiments to optimize the synthesis of a model sauconite. To study the role of succinate, a central metabolite, as a catalyst promoting clay formation, we made several modifications to the gel. In the first set of experiments we varied the concentration of sodium succinate (Figure 4.1). Alternatively, the nature of the organic salt is investigated by substituting succinate with sodium salts of formic acid, acetic acid, oxalic acid, and malic acid (Supplemental Fig. S1-S4 online). In the second set of experiments, we performed the synthesis under variable temperature. In the third set of experiments, the initial pH was varied in the range 6-14.

4.4.1 Effect of Varying the Concentration of Organic Acids.

Figure 4.1 shows the powder XRD diffractograms after 20 h of synthesis of the dried gel with and without succinate added. When no succinate is added, an amorphous gel is observed as shown by the lack of XRD reflections and presence of an elevated background in the 2θ range 15-35° (Figure 4.1A), which does not possess any features from the smectite group of 2:1 layer silicates. In contrast, the gel with succinate added at concentrations of 0.01, 0.10, 0.50, and 1.00 M (Figure 4.1) shows an XRD peak emerge

with a low-angle shoulder between 3.3 and 8.3° centered at 5.82° corresponding to a first-order basal reflection, $d_{0\ 0\ 1}$ of sauconite. The $d_{0\ 0\ 1}$ values, which corresponds to the thickness of the 2:1 phyllosilicate layer to layer distance (per half unit cell), increase for larger [succinate], varying between 14.2 and 15.1 Å (Figure 4.1B). In addition to the (0 0 1) reflection labeled in each XRD diffractogram, six more appear at 2θ angles of 11.46 (7.72 Å), 19.68 (4.51 Å), 28.60 (3.12 Å), 33.96 (2.64 Å), 59.98 (1.54 Å), and 70.20° (1.34 Å) most likely representing the (0 0 2), (0 2 l), (0 0 5), (1 1 0), (0 6 0), and (2 2 0) basal reflections of sauconite (ICDD PDF No. 00-008-0445),[126, 133] respectively. Interestingly, the weak peak at 4.51 Å that should correspond to the 0 2 l reflection suggests the sauconite is turbostratic (irregular and not perfectly oriented).[134-135] The peak (0 6 0) at 1.54 Å confirms the trioctahedral structure of sauconite. The reversal in the trend of $d_{0\ 0\ 1}$ with concentration above certain high [formate], or [acetate], [oxalate], or [malate] (Figure S4.1-S4.4, Supporting Information) is associated to larger particle sizes limiting the process of expansion.[136]
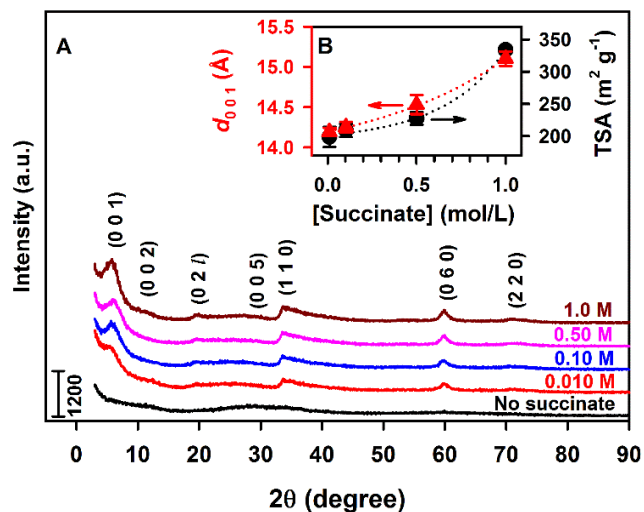
Figure 4.1 Powder XRD and TSA characterization of sauconite synthesized at pH_0 6.3 and 90 °C during 20 h under variable succinate concentration. (A) (A) XRD diffractograms for [succinate] listed above each trace. Numbers, e.g., (0 0 1), indicate basal reflections of the identified phases. (B) The layer to layer distance for 2:1 sauconite ($d_{0\,0\,1}$, red solid triangle) and TSA (black solid circle) for traces in (A) vs [succinate].

The higher $d_{0\,0\,1}$ basal spacings for the series of sauconite in Figure 4.1A with increasing succinate levels coincides with the growing total surface area (TSA) (Figure 1B). The larger TSA with increasing [succinate] is likely attributed to greater formation of the 2:1 layered structure. It is also probable that succinate has accumulated in the interlayer space, as supported by both the increase in $d_{0\,0\,1}$ basal layer to layer distance and the lower than expected total surface area of a 2:1 layered sauconite. The highest TSA value in the experiment of Figure 4.1 is 338.8 (± 4.1) m^2 g^{-1} (Figure 4.1B) indicates we are observing the beginning of the crystallization process. For comparison, the typical values of TSA for pure 2:1 layered clay minerals of the smectite family[116] ranging from 600 to 800 m^2 g^{-1} are only reached after 1 week of synthesis.

DRIFT spectra of the precursor gel, sauconite synthesized with [succinate] = 0.010, 0.10, 0.50, and 1.0 M, and sodium succinate are shown in Figure. S4.5 (Supporting

Information). In the gel, there is a broad band in the range 3100-3600 cm^{-1} corresponding to overlapping OH stretching bands due to water and the weaker corresponding OH-bending mode of water at 1645 cm^{-1} (Supporting Information Figure S4.5, dashed line).[135] In addition, there is a broad stretching band near 1000 cm^{-1} in the precursor gel assigned to Si-O. After addition of succinate, two new shoulders appear in the spectrum at ~3639 and ~3743 cm^{-1}, which are characteristic stretching vibrations of hydroxyl groups (ν_{OH}) attached to octahedral Zn ions located in the interior blocks of sauconite.[137] IR bands appear at 2951 and 2973 cm^{-1} in the presence of succinate and these are assigned as C-H stretching vibrations of succinate, which match the spectrum of the sodium succinate standard.

The new band at 1630 cm^{-1} in sauconite (Figure S4.5, Supporting Information) quickly grows from the stretching at 1645 cm^{-1} in the gel, due to OH bending vibrations of interlayer water.[134-135] This band at 1630 cm^{-1} due to the OH-bending mode of interlayer water is typical of 2:1 layered trioctahedral clay minerals.[138] After addition of succinate, the bands from the amorphous gel at 604 and 1009 cm^{-1} show the prominent development of sauconite shoulders from symmetric Zn-O vibration at 661cm^{-1}, and asymmetric in plane Si-O-Si vibration at 1020 cm^{-1}.[125, 136] The bands at 1404 and 1383 cm^{-1} in the amorphous gel are due to a small amounts of sodium nitrate left from the synthesis.[139] Spectra of sauconite also show bands at 1579 and 1296 cm^{-1}, corresponding to the stretching of C=O and C-O groups in the structure,[126] which are matched to sodium succinate standard (Figure S4.5, Supporting Information). Interestingly, the absorbance from succinate incorporated in the interlayer is correlated to the amount added during the synthesis. The intercalation of aliphatic organic carbon in 2:1 layered clay minerals has

been reported in pure standards and natural clays extracted from sediments.[140-141] Overall, two analytical methods (XRD and DRIFT spectroscopy) confirm a clay mineral is successfully synthesized in the presence of central metabolites such as acetate, malate, and succinate.

4.4.2 Effects of Temperature and pH.

Figure 4.2 shows the powder XRD diffractograms for 20 h syntheses with 0.10 M succinate under variable reflux temperature. While at 70 °C no sauconite formation is registered, the spectroscopic features of the mineral are observed at 75 °C. However, the first-order reflection (0 0 1) is only well-resolved for a minimum temperature of 80 °C, which allows the measurement of $d_{0\,0\,1}$ displayed in Figure 4.2B. As the first-order reflection (0 0 1) becomes better defined with increasing temperature, its width decreases indicating the layer to layer distance expands. For example, $d_{0\,0\,1}$ increases in Figure 4.2 from 13.6 Å at 80 °C to 14.2 Å at 90 °C. Control experiments demonstrate that sauconite dried overnight under room temperature (Figure S4.6, Supporting Information) showed the same XRD features observed when drying at 90 °C (Figure 4.2) was applied. Related experiments changing the pH of synthesis for 0.10 M succinate, under reflux at 90 °C for 20 h, demonstrate (see $d_{0\,0\,1}$ values in Figure S4.7, Supporting Information) that the best crystallinity is obtained at pH_0 9.0. Summarizing, the best conditions for studying the time series of the synthesis by microscopy techniques correspond to 1.0 M succinate, pH_0 9.0, and 90 °C for reflux. Comparison of samples after 20 h of synthesis under these optimized conditions, which have been Mg-saturated first and glycerol solvated second, revealed a 3.4 Å shifting of the (0 0 1) reflection (Figure S4.8, Supporting Information). Thus, expansion behavior for a double layer trioctahedral smectite is confirmed to be in

the range of reported values (3.1-3.7 Å) for 2:1 layer smectites.[142] The unexpected lower intensity observed after glycerol saturation confirms the 2:1 layer sauconite lacks any stacking of layers at 20 h. These experiments showing Al to Si ratios of 1:9 for the synthetized sauconite also discard the presence of tubular crystallites of imogolite in the samples.[116, 143]

4.4.3 Seeding Induced Crystallization.

The catalytic power of the synthesized clay is confirmed by repeating the procedure at 70 °C after spiking the gel with a single (macroscopic) sauconite particle obtained at 90 °C. As shown by the bottom trace labeled "seeded" in Figure 4.2, after spiking the single particle, the synthesis is promoted at 70 °C in the same 20 h timespan, yielding 1.86 (± 0.06) g of sauconite (a 54% of the material obtained at 90 °C). The fact that a simple particle of sauconite serves as a seed crystal to grow a larger amount of mineral serves as an outstanding example of the self-catalytic power of clays toward their crystallization. The surface of the seed particle facilitates heterogeneous nucleation at lower temperature by reducing the activation energy for crystallization. The observed acceleration in crystallization by seeding does not rely solely on random events but results from the surface interaction with chemical species in the precursor gel at 70 °C. The seed particle interacts with soluble free and complexed ions moving randomly in the gel, establishing intermolecular forces that are needed to form the crystal lattice. The addition of a seed particle to the gel provides a route to direct a process that does not depend on random interactions anymore.
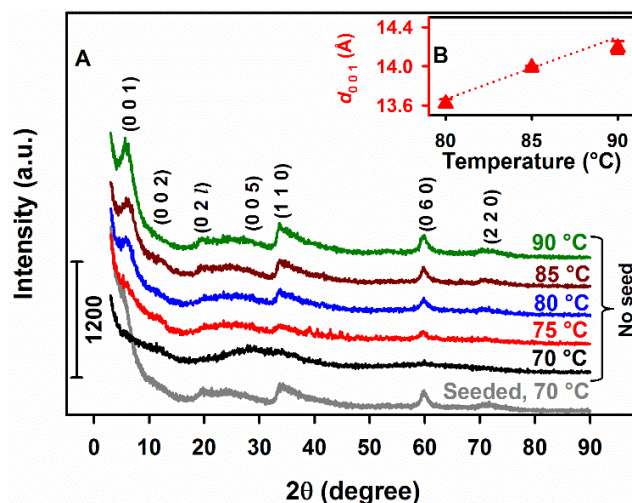
Figure 4.2 Powder XRD and $d_{0\,0\,1}$ values for 2:1 sauconite synthesized at pH_0 6.3 with 0.10 M succinate during 20 h under variable temperature. (A) XRD diffractograms under the temperatures listed above each trace. The gray line at the bottom labeled "seeded" corresponds to an experiment at 70 °C started after adding a single particle from sauconite synthesized at 90 °C. An oval shaped particle weighing 0.7 ($\pm$ 0.1) mg and symmetry axes of length 313 ($\pm$ 9) and 144 ($\pm$ 7) μm was used for seeding. (B) Values of $d_{0\,0\,1}$ (red solid triangle) for traces in (A) with no seed vs temperature.

4.4.4 Morphological and Structural Analysis.

Complimentary preparation, imaging and analytical techniques were applied to investigate the evolution of sauconite synthesized with 1.0 M succinate at pH_0 9.0 and 90 °C. Samples at the early (0 h), intermediate (6 h) and final stage (20 h) of the synthesis were selected for detailed analysis. The sample at zero timepoint revealed the presence of unstable Zn-containing plate-like particles, likely $Zn(OH)_2$, that are coated with Zn-containing nanoparticle, possibly of zinc silicate (Zn_2SiO_4) (Figure S4.9, Supporting Information). However, the previous phases were only observed in the untreated, air-dried condition for TEM and were likely unstable under the conditions required for plastic embedding or cryo-fixation. TEM images and energy dispersive X-ray spectroscopy (EDS) demonstrate that the morphology of the precursor gel corresponds to

an amorphous material that has not incorporated aluminum in the structure (Figure S4.9, Supporting Information).

After 6 h of synthesis the sample showed aggregates of sauconite nanocrystals, sometimes in association with an unknown gel-like phase (Figure 4.3A-C), and occasionally Zn-containing nanocrystals as seen in the sample at the zero timepoint. These latter crystals have an atomic structure close to Zn_2SiO_4.with lattice fringes spaced by ~2.3 Å (Figure 4.3C). Sauconite is made up of Al, Si, H and O in ratios similar to other smectite-group minerals (Figure 4.3D). Compared to the Zn-clay synthesized, the Zn-containing particles contain more Zn, much less Si and no Al. These nanoparticles were not observed in the TEM images from samples prepared for ultrathin section suggesting they are sensitive to the chemical treatment required for sample processing i.e. dilution, washing, dehydration, embedding. The objective of the TEM analysis of the samples in ultrathin section was to image the lattice fringes and observe the stacking order of individual 2:1 layers. High-resolution TEM (HRTEM) analysis of the cross-section through aggregates of sauconite showed disorganized and random arrangements of individual 2:1 layers. Most smectite-group minerals, including synthetic saponite,[21] consist of packets of short-range, turbostratic stacks of 2:1 silicate layers. Both the structure and chemical composition of sauconite resembles, however, other known smectite-group minerals.
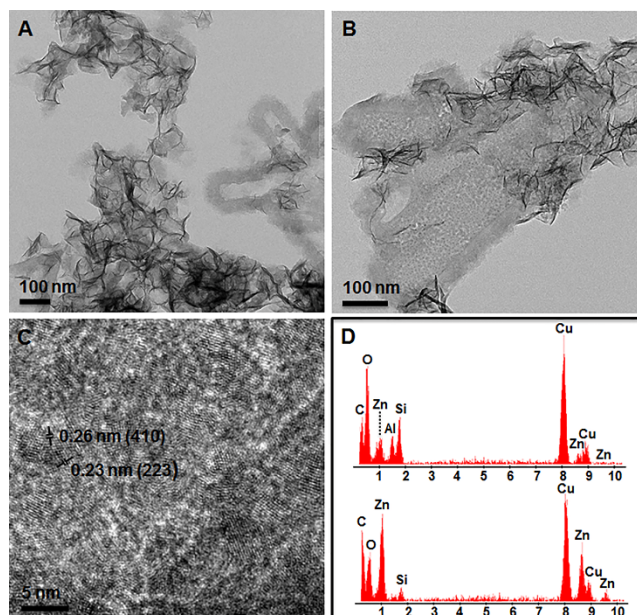
Figure 4.3 TEM images and energy dispersive X-ray spectra (EDS) of air-dried whole mount synthesized sauconite with 1.0 M succinate at pH_0 9.0 after 6 h reflux at 90 °C. (A) Aggregates of sauconite nanocrystals. Gel-like material shows nucleation of sauconite (right side of image). (B) Higher magnification of the gel-like sauconite showing the presence of unknown zinc-containing nanocrystals in addition to sauconite. (C) Lattice fringe image of zinc nanoparticles. (D) Representative EDS spectra of the composition of sauconite nanocrystals (upper) and zinc nanoparticles (lower). The presence of Cu is due to the carbon coated copper grid used for EDS analysis.

The structure and chemical composition of the sauconite 2:1 layers after 20 h of synthesis is the same as the sample collected after 6 h. There is, however, a difference in the organization and aggregation of individual 2:1 layers as well as in the distribution and density of the particles. The TEM images for the 20 h synthesis in ultrathin section shows only isolated stacks containing a few individual 2:1 layers of sauconite (Figure 4.4). The corresponding XRD diffractogram for this sample shows the 2:1 layer to layer distance expands a rate of 1.54 Å day^{-1}, which is accompanied by the incorporation of Al. Aluminum incorporation could take place by a 3 $Zn^{2+} \leftrightarrows$ 2 Al^{3+} + 1 vacancy substitution mechanism, which would not introduce a positive charge to the octahedral sheet.
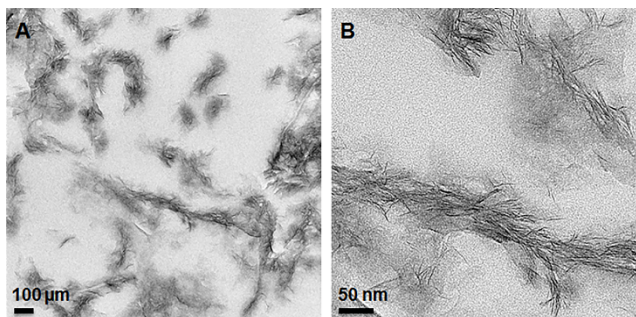
Figure 4.4 TEM images of ultrathin sections of synthesized sauconite with 1.0 M succinate at pH_0 9.0 after 20 h at 90 °C. (A) Overview of the area in the section containing aggregates of sauconite crystals. (B) Close-up of an aggregate of sauconite in the center of (A) showing the disorganized arrangement of individual 2:1 layer silicates with the occasional short-range stack of coherent layers.

4.4.5 Electron Tomography and 3D Reconstruction.

Electron tomography (ET) was carried out to determine the detailed 3D structure and mode of interaction of the sauconite 2:1 layers in ultrathin sections. The objective in ET is to reconstruct the 3D structure of an object from a series of 2D projections. Using the single-axis tilting method, a series of TEM images was collected from isolated aggregates of sauconite 2:1 layers in ultrathin section at every 2° tilt angle from − 70° to +70°. No significant differences were observed between samples after 6 and 20 h of synthesis. A snapshot of the tomogram and its reconstructed image are shown in Figure 4.5A-B. The images show the individual 2:1 layers are arranged in a random edge-to-face orientation within isolated aggregates.
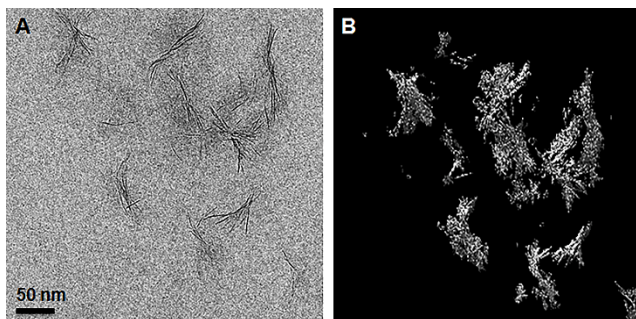
Figure 4.5 (A) Snapshot from a tomogram of an isolated aggregate of sauconite nanocrystals from a less dense area in the section for 20 h synthesis with 1.0 M succinate at pH_0 9.0 and 90 °C (B) 3D reconstruction of (A). See *Video* M4 in the *Supporting Information*.

Cryo-TEM was applied to study the size and shape of individual sauconite particles and their distribution in their natural dispersed state. The results of the extremely diluted (0.2 wt %) frozen samples show significant differences between samples collected after 6 and 20 h of synthesis (Figure 4.6). Figure 4.6A shows the emergence of the sauconite particles from the gel-like precursor suggesting initial nucleation and growth of the sauconite phase. Surprisingly, the sauconite 2:1 layers were not dispersed in either sample confirming the features and morphology observed in the ultrathin sections (Figure 4.5) is not an artifact, but a growth feature.
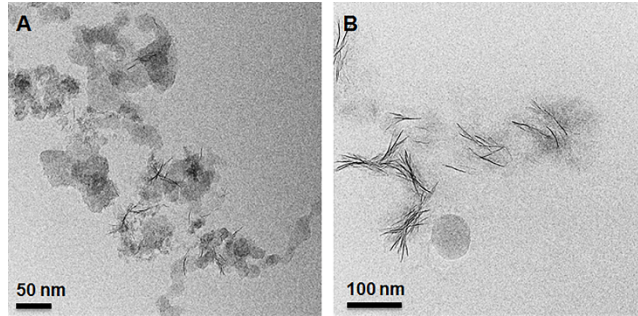
Figure 4.6 (A) Cryo-TEM image of sauconite synthesized with 1.0 M succinate at pH_0 9.0 after 6 h at 90 °C. The presence of irregular-shaped, possibly gel-like particles seen in Figure 4.3A-B in their dispersed state. The initiation of the formation of sauconite nanocrystals within these particles can be seen in the center of the image. (B) Cryo-TEM image of 20 h synthesis as for Figure showing isolated, disorganized aggregates of sauconite nanocrystals also seen in Figure 4.4. This sample in a diluted dispersed suspension consisting of pure sauconite nanocrystals.

Figure 4.7 displays snapshots from the tomograms of the sample after 20 h of synthesis (see Supplementary *Video* M1). Figure 4.7C-D shows the aggregation of individual sauconite particles consists of stacks of a few semi-oriented 2:1 layers suggesting a unique growth feature. Most synthetic or natural smectite-group minerals are completely dispersed as individual particles consisting of single 2:1 layers or stacks of a few ordered face-to-face 2:1 layers.[144] Different rotational views are displayed in Supplementary *Videos* M2 and M3.
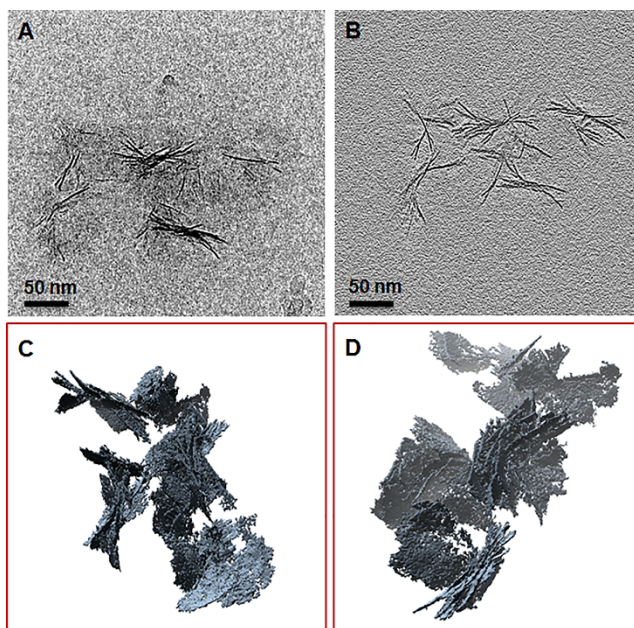
Figure 4.7 Snapshots from tomograms and 3D reconstructions for 20 h synthesis with 1.0 M succinate at pH_0 9.0 and 90 °C from cryo-TEM. (A) Raw image showing the individual aggregates of sauconite nanocrystals. (B) Reconstructed image of (A). (C) (D) Different views of reconstructed aggregates of sauconite nanocrystals seen in (A) and (B) showing the 3D arrangement and orientation of individual nanocrystals. See *Videos* M2 and M3 in the Supporting Information.

4.4.6 Kinetics of Crystallization and Swelling.

The results presented above confirm the formation of sauconite by several complementary methods. While TEM and cryo-TEM provide images of sauconite, they both indicate that XRD and DRIFT spectroscopy can be used to monitor the time series of Zn clay formation. Thus, a series of syntheses under the optimized conditions of 1.0 M succinate, pH_0 9.0 at 90 °C were performed and stopped at 0, 1, 2, 6, 15, and 20 h to monitor sauconite formation. Figure 4.8A and B show the timepoints for XRD diffractograms and DRIFT spectra. The (0 0 1) peak becomes evident after only 1 h and undergoes a pronounced broadening at 20 h. Similarly, the stretching vibrations for sauconite are clearly registered in the time series of Figure 4.8B, what makes possible to estimate a time profile for the incorporation of succinate. Finally, the time series of

measured TSA values for the corresponding samples is displayed in Figure 4.8C, where $d_{0\,0\,1}$ values extracted from Figure 4.8A and the integrated area under the C-H stretching ($v_{C\text{-}H}$) between 2937 and 2991 cm^{-1} from Figure 4.8B are also presented. Remarkably, the expansion of the layer to layer distance ($d_{0\,0\,1}$), the total surface area, and the amount of succinate accumulated in the interlayer, all depend on time with a similar exponential correlation (Figure 4.8C).
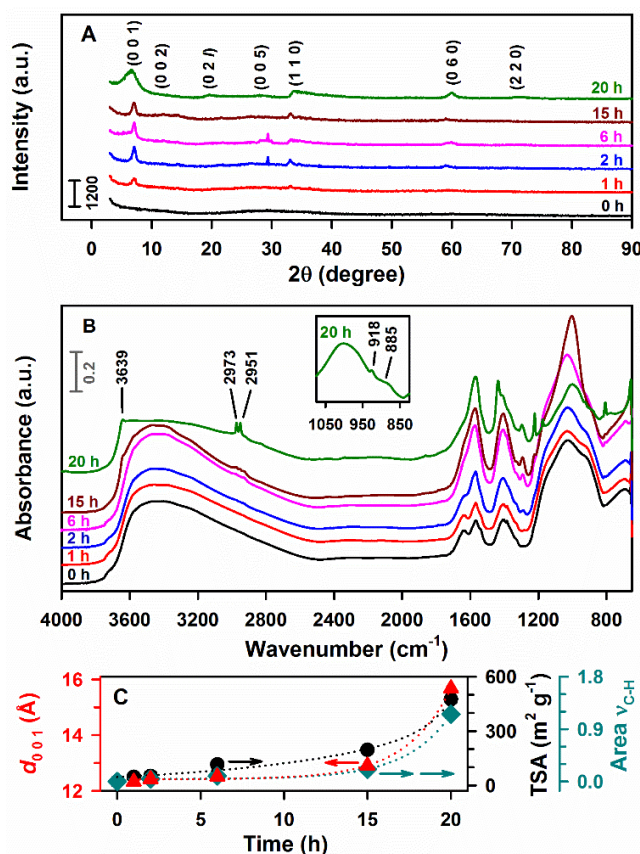
Figure 4.8 Time series of powder XRD diffractograms and DRIFT spectra registered at 0, 1, 2, 6, 15, and 20 h for sauconite synthesis with 1.0 M succinate, pH$_0$ 9.0 at 90 °C. (A) XRD diffractogram. (B) DRIFT spectra including an inset with features at 20 h. (C) Time correlation of $d_{0\,0\,1}$ values for 2:1 sauconite (red solid triangle) in (A), TSA (black solid circle) in (A), and the area for C-H stretching ($v_{C\text{-}H}$, teal solid diamond) integrated between 2937 and 2991 cm^{-1} in (B), after baseline correction with a two point algorithm.

The peak at 918 cm^{-1} in the DRIFT spectra of synthesized sauconite at pH$_0$ 9.0 from 0 to 6 h (Figure 8B) corresponds to Al-OH bending from the reactant Al(OH)$_4^-$,[145] the dominant hydroxy complex of aluminum in the starting gel at high pH.[123] As the previous peak disappears after 15 h of synthesis, a new peak is developed at 885 cm^{-1} assigned to Si-O-Al^{IV} vibrations in the tetrahedral position of sauconite. The stronger intensity for the Si-O-Al^{IV} vibration at 20 h in Figure 4.8B, which is also present in experiments with variable [succinate] (Figure S4.5, Supporting Information), suggests the incorporation of Al to the tetrahedral layer,[138] which is key for crystallization. The role of succinate as a catalyst is proposed to facilitate the simultaneous insertion of two Al^{3+} above and below a plane that becomes the interlayer of sauconite. Figure 4.9 displays a representation that takes into account the previous concept for the layers in 2:1 trioctahedral sauconite, which agrees with cryo-TEM, XRD, and DRIFT spectroscopy observations. In this model representation, succinate and the water molecules are slightly scaled-up relative to the centers in the crystalline structure to facilitate their visualization. The constrains that succinate experience to accommodate in the interlayer space is thought to be controlled by the slower free rotation of σ-bonds among carbon atoms in the gel compared to the freedom provided in a complete solution state. The 3D structure of succinate is represented in Figure 4.9 for the staggered conformation that decreases the torsional strain in energy from eclipsing interactions by optimizing the rotation around carbon-carbon σ-bonds. Because $d_{0\,0\,1}$ grows over time (Figure 4.8C), it is logic to assume that the sauconite structure in Figure 4.9 reaches its maximum swelling as the conformer of succinate optimizes its geometry reaching a length of 5.6 (± 0.7) Å. In addition, the selected succinate structure appears stabilized by interactions with two aluminum centers

located on opposite sites of the interlayer space (Figure 4.9). However, it would also be possible to envision interactions of succinate with a single zinc center of the interlayer. Figure 4.9 also depicts the tetrahedral–octahedral–tetrahedral sheets with Zn, Al and Si, as proved by EDS (Figure 4.3D).
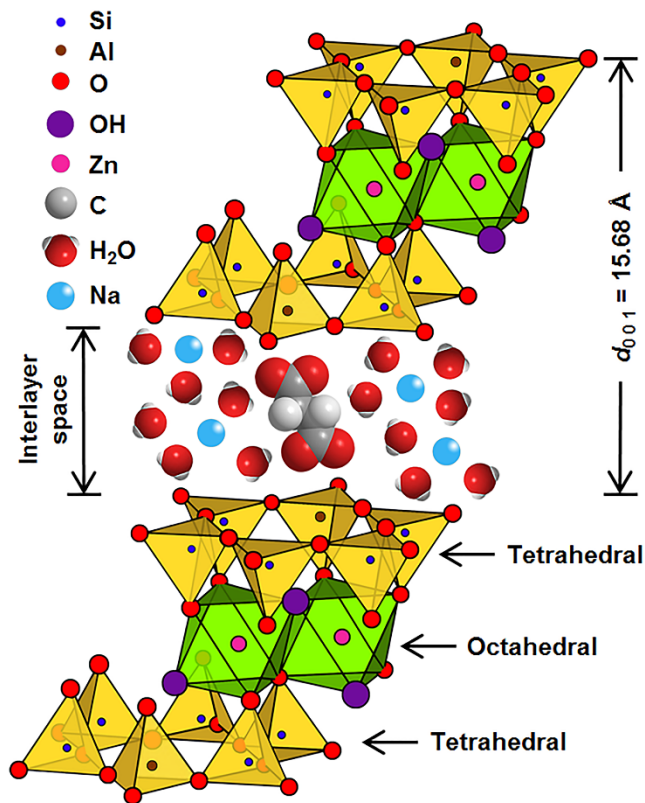
Figure 4.9 Model displaying the stacking order of layers in a 2:1 trioctahedral sauconite structure al synthesized during 20 h using 1.0 M succinate at pH_0 6.3 and 90 °C. The layer to layer distance $d_{0\,0\,1}$ = 15.68 Å is represented to be about 3-times larger than the length of succinate that appears longitudinally oriented perpendicular to tetrahedral aluminum centers.

The peaks at 1438 and 1570 cm^{-1} (Figure 4.8B) at 20 h of synthesis represent symmetric and asymmetric stretching vibrations for C=O ($v_{C=O}$) in the carboxylate group of succinate, respectively.[126] In addition, the two undissociated -COOH groups of succinic acid (pK_{a1} = 4.21 and pK_{a2} = 5.64)[146] expected at 1297 cm^{-1} ($v_{C=O}$) and 1691 cm$^-$

[1] $(v_{\text{C-OH}})$[147] are absence at pH_0 9.0 because only completely dissociated succinate is available in equilibrium. However, at pH_0 6.3 the fraction of dianion drops to 81.9% while succinate monoanion reaches an 17.9% justifying the observation of a peak at 1297 cm^{-1} for the symmetric $v_{\text{C-OH}}$ stretching of –COOH groups in Figure 4.8B. Therefore, DRIFT spectroscopy confirms the dianion of succinate depicted in Figure 4.9 is the dominant species both participating in the synthesis and accumulating in the interlayer space of sauconite in experiments at pH_0 9.0.

Total surface area measurements, TEM and cryo-TEM together with XRD and DRIFT spectroscopies reveal that the slow initial swelling during sauconite growth becomes exponentially faster after aluminum incorporation to the structure. The total surface area of the synthesized clay is a direct function of the amount of a simple dicarboxylic acid, which is an adsorbate in the interlayer space (Figure 4.9) and a catalyst for crystallization. Therefore, as the amount of organic salt increases, swelling occurs and the reactive surface growths exponentially. The associated retention of water in the interlayer space is enhanced for longer syntheses as indicated by the 2.2×10^3 expansion in TSA occurring when transitioning from 0 to 20 h for the data in Figure 4.8C. The surface charge density $\sigma_0 = -0.26 (\pm 0.04)$ C m^{-2} for the sauconite sample in Figure 4.8C at 20 h is in good agreement with the reported values for 2:1 phyllosilicate clay minerals.[116] Both TSA = 475 ($\pm$ 18) m^2 g^{-1} and the cation exchange capacity, CEC = 127 ($\pm$ 14) cmol$_{(+)}$ kg^{-1}, at 20 h in Figure 4.8C were employed to calculate σ_0.[116] Finally, Scherrer equation[148]

$$L_{hk} = \frac{K\lambda}{\beta \cos\theta} \tag{1}$$

with $K = 1.84$,[149] X-ray wavelength $\lambda = 1.5418$ Å, and a full width at half maximum $\beta = 3.4534 \times 10^{-2}$ radians for the baseline corrected (0 0 1) peak centered at $2\theta = 5.7892°$ can be used to estimate the mean crystallite size $L_{hk} = 8.2$ nm for the two-dimensional random layer lattice at 20 h in Figure 4.8C.

4.5 Conclusions

Because clay minerals contribute most of the inorganic surface to catalyze reactions in soil environments, these results provide new understanding of the continuous evolution of present agricultural fields. Overall, this laboratory study demonstrates an effective coupling between photochemistry mediated by semiconductor minerals and clay formation exists. The work also demonstrates the self-catalytic power of clays toward mineral formation in the geological past as well as the ability of simple central metabolic molecules to co-catalyze crystallization in short time scales. The co-catalytic role of succinate between layers is to provide soluble complexes of Al^{3+}, which is the limiting reagent for sauconite crystallization. Once the likely intercalation of succinate (or the other organic species) balances the relative adsorption forces between the precursor gel and the aluminum species, due to its bidentate ability, it can overturn the attraction forces between adjacent sauconite whiskers. A detailed description of the nucleation and growth of model clay particles is supported by cryogenic and conventional TEM. Finally, a major outcome of this work is that photochemistry may have played an important role in the origin of life on early Earth and other rocky planets.

4.6 Acknowledgements

4.7 Supporting Information for: Catalyzed Synthesis of Zinc Clays by Prebiotic Central Metabolites
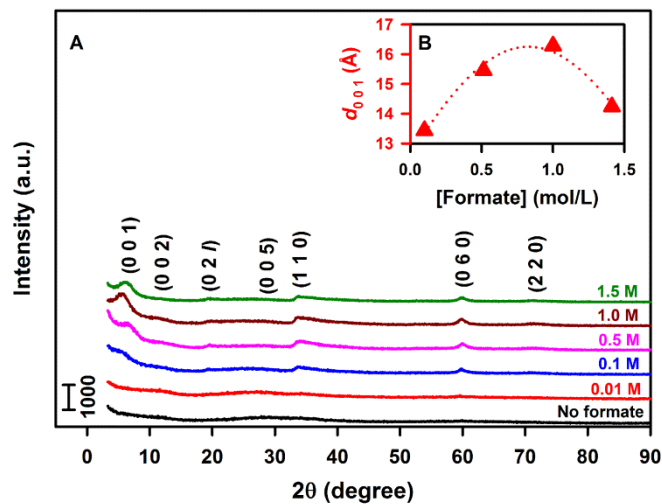
Figure S4.1 (A) Powder XRD diffractograms of sauconite synthesized at pH_0 6.3 at 90 °C during 20 h under the variable [formate] listed above each trace. Subscript numbers, e.g., (0 0 1), indicate basal reflections of the identified phases. (B) The layer to layer distance for 2:1 sauconite ($d_{0\,0\,1}$, red solid triangle) for traces in (A) vs [formate].
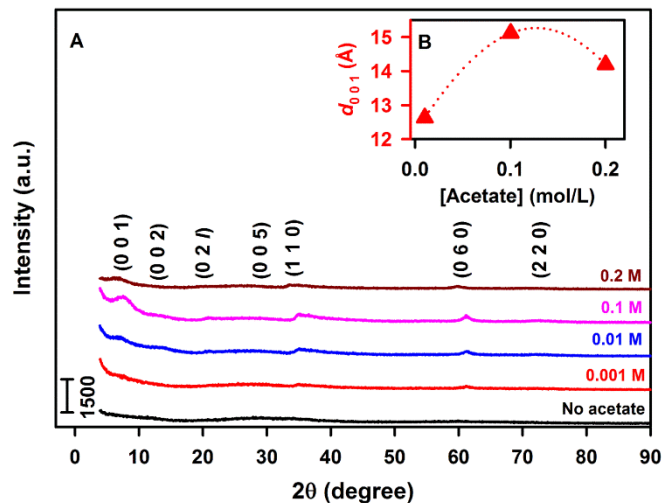
Figure S4.2 (A) Powder XRD diffractograms of sauconite synthesized at pH_0 6.3 at 90 °C during 20 h under the variable [acetate] listed above each trace. Subscript numbers, e.g., (0 0 1), indicate basal reflections of the identified phases. (B) The layer to layer distance for 2:1 sauconite ($d_{0\,0\,1}$) for traces in (A) vs [acetate].
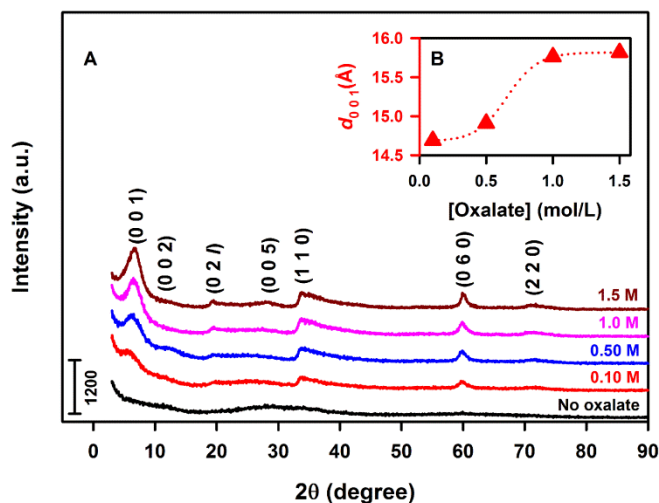
Figure S4.3 (A) Powder XRD diffractograms of sauconite synthesized at pH_0 6.3 at 90 °C during 20 h under the variable [oxalate] listed above each trace. Subscript numbers, e.g., (0 0 1), indicate basal reflections of the identified phases. (B) The layer to layer distance for 2:1 sauconite ($d_{0\,0\,1}$) for traces in (A) vs [oxalate].
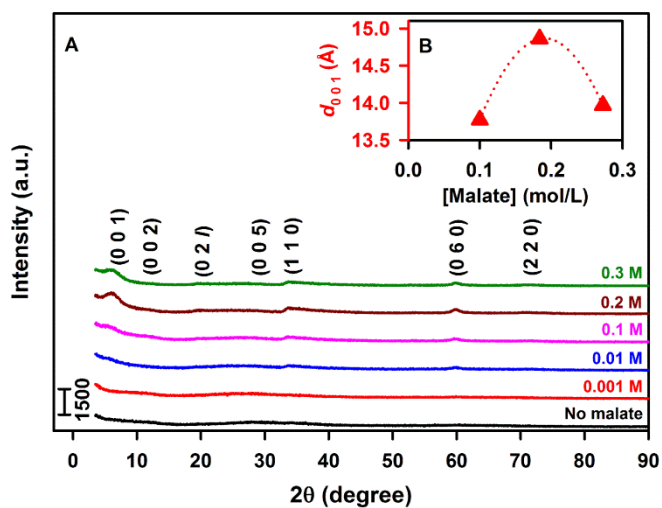
Figure S4.4 (A) Powder XRD diffractograms of sauconite synthesized at pH_0 6.3 at 90 °C during 20 h under the variable [malate] listed above each trace. Subscript numbers, e.g., (0 0 1), indicate basal reflections of the identified phases. (B) The layer to layer distance for 2:1 sauconite ($d_{0\,0\,1}$) for traces in (A) vs [malate].
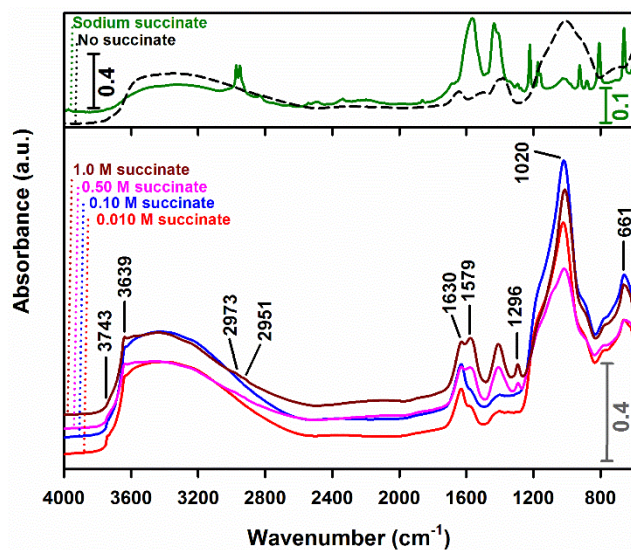
Figure S4.5 DRIFT spectra of sauconite synthesized under variable [succinate] for the same conditions of Figure 1 (20 h at pH_0 6.3 and 90 °C) compared to sodium succinate and the starting gel.
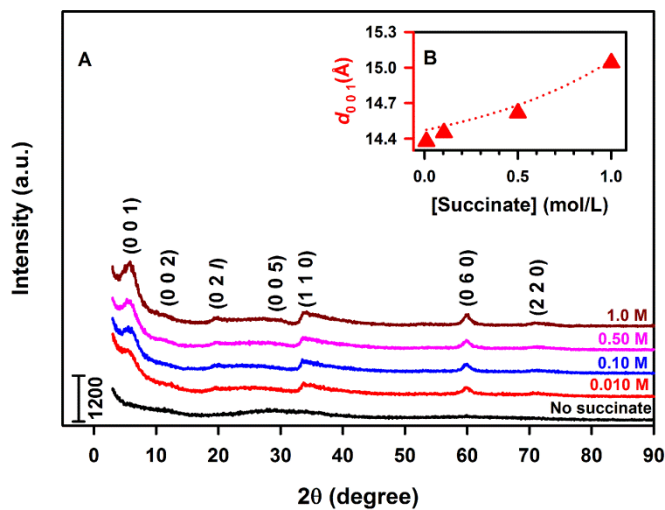
Figure S4.6 (A) Powder XRD diffractograms of sauconite synthesized at pH_0 6.3 at 90 °C during 20 h dried under room temperature instead of in the oven as in the other Figures. The variable [succinate] is listed above each trace. (B) The layer to layer distance for 2:1 sauconite ($d_{0\,0\,1}$) vs [succinate].
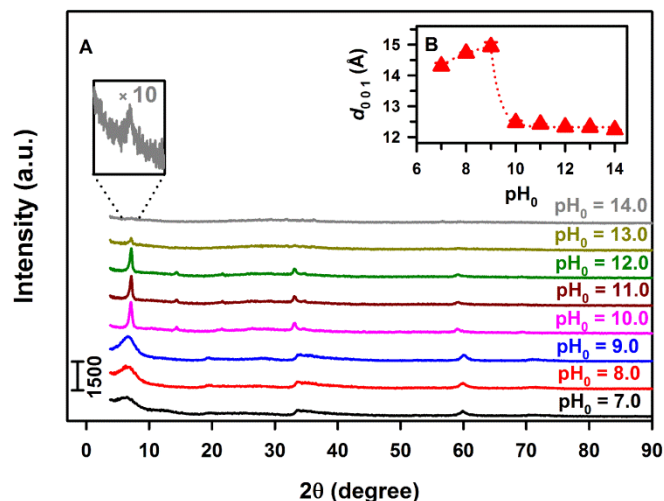
Figure S4.7 (A) Powder XRD diffractograms of sauconite synthesized with 1.0 M succinate at 90 °C during 20 h under the variable pH_0 values indicated over the traces. (B) The layer to layer distance for 2:1 sauconite, $d_{0\,0\,1}$ from $2\theta = 5.82°$ is (A) vs pH_0.
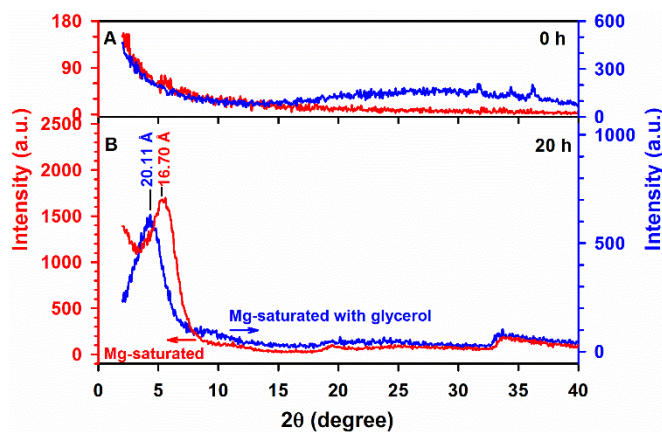
Figure S4.8 XRD patterns of (red) Mg-saturated and (blue) Mg-saturated with glycerol of synthesized sauconite with 1.0 M succinate at pH_0 9.0 and 90 °C for timepoints at (A) 0 and (B) 20 h.
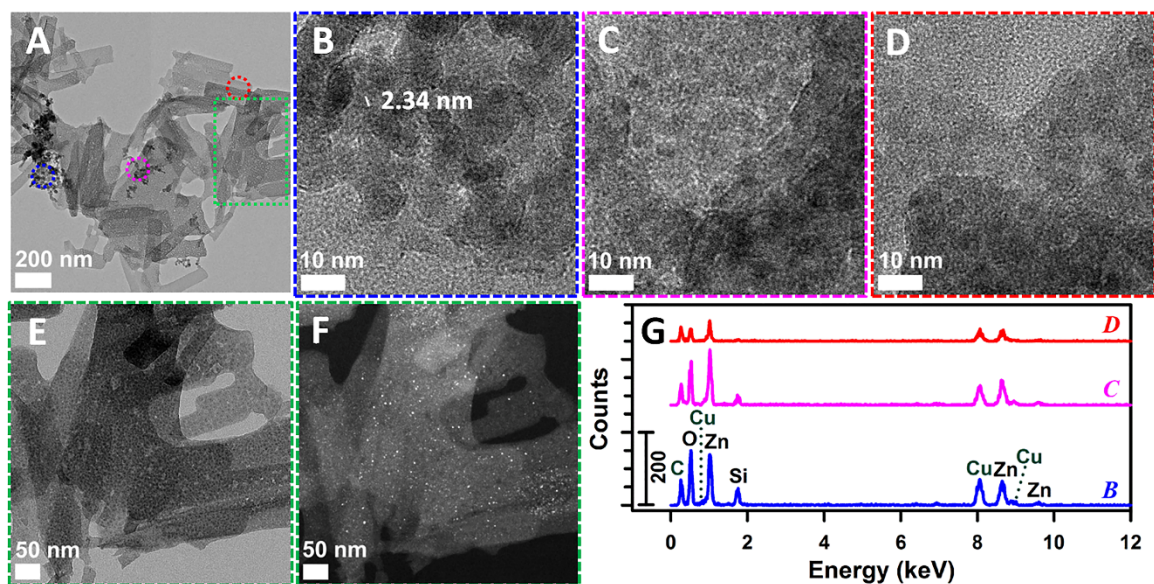
Figure S4.9 Transmission electron micrographs (TEM) and energy dispersive X-ray spectra (EDS) of initial gel with 1.0 M succinate and pH_0 9.0 before starting reflux showing morphologies in different parts. (A) Large region showing the inhomogeneity of the gel with fours demarked sections displayed in close-ups: (B) blue circle for thick-agglomerated microspheres; (C) pink circle for thin-agglomerated microspheres; (D) red circle for a more translucent region without microspheres; and (E and F) green square for the bright and dark field modes of a translucent region contrasting the presence of nanoscopic nuclei in the bulk structure but not on the surface. (G) EDS for the close-ups in panels A, B, and C.

Video M1-M4 are available at doi:10.1038/s41598-017-00558-1, Supplementary

Information.

Chapter 5. Cu$_2$O/TiO$_2$ Heterostructures for CO$_2$ Reduction through a Direct Z-scheme: Protecting Cu$_2$O from Photocorrosion
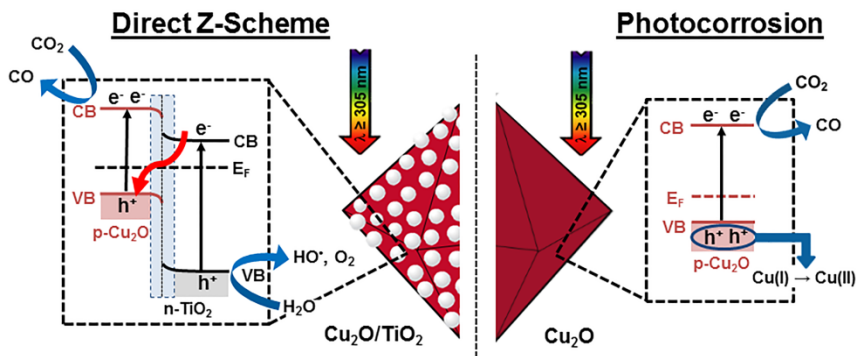
Scheme 5.1 Synopsis TOC

5.1 Synopsis

The development of artificial photosynthesis aims to solve the increasing energy demand and associated environmental problems. A model photosynthetic system employing a composite of semiconductors with a Z-Scheme can potentially mimic the combined power of photosystems 1 and 2 to transfer electrons. In this work, octahedral cuprous oxide covered with titanium dioxide nanoparticles (Cu_2O/TiO_2) are synthesized by a solvothermal strategy that provides high morphological and crystallographic control. The formation of a *p-n* heterojunction and characterization of the Type II band alignment of the composite are performed by diffuse reflectance UV-visible (DRUV) spectroscopy, ultraviolet photoelectron spectroscopy (UPS), and X-ray photoelectron spectroscopy (XPS). Upon UV-visible irradiation ($\lambda \geq 305$ nm) of the composite in the presence of water vapor as the hole scavenger, the photoreduction of $CO_2(g)$ proceeds selectively to generate $CO(g)$. The production rate of CO by the composite, $R_{CO} = 2.11$ μmol $g_{cat}^{-1} h^{-1}$, is 4-times larger than for pure Cu_2O under identical conditions. Contrasting XPS analyses of Cu_2O and Cu_2O/TiO_2, during photocatalysts operation and the detection of photogenerated hydroxyl radicals ($HO^{\bullet}$) in the heterostructure at variance with the results obtained for pure Cu_2O are taken as evidences that TiO_2 protects Cu_2O from undergoing photocorrosion. These results provide direct evidence of an efficient Z-Scheme as the main mechanism for harvesting energy during CO_2 reduction in the synthesized materials.

5.2 Introduction

The design of efficient photocatalysts aimed at the conversion of CO_2 to useful chemicals is a scientific challenge, which is driven by the shortage of energy resources and the increased concentration of this greenhouse gas in the atmosphere.[150-153] The high stability of the linear CO_2 molecule makes its reduction difficult and usually demands scarce and expensive species, such as ruthenium or rhenium complexes.[153-159] The use of heterogeneous photocatalytic systems involving TiO_2, ZnO, or ZnS provide a possible, although less efficient alternative for carbon dioxide reduction under UV excitation.[5, 8, 160] It should be noticed that none of these semiconductors provides sufficient potential to mediate the one electron reduction of CO_2 (Equation (1)), since their conduction bands lie below the homogeneous reduction potential of carbon dioxide, E^0 (CO_2/ $CO_2^{\bullet-}$) = -1.9 V.[161]

$$CO_2 + e^- \rightarrow CO_2^{\bullet-} \tag{1}$$

Although adsorption on semiconductor surfaces would certainly bend the linear CO_2 molecule and lower the energy demand for reaction 1, the considerable gap between the CO_2 LUMO and the conduction band (CB) probably prevents direct CO_2 reduction by CB electrons.[162] Thus, the photocatalytic reduction of CO_2 frequently involves the use of sacrificial donors (i.e., alcohols) that generate reactive intermediates (hydroxyalkyl radicals) which can accomplish reaction (1). It is also apparent that the low photon intermittency usually employed under practical photocatalytic experiments is against the

occurrence of multielectronic processes,[163] which could by-pass the high energy

intermediate $CO_2^{\bullet-}$.[9]

Cuprous oxide (Cu_2O) is an interesting *p*-semiconductor whose conduction band is

much more energetic than the commonly used wide bandgap semiconductors. The

bandgap of cuprous oxide is $E_{gap,2} \approx 2\text{-}2.2$ eV, while its conduction band is poised at $E_{CB,2}$

-1.4 eV vs NHE at pH = 7.[164] Unfortunately, as commonly found for semiconductors

active in the visible region its photostability is poor.[165] However, it can be envisaged that

surface modification of Cu_2O with a *n*-type wide bandgap semiconductor such as TiO_2

could generate a Type II heterostructure and avoid Cu_2O photocorrosion as discussed

below.

Scheme 5.2 shows the expected energy diagram for the Type II Cu_2O/TiO_2

heterostructure.[26]

Mechanism A

e^- $E_{CB,2}$

$E_{CB,1}$ e^-

$h\nu \geq E_{gap,2}$

h^+ $E_{VB,2}$

$h\nu \geq E_{gap,1}$

$E_{VB,1}$ h^+

TiO_2 Cu_2O

Mechanism B

e^- $E_{CB,2}$

$E_{CB,1}$ e^-

$h\nu \geq E_{gap,2}$

h^+ $E_{VB,2}$

$h\nu \geq E_{gap,1}$

$E_{VB,1}$ h^+

TiO_2 Cu_2O
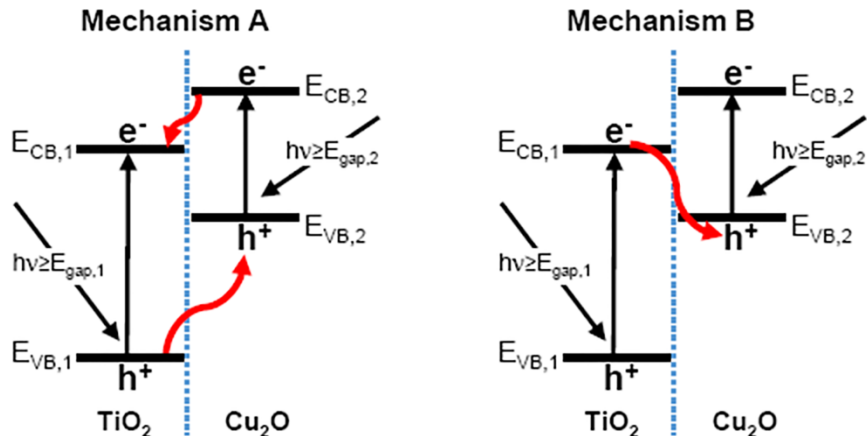
Scheme 5.2 Schematic representation of the processes that can take place in a system consisting of two semiconductors in electrical contact under irradiation with photons of suitable energy. (A) Double Charge Transfer, and (B) direct Z-Scheme mechanism.

Simultaneous excitation of the individual components of the composite leads to an electron-hole pair in each photocatalytic center. Different mechanisms can be envisaged to rationalize the charge transfer across the interface in *p-n* heterojunctions. Scheme 5.2A represents a double-charge transfer mechanism, in which the Cu_2O electrons move to the TiO_2 center and TiO_2 holes migrate to Cu_2O.[166-167] Alternatively, scheme 5.2B involves a direct Z-mechanism,[27, 168-170] where the TiO_2 electrons are used to scavenge Cu_2O holes. The double-charge transfer mechanism favors charge separation, at the expense of a decrease in the potential energy of electrons and holes. Moreover, it generates an excess of holes in Cu_2O that could lead to its photocorrosion in absence of a suitable electron donor. Instead, under the Z-mechanism the electron transfer across the interface could provide a way for preserving Cu_2O photostability while maintaining a high reduction potential. Both, mechanisms A and B (Scheme 5.1), have been previously invoked to

explain the higher efficiency of the heterostructures in comparison to the individual

counterparts; however, the factors favoring one of the two mechanisms remain elusive.

In this work, we synthesize and fully characterize a type II heterostructure based on

p-type octahedral Cu_2O and n-type TiO_2 nanoparticles. The synthetized material shows

an enhanced efficiency for CO_2 photoreduction in comparison to the individual materials.

Based on comparative X-ray photoelectron spectroscopy (XPS) studies of Cu_2O and

Cu_2O/TiO_2 heterostructures under UV-visible irradiation, we provide direct experimental

evidence in favor of the Z-Scheme mechanism.

5.3 Experimental Details

5.3.1 Chemical and Materials

Copper (II) chloride dihydrate ($CuCl_2 \cdot 2H_2O$, 99.4% assay, J. T. Baker),

Polyvinylpyrrolidone (PVP, average MW $\approx$ 29000 from Aldrich), Sodium Hydroxide

(NaOH, 99.3% assay, VWR), L-ascorbic acid (99.7% assay, Sigma-Aldrich), Ethanol

(absolute for analysis, 99.9% assay, EMD Chemicals) and Titanium (IV) butoxide

(97.0% assay, Sigma-Aldrich) were used as received. Carbon dioxide (CO_2, UHP) and

Carbon monoxide (CO, CP) were purchased from Scott Gross. All procedures employed

ultrapure water (18.2 MΩ.cm, ELGA PURELAB flex, Veolia).

5.3.2 Synthesis of Cu_2O Octahedra

Cu_2O synthesis closely follows a previous published procedure.[171] In a typical

experiment, 6.66 g of PVP were dissolved in an aqueous solution of $CuCl_2$. $2H_2O$ (0.01

mol L^{-1}, 100 mL) at 55 °C. Then, 10.0 mL NaOH aqueous solution (2.0 mol L^{-1}) was

added dropwise into the above transparent light green solution. During this process, the

solution color changes from blue-green to dark brown. The reaction mixture was stirred for 0.5 h, keeping the temperature at 55 °C. Afterwards, 10 ml of an aqueous ascorbic acid solution (0.6 mol L^{-1}) was added dropwise and the mixture was aged for 3 h under constant stirring and strict temperature control (55 °C). This last stage gradually produces a red suspension. The resulting precipitate was collected by centrifugation and washed consecutively with 10 ml of deionized water and absolute ethanol (5 times). Finally, the solid was dried under vacuum at 60 °C for 5 h for further use and characterization.

When mentioned a thermal treatment was applied to the as-synthesized solid. Briefly, the solid was resuspended in absolute ethanol, transferred to 200 mL Teflon-lined stainless steel autoclave and heated at 180 °C for 12 h in a programmable oven. An initial ramp of 1 °C min^{-1} was used to achieve the final temperature.

5.3.3 Preparation of TiO$_2$/Cu$_2$O

The modification of Cu$_2$O octahedral was performed following the procedure developed by Liu *et al.*[172] Briefly, 186 mg of Cu$_2$O were resuspended in 65 ml of absolute ethanol with the aid of ultrasonication for 30 minutes, and the suspension was cooled at 0 °C. At this temperature, 1.3 mL of titanium (IV) butoxide ethanolic solution (0.1 mol L^{-1}) were added dropwise into the Cu$_2$O suspension and stirred for 1 h at 0 °C. Afterwards, 6.5 mL of a water:ethanol solution (volume ratio 1:4) were added dropwise to the mixture under vigorous stirring for another hour. The reaction mixture was diluted with 98 mL of absolute ethanol, transferred to 200 mL Teflon-lined stainless steel autoclave and heated at 180 °C for 12 h in a programmable oven. An initial ramp of 1 °C min^{-1} was used to achieve the final temperature. The amount of Cu$_2$O and TiO$_2$ precursors used in this approach guarantee a nominal proportion of 0.05:0.95 of

$TiO_2:Cu_2O$ in weight. The product was collected by centrifugation and washed consecutively with 10 mL of deionized water and absolute ethanol (5 times). Finally, the solid was dried in vacuum at 60 °C for 5 h for further use and characterization.

Pure TiO_2 was obtained using the same solvothermal procedure described above, in absence of Cu_2O crystals.

5.3.4 Catalyst Characterization

The crystalline properties of the as-prepared samples were analyzed via powder X-ray diffraction (XRD). The analysis was carried out on a X'Pert PRO (PANalytical) powder X-ray diffractometer, with Cu K_α (1.54 Å) as the incident radiation and operated at an accelerating voltage of 40 kV with a current intensity of 40 mA.

The morphology of the samples was observed by scanning electron microscopy (SEM) using a Hitachi S-4300 instrument with an accelerating voltage of 25 kV. A ca. 10 µL drop of colloidal suspension in ethanol (10 mg mL^{-1}) was put on a SEM grid and dried under a red light lamp. The phase distribution in the Au-metallized samples, was analyzed by Energy-Dispersive X-ray Spectroscopy (EDS) by using a Jeol JSM-6460LV scanning electron microscope, operating at 15 kV coupled to a EDS probe Genesis XM4-Sys 60. X-ray photoelectron spectroscopy (XPS) measurements of the powdered samples were conducted using PHI VersaProbe II spectrometer with an Al K-α anode (1486.6 eV photon energy, 86.6 W). Ultraviolet photoelectron spectroscopy (UPS) studies were carried out by using a PHI 5600 system with He (10.2 eV) as monochromatic light source with a polarization potential (bias) of -5.0 eV. All values determined from UPS analysis are referred to vacuum. The diffuse reflectance UV-visible (DRUV) spectra of the powered samples were obtained with an Evolution 220, ISA-220 accessory, Thermo

Scientific UV−vis spectrophotometer using a built-in 10 mm silicon photodiode with a 60 mm Spectralon sphere. The ISA-220 accessory was used in a configuration to register the diffuse reflectance spectrum of dry solid powders as a Kubelka−Munk function against the certified Spectralon standard.[161]

5.3.5 Photocatalytic Studies

The photocatalytic experiments were performed in 135 cm^3 customized quartz photoreactor with flat circular windows (diameter = 5.08 cm). Based on the elemental distribution obtained by SEM-EDS analysis (See Figure S5.1, Supporting Information), 3 mL of suspensions of appropriate concentrations to deposit 30 mg of Cu_2O/TiO_2, 28.4 mg of Cu_2O, and 1.6 mg TiO_2 were uniformly deposited in one of the reactor windows, and left to dry overnight. The reactor was then filled with 1 atm $CO_2(g)$ saturated with water vapor by sparging the gas during 20 min (0.5 L min^{-1}) through a gas wash bottle. The reactor sealed with septa was kept in the dark for 1 hour before irradiation to ensure a homogenous internal atmosphere. UV-visible irradiation was performed with a collimated 1 kW high-pressure Hg (Xe) arc lamp provided with a water filter and a cut-off filter at $\lambda \geq 305$ nm (Newport) previously described.

The irradiance of the lamp was measured in the interval $305 \leq \lambda \leq 665$ nm with a calibrated radiometer (Ocean Optics). Gas aliquots of 0.5 cm^3 were taken from the reactor at different irradiation times for analysis by gas chromatography (SRI 8610C, Multiple Gas #3 GC) equipped with two columns (a silica gel HaySep D as column 1 and a MoleSieve 13X as column 2), a thermal conductivity detector (TCD), and a flame ionization (FID) detector interfaced to a methanizer. The irradiation of the photocatalyst and quantification of produced $CO(g)$ were performed at room temperature (20 °C).

Additionally, the reaction products were identified by FTIR spectroscopy using a 2.4 m path length infrared gas cell with ZnSe windows (PIKE) thermostatted at 100 °C mounted in an iZ10 FTIR module connected to an infrared microscope (Thermo Scientific Nicolet iN10).[122] Furthermore, photocatalyst alteration during irradiation was monitored by XPS using a Thermo-Scientific K-Alpha X-ray Photoelectron Spectrometer with an Al K-α anode (1486.6 eV photon energy, 300 W).

The formation of hydroxyl radicals (HO$^{\bullet}$) on the surface of irradiated Cu_2O/TiO_2 was quantified using the coumarin fluorescence method with a Lumina Fluorescence Spectrometer (Thermo Scientific) using excitation at $\lambda_{exc} = 332$ nm. While coumarin is a poorly fluorescent molecule, it is an excellent probe to quantify [HO$^{\bullet}$] trapped in the produced 7-hydroxycoumarin. 7-Hydroxycoumarin has a characteristic fluorescent signal at $\lambda_{em} = 456$ nm,[173] which is proportional to the formed [HO$^{\bullet}$].[174] The experimental procedure followed the same steps of the photoreduction experiments, except that 30 mg of coumarin (Alfa Aesar, 98.0%) were deposited on top of the 30 mg of nanocomposite thin film for a 1:1 mass ratio.[168] Each data point corresponds to individual irradiation experiments at times of 0, 1, 2, and 3 h. Controls in the dark and with the individual components were also performed. Samples were extracted with 51 mL of water,[168] centrifuged at 4400 rpm for 5 min, and forced through a filter (Acrodisc 0.2 μm pore size; Pall Corp.) to quantify by standard addition the 7-hydroxycoumarin (Acros, 98.5%) produced.

5.4 Results and Discussion

5.4.1 Selection of Cu_2O Shape and Composite Architecture

By modifying the reaction conditions, i.e., the relative amount between the capping agent and Cu_2O precursors, the shape of Cu_2O crystals can be easily modified from cubic to octahedra. This issue has attracted the attention of many researchers, who concluded that octahedral Cu_2O with exposed (1 1 1) faces exhibited much higher photocatalytic activity than the cubic structure.[175-177] It is apparent that crystalline (1 1 1) facets containing active Cu atoms can increase the interaction with donors and acceptors.[169, 178] Guided by these conditions, we choose Cu_2O octahedral as the starting point to design the composite.[30, 179] Also, since the hybrid composite would allow free access of the acceptor and donor to both surfaces, we regulated the concentration of the semiconductors precursors taking into account the individual size and surface area in order to warrant nearly all of TiO_2 nanoparticles cover the surface of Cu_2O and the amount of free TiO_2 nanoparticles is depreciable as verified by SEM analysis. The actual proportion in the composite was estimated by SEM-EDS analysis in 0.053:0.947 of TiO_2:Cu_2O in weight, in very good agreement with the nominal proportion (See Figure S5.1, Supporting Information).

5.4.2 XRD and SEM Analysis of Crystal Structure and Morphology

Figure 5.1 shows the X-ray diffraction patterns of the synthesized Cu_2O octahedra, TiO_2 and Cu_2O/TiO_2. For both Cu_2O and Cu_2O/TiO_2, all the peaks belong to the face-centered cubic Cu_2O phase (PDF Card No. 05-0667) and no diffraction peaks of CuO or metallic Cu could be detected. The strong and sharp peaks attributable to Cu_2O indicate a high degree of crystallinity. A low-intensity diffraction peak at $\theta = 25.08$ is present in the

Cu$_2$O/TiO$_2$ diffraction pattern, and ascribed to the (100) plane of anatase, as shown in the inset of Figure 5.1.

The XRD pattern of pure TiO$_2$ (Figure 5.1), obtained in a parallel synthesis is in agreement with the report for anatase (JCPDS 21-1272).
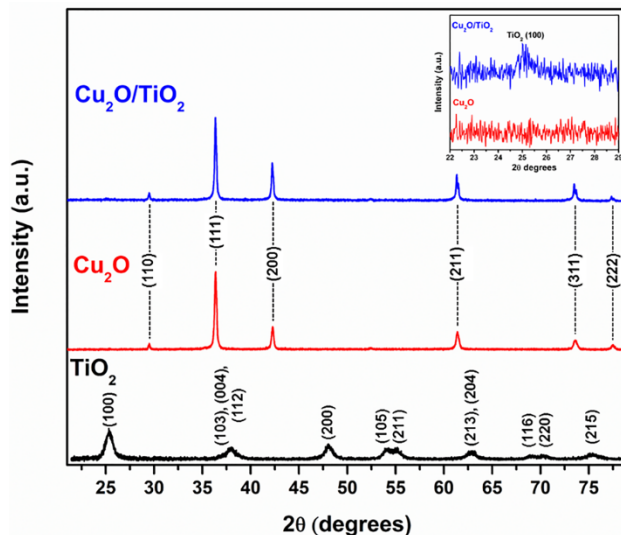
Figure 5.1 X- ray diffraction patterns of (blue) Cu$_2$O/TiO$_2$, (red) Cu$_2$O and (black) TiO$_2$. The crystal planes from JCPDS are shown between parentheses. Inset shows an enlarged view of the region between θ = 22-29° of (blue) Cu$_2$O/TiO$_2$ and (red) Cu$_2$O diffractograms.

SEM measurements, Figure 5.2(A, B), show that after solvothermal treatment of the titanium (IV) butoxide ethanolic solution in the presence of Cu$_2$O octahedral particles, fine TiO$_2$ nanoparticles cover Cu$_2$O (Figure 5.2(C, D)). It is also apparent that Cu$_2$O morphology is not altered by the thermal treatment, thus, the difference observed in the photocatalytic activity of the composite presented below cannot be attributed to changes in the surface chemistry of Cu$_2$O particles, but rather to the presence of TiO$_2$. Distribution phase was confirmed by EDS (Figure S5.1, Supporting Information).
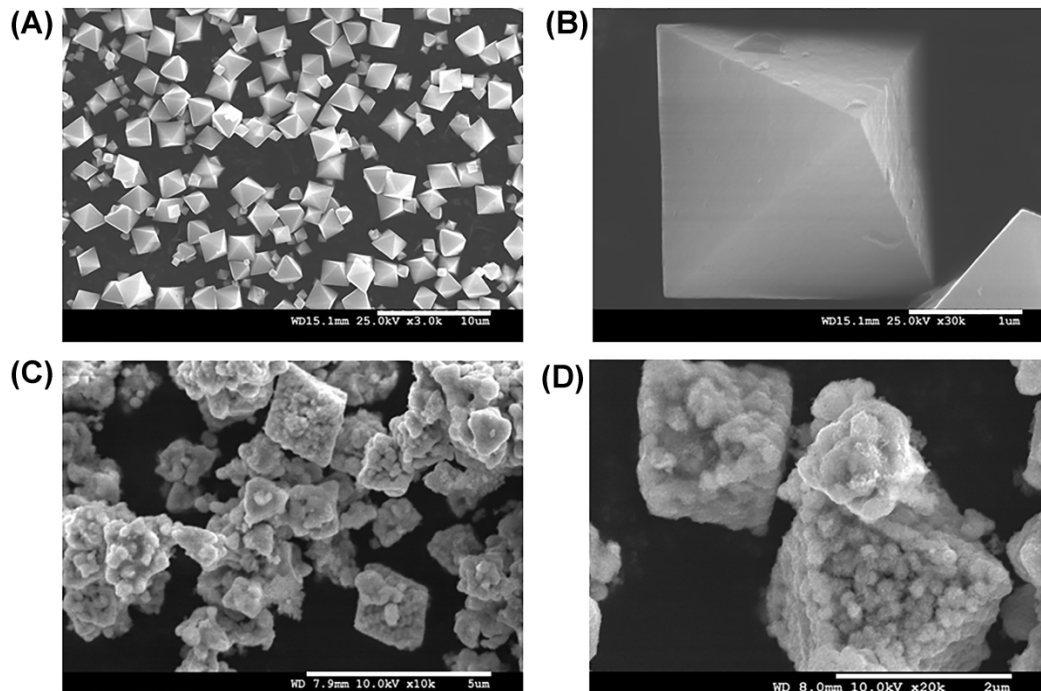
Figure 5.2 SEM images for (A, B) Cu_2O, (C, D) Cu_2O/TiO_2. The left hand side panels show images obtained with low magnification, while the aspect of isolated particles obtained with high magnification are shown at the right hand side.

5.4.3 Surface Characterization by XPS Analysis

Figure 5.3A shows the XPS survey spectrum for Cu_2O/TiO_2 composites, which demonstrates the existence of Cu, Ti and O in the sample. The C $1s$ peak, associated to the widespread presence of carbon in the environment is also clearly observed. Fig. 5.3B compares the high resolution XPS spectrum in the region of Cu $2p_{3/2}$ for pure Cu_2O and Cu_2O/TiO_2 composite. The same deconvolution procedure was applied throughout the analysis of the peaks and basically involves the subtraction of a Shirley-type baseline and the use of Voigt-type functions to reproduce the spectra. For Cu_2O the main peak is centered at 932.01 eV and is readily assigned to Cu^+,[180] while the shake-up satellite peaks with higher binding energy (933.98, 942.46, 943.98 eV) confirm the presence of an unfilled Cu $3d$ shell corresponding to Cu^{2+} species at the Cu_2O surface. This observation

has been commonly attributed to the oxidation of Cu^+ during sample preparation for analysis.[181] For the Cu_2O/TiO_2 composites, the position of the peaks is similar (See Figure 5.3B) but the relative area Cu(I):Cu(II) obtained through the deconvolution of Cu $2p_{3/2}$ spectrum changes from 0.75:0.25 (for pure Cu_2O) to 0.65:0.35 (in Cu_2O/TiO_2 composites). The previous information together with the results from XRD diffractograms suggests that a minimum fraction of surface copper changes its electronic state during the solvothermal treatment.

The high resolution XPS spectrum of Ti $2p$ in Cu_2O/TiO_2 can be adjusted with great accuracy with two Voigt-type functions centered in 458.31 and 464.19 eV that can be assigned at Ti $2p_{3/2}$ and Ti $2p_{1/2}$, respectively for Ti(IV)[182] in agreement with the results obtained for pure TiO_2 (Figure S5.2, Supporting Information). The deconvolution peaks of the O $1s$ spectrum for the Cu_2O/TiO_2 requires a greater number of components than for Cu_2O and in particular, three curves centered in 530.01, 532.08 and 533.63 eV are necessary. The two last components could be assigned to hydroxyl groups and water molecules adsorbed on the TiO_2 surface.[183-184] It should be noticed that the hydroxylation and the presence of adsorbed water molecules benefits CO_2 photoreduction[168] (See Supporting Information Figure S5.3, for details).
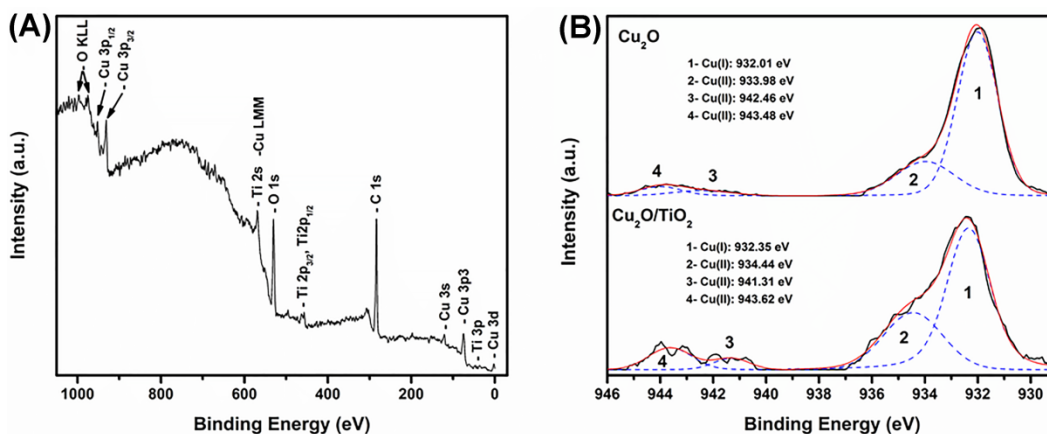
Figure 5.3 (A) XPS survey spectrum for Cu_2O/TiO_2 composite. (B) high resolution spectra for Cu2p$_{3/2}$ (peak 1) and shake-up satellite peaks (2, 3, and 4) in Cu_2O (top) and Cu_2O/TiO_2 (bottom) are shown as black solid lines. For comparison, the deconvoluted components (blue dash line) and the total fit from the sum of the components (red solid line) are also shown. See text for details.

5.4.4 Optical Properties and Energy Bands Alignments at the Heterojunction

Assessing the bands edge positions of Cu_2O and TiO_2 and the band alignment is important to understand the electron transfer process at the heterojunction and to determine the reactions that are thermodynamically feasible. The combined information from DRUV, UPS and XPS spectroscopies was used to determine electronic band alignments and the construction of the band energy diagram as discussed below.

DRUV spectra of Cu_2O, pure TiO_2, and Cu_2O/TiO_2 are shown in Figure 5.4A. The absorption edges for pure Cu_2O and TiO_2 samples were approximately 600 and 390 nm, respectively. Analysis of Tauc plots indicates that the optical bandgaps are $E_{BG}(Cu_2O) = 2.03$ eV, (as a direct semiconductor) and $E_{BG}(TiO_2) = 3.16$ eV, (as an indirect semiconductor)[185-186] (Figure S5.4, Supporting Information). These figures agree with the previously reported values for Cu_2O[187] and TiO_2[161].
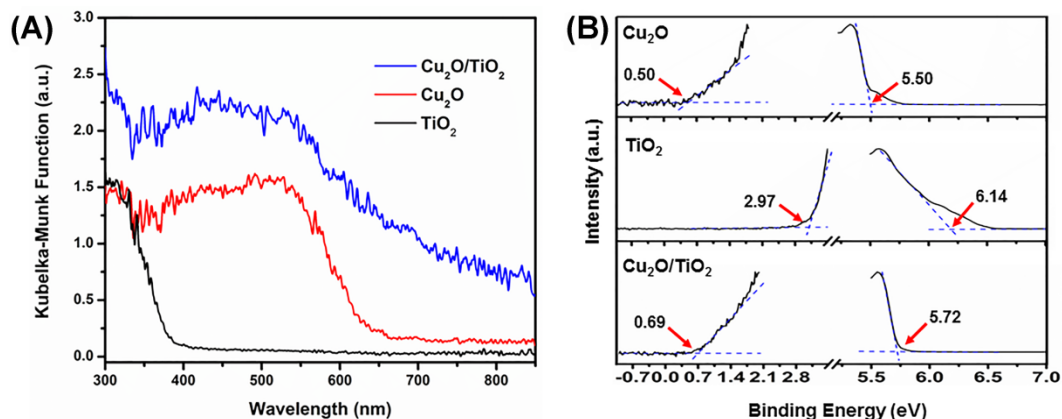
Figure 5.4 (A) UV-visible absorption spectra for solid samples. (B) UPS spectra for Cu$_2$O octahedral (top), pure TiO$_2$ (center), and Cu$_2$O/TiO$_2$ heterostructure (bottom). Extrapolations to the left and right hand sides correspond to the onset values for the valence band and secondary electron cut-off, respectively. A complete description is available in the Supporting Information (see Figure S5.5).

Figure 5.4B shows the UPS spectra of Cu$_2$O, TiO$_2$ and Cu$_2$O/TiO$_2$. By applying the method of linear approximation to the UPS spectra, the work function and the corresponding energy of the Fermi level of Cu$_2$O were estimated to be 4.70 and −4.70 eV, respectively. Similarly, the valence band maximum was calculated to be −5.20 eV. Considering the average bandgap energy value (2.03 eV for Cu$_2$O) obtained from the Tauc plots (Figure S5.4, Supporting Information), the minimum of the conduction band is located at -3.17 eV. The quantities previously determined are referred to the vacuum level. Therefore, according to the relationship between the potential of the normal hydrogen electrode (NHE), E°, and the energy of the vacuum (E_{abs}), $E_{abs} = - E^{\circ} - 4.44$ (at 298 K), the conduction and valence bands of Cu$_2$O are poised at −1.27 and 0.76 eV, respectively. Similarly, following this procedure for TiO$_2$, the estimated Fermi level (E_F), CB and VB vs NHE are −0.38, −0.57 and 2.59 eV, respectively (Figure S5.5, Supporting Information).

After contact, the Fermi levels of Cu_2O and TiO_2 equilibrate due to the formation of a *p-n* heterojunction at the interface of the Cu_2O/TiO_2 composite.[188] This process alters the band positions, as observed by XPS. Figure S5.5 in the Supporting Information provides the XPS spectra. The band alignment at the interface of Cu_2O/TiO_2 was determined following the method of Kraut.[189] To accurately determine the valence band offset, ΔE_{VBO}, the energy difference between the core level (E_{CL}) and the valence band maximum (E_{VBM}) in the pure materials, as well as the energy difference between the core levels at the interface of the heterostructure (ΔE_{CL}^{Int}) are needed. Eq. 2 and 3 are used to calculate ΔE_{VBO} and ΔE_{CL}^{Int}, respectively:

$$\Delta E_{VBO} = \left(E_{CL}^{Cu_2O} - E_{VBM}^{Cu_2O}\right) - \left(E_{CL}^{TiO_2} - E_{VBM}^{TiO_2}\right) + \Delta E_{CL}^{Int} \tag{2}$$

$$\Delta E_{CL}^{Int} = \left(E_{CL}^{TiO_2} + E_{CL}^{Cu_2O}\right)^{Cu_2O/TiO_2} \tag{3}$$

The conduction band offset, ΔE_{CBO}, can be readily obtained from the bandgap energies (E_{BG}) of the pure materials and ΔE_{VBO}:

$$\Delta E_{CBO} = E_{BG}^{Cu_2O} - E_{BG}^{TiO_2} + \Delta E_{VBO} \tag{4}$$

Combining the information gathered during XPS and DRUV analyses reveals that for the nanocomposite $\Delta E_{VBO} = 1.93$ eV and $\Delta E_{CBO} = 0.81$ eV (Figure 5.5). The energy difference between the conduction and valence bands for the materials in the composite are about 0.11 eV higher than the values before contact. From the previous observation

and the onset value of the composite (Figure 5.4B), the valence band maximum of Cu_2O in the composite is calculated to lie at 0.62 eV (vs NHE). The last figure is useful to calculate the apparent bandgap of Cu_2O in the composite, which together with ΔE_{VBO} and ΔE_{CBO}, is needed to estimate the minimum of the conduction band of Cu_2O in the composite is -1.39 eV (vs NHE) and the valence band maximum and conduction band minimum of TiO_2, which are depicted at 2.55 and −0.58 eV in Figure 5.5, respectively.[26]

Figure 5.5 shows the energy diagram indicating the formation of a Type II (staggered) band heterostructure, whose highly energetic conduction band favors the reduction of CO_2 through photogenerated electrons. We assume that the assignment of the composite bands corresponds to values that are far from the Cu_2O/TiO_2 interface. Taking into account this observation, and considering that the energy differences between CB and E_F for TiO_2 as well as from VB and E_F for Cu_2O do not remain constant before and after contact, we showed in Fig. 5.5 the associated band bendings.[190-192]
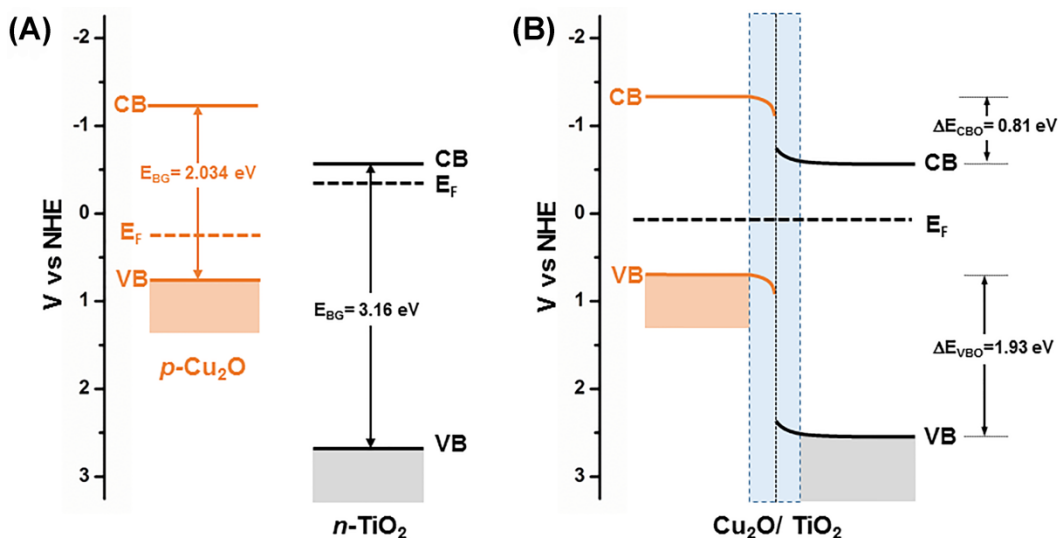
Figure 5.5 Energy band diagrams for (A) Cu_2O and TiO_2 before contact and (B) Cu_2O/TiO_2 composite.

The energy difference between the valence band maximum of Cu_2O and the conduction band minimum of TiO_2 can be estimated as 1.33 and 1.2 eV for the separated semiconductors and the composite, respectively. This change indicates that under UV-visible irradiation, the electron transfer from the conduction band of TiO_2 to the valence band of Cu_2O (direct Z-Scheme) could be favored due to the increased overlap of energy levels involved upon *p-n* heterojunction formation.

5.4.5 Photocatalytic CO_2 Reduction

Irradiation of the composite with $\lambda \geq 305$ nm results in the selective formation of CO, (and O_2). The time series for CO evolution from the irradiated composite is shown in Figure 5.6 together with the results obtained under similar conditions for pure Cu_2O and TiO_2. Control experiments for Cu_2O/TiO_2 showed that no CO evolved in the dark or when the irradiation was carried out in the absence of CO_2 under 1 atm argon (Figure S5.6, Supporting Information).
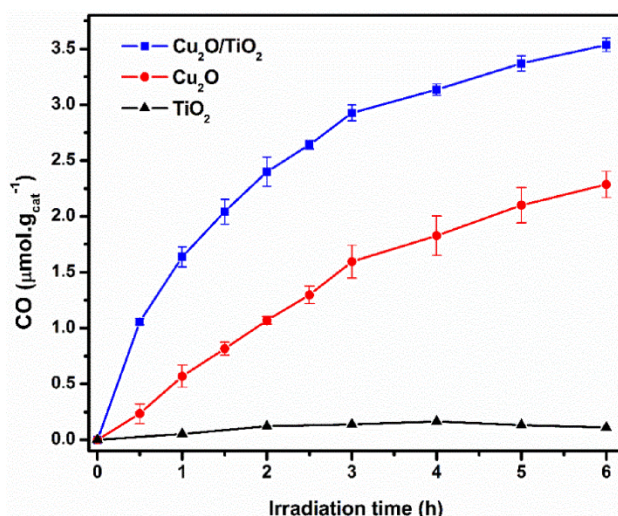
Figure 5.6 Carbon monoxide evolution over Cu_2O/TiO_2 heterostructure (blue), Cu_2O (red) and TiO_2 (black) under UV-visible irradiation ($\lambda \geq 305$ nm).

It is apparent from the results in Figure 5.6 that the formation of the *p-n* heterojunction improves the CO_2 reduction efficiency. Considering the same initial stage of irradiation, the CO evolution rates were calculated to be 2.11 and 0.55 µmol g_{cat}^{-1} h^{-1} for Cu_2O/TiO_2 and Cu_2O, respectively, which represents a ca. 4-times enhancement for the composite. The ratio from the areas for the convolution of the irradiance of the lamp with the DRUV spectra of 1) Cu_2O/TiO_2 and 2) Cu_2O in the interval $305 \leq \lambda \leq 665$ nm indicates the nanocomposite absorbs ca. 2-times more photons than Cu_2O per unit mass under the experimental conditions in Figure 5.6 Thus, only a 50% of the enhanced photocatalytic activity can be explained to arise from an increment in the oscillator strength (or the resulting increase of the integrated absorption per unit mass). Therefore, the synergistic effect from the materials in the nanocomposite is proposed to provide the remaining 50% photocatalytic enhancement.

The ratio of quantum efficiencies for CO production, Φ_{CO}, for Cu_2O/TiO_2 and Cu_2O can be easily calculated from the established relationships between the initial reaction rates ($R_{0,CO}$) and the absorbed photon fluxes I_a, which was established in the response to the previous comment,

$$\frac{\Phi_{CO}^{Cu_2O/TiO_2}}{\Phi_{CO}^{Cu_2O}} = \frac{R_{0,CO}^{Cu_2O/TiO_2}/I_a^{Cu_2O/TiO_2}}{R_{0,CO}^{Cu_2O}/I_a^{Cu_2O}} = \frac{R_{0,CO}^{Cu_2O/TiO_2}}{R_{0,CO}^{Cu_2O}} \times \frac{I_a^{Cu_2O}}{I_a^{Cu_2O/TiO_2}} = \frac{4}{1} \times \frac{1}{2} = 2 \qquad (5)$$

Therefore, the relative quantum efficiencies in Eq (5) clearly demonstrate that Cu_2O/TiO_2 has an enhanced photocatalytic activity over Cu_2O.

Another point of interest is that the evolution of CO decreases with the irradiation time. This is a characteristic of many photocatalytic process[161] and, in particular, has been observed for the photocatalytic CO_2 reduction over α- Fe_2O_3/Cu_2O[168], and over pure Cu_2O and $Cu_2O/RuOx$ systems.[193] The actual reason for this behavior is not well understood, and possible causes for the non-linear time profile are commonly ascribed to the strong interaction between Cu_2O and CO, or the formation of O_2, which competes with carbon dioxide reduction.[192] To get more insight, we investigate the rate of CO evolution in repeated 1 h irradiation cycles. After each run, the reactor was thoroughly evacuated and re-loaded with the same amount of CO_2 and H_2O before irradiation. Figure 5.7 shows that after 4 cycles, CO yields slightly diminish, in sharp contrast with the results obtained under continuous irradiation. These experiments indicate that the inhibition observed in Figure 5.6 is not irreversible, and the catalyst may be recycled without significant loss of efficiency, if the products are periodically removed.
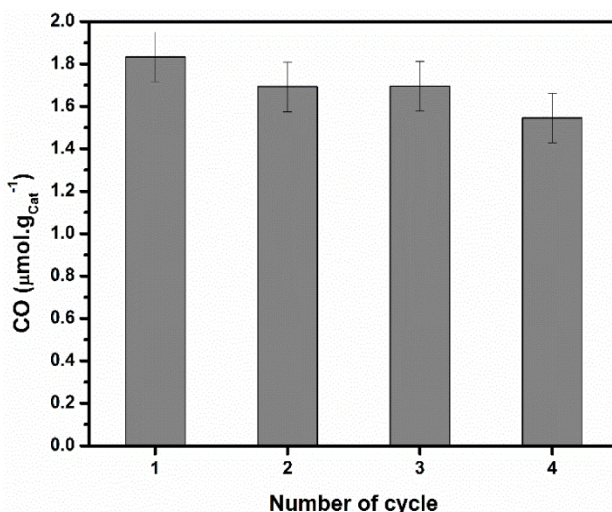
Figure 5.7 Carbon monoxide production during 1 hour-period in the recycling experiments (see text for details).

5.4.6 Analysis of the Reaction Mechanism

As discussed above, two different schemes commonly referred as (A) *double charge transfer* and (B) *direct Z-Scheme mechanisms* are often proposed to explain the electron transfer processes across the interface in *p-n* heterojunctions after the simultaneous excitation of the centers of Type II heterostructures.[26, 194] To determine which of these two mechanisms is operative, the photocatalyst was separated from the reactor and analyzed by XPS after different photons doses to monitor the possible change in the copper oxidation state during the irradiation experiments. The most relevant results are summarized in the Table 5.1, which details are provided in Supporting Information Figure S5.7.

Table 5.1 Summary of XPS analysis for Cu_2O and Cu_2O/TiO_2 photocatalysts at different irradiation times.

	Relative Components		Relative Components	
	Cu_2O		Cu_2O/TiO_2	
Irradiation time (h)	Cu (+)	Cu (2+)	Cu (+)	Cu (2+)
0	0.75	0.25	0.65	0.35
3	0.69	0.31	0.64	0.36
6	0.60	0.40	0.65	0.35

As shown in Table 5.1, XPS analysis of pure Cu_2O shows a relative increment of the contribution of Cu(II) in the $Cu2p_{3/2}$ in relation to the Cu(I) content. Cu_2O photocorrosion might have been anticipated since Cu_2O irradiation generates a highly reductive conduction band electron, $E_{CB} = -1.27$ eV, but a valence band hole with insufficient energy to oxidize water[162] (Scheme 5.3A). This key point is also demonstrated during experiment presented below that have quantified the production of HO radicals.

By contrast, in the Cu_2O/TiO_2 composite, the ratio Cu(II)/Cu(I) keeps constant along the entire photocatalytic reaction. To account for these results, we proposed that UV-visible irradiation induces the formation of an electron/hole pair in each photocatalytic center, Eq. (6):

$$Cu_2O/TiO_2 + h\nu_{(UV-visible)} \rightarrow Cu_2O(e_{CB}^-, h_{VB}^+)/TiO_2(e_{CB}^-, h_{VB}^+) \qquad (6)$$
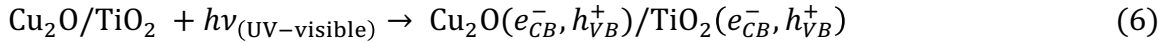
and after carrier generation, the electrons in the conduction band of TiO_2 are transferred to Cu_2O (see Scheme 5.2B):

$$Cu_2O(e_{CB}^-, h_{VB}^+)/TiO_2(e_{CB}^-, h_{VB}^+) \rightarrow Cu_2O(e_{CB}^-)/TiO_2(h_{VB}^+) + heat \qquad (7)$$
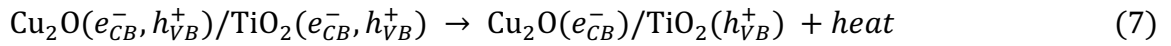
and the TiO_2 holes localize on surface oxygen, forming $(Ti^{3+})_{latt}$ and $(Ti^{4+}O^{\bullet-})_{surf}$ paramagnetic species, respectively. By these processes, we achieved a heterostructure with strongly reductive electrons, $Cu_2O(e_{CB}^-)$, and oxidative holes, $TiO_2(h_{VB}^+)$, able to oxidize water. Water oxidation by TiO_2 is not only thermodynamically allowed but also kinetically feasible as revealed by EPR experiments, which indicate that surface trapped

holes react with adsorbed molecules even at the extremely low temperatures used in the EPR studies.[195]

$$TiO_2(h\nu_{VB}^+) + H_2O \rightarrow HO^\bullet + H^+ \tag{8}$$

The fluorescence spectra for the production of 7-hydroxycoumarin during irradiation of Cu_2O/TiO_2 is presented in Figure S5.8 (Supporting Information). The characteristic fluorescence peak at $\lambda_{em} = 456$ nm matches the reported spectrum of 7-Hydroxycoumarin,[174] which implies that only this species is produced.[173] Importantly, no peak for 7-hydroxycoumarin production was observed during 1) a dark control with Cu_2O/TiO_2, or 2) irradiated Cu_2O. These controls strongly support the assignment of $HO^\bullet$, an important intermediate for O_2 production, as a unique product from the photoactivity of the nanocomposite. The linear relationship between fluorescence intensity and irradiation time (Figure S5.8, Supporting Information) indicates a constant production rate for 7-Hydroxycoumarin. Consequently, the production of $HO^\bullet$ displayed in the inset of Figure S5.8 (Supporting Information) is enabled by standard addition of 7-hydroxycoumarin to the samples. From the slope of the inset in Figure S5.8 (Supporting Information), the production rate of $HO^\bullet$ is 0.22 ($\pm$ 0.03) μmol g_{cat}^{-1} h^{-1}. Comparatively, after 3 h of irradiation, the rate of production of CO is 5-times larger. By correcting the previous rates in a per photon basis using the stoichiometric consumptions of 2 e_{CB}^- and 1 h_{VB}^+ for CO and $HO^\bullet$ species produced, respectively, indicates that 40% of the theoretical amount of $HO^\bullet$ is trapped in 7-hydroxycoumarin. The previous observation is not surprising for $HO^\bullet$, a high reactivity and short lived species with a lifetime $\tau \sim 1$ ns.[174]

In the presence of CO_2, additional evidence of water oxidation by Cu_2O-TiO_2 nanostructures, comes from the analysis of the ratio between CO and O_2 yields. After 1 hr of irradiation, we determined CO/ μmol g^{-1} cat = 1.69 ± 0.12 and O_2 / μmol g^{-1} cat = 0.83 ± 0.06, which gives CO/O_2 = 1.69:0.83 = 2.03, in close agreement with the expected reaction stoichiometry.

According to the Z-Scheme, the anodic reaction takes place in the Cu_2O surface. In this regard, it is interesting to notice that the one electron homogeneous reduction potential for the monoelectronic reduction of CO_2 (Eq. (1)), is more negative than the conduction band level of Cu_2O (E_{CB} (Cu_2O) = −1.39 eV). Thus, in order to make the CO_2 reduction thermodynamically feasible, some stabilization must be invoked.[196-197] Alternatively, rapid hole scavenging by adsorbed molecular water could lead to electron accumulation in Cu_2O, and reduce CO_2 by a two-electron process,

$$2\ e^{-}_{CB,Cu_2O} + CO_2 + 2\ H^+ \rightarrow CO + H_2O \tag{9}$$

with lower energy demand (E°(CO_2/CO) = −0.53 V),[198] avoiding the formation of the high energy intermediate, $CO_2^{\bullet-}$. However, current evidence does not allow distinguishing between the two possibilities.
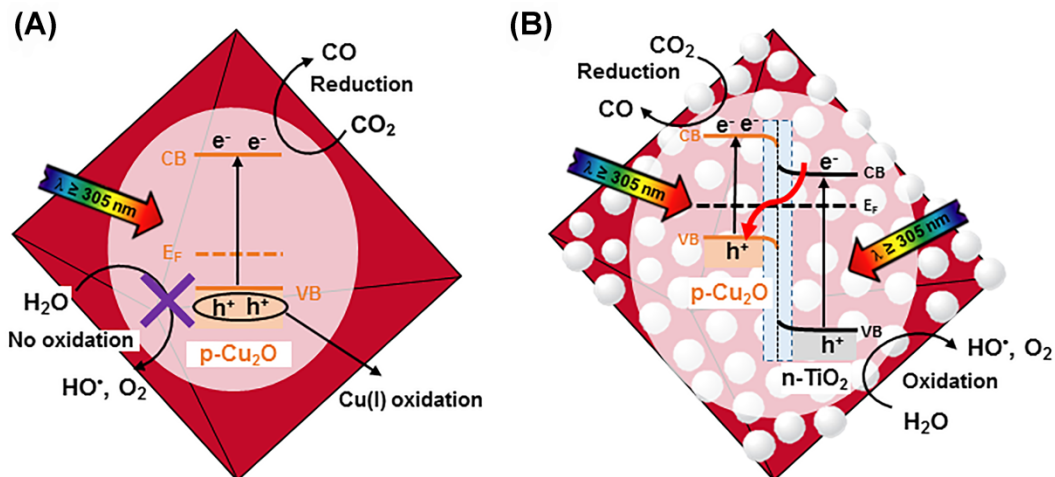
Scheme 5.3 Sketch of the proposed mechanism to account for CO_2 reduction induced by UV-visible irradiation ($\lambda \geq 305$ nm) of (A) octahedral Cu_2O and (B) Cu_2O/TiO_2 composite.

5.5 Conclusion

A Cu_2O/TiO_2 photocatalyst with high morphologic and crystallographic quality was synthetized by a simple solvothermal method. The new material shows a 4-times enhancement for the photoreduction rate of CO_2 induced by UV-visible irradiation in comparison to pure Cu_2O. Detailed analyses of the photocatalysts by XPS spectroscopy under operation, as well as the formation of OH radicals in the Cu_2O-TiO_2 system, at variance with the results for pure Cu_2O, unequivocally prove a Z-Scheme mechanism. The results obtained are of practical interest for photocatalysis and are also relevant for the understanding of photoinduced interfacial charge-transfer processes at the *p-n* heterojunction.

5.6 Acknowledgements

5.7 Supporting Information for: Cu₂O/TiO₂ Heterostructures for CO₂ Reduction through a Direct Z-scheme: Protecting Cu₂O from Photocorrosion

SEM-EDS analysis of Cu₂O octahedra and Cu₂O/TiO₂ nanocomposite
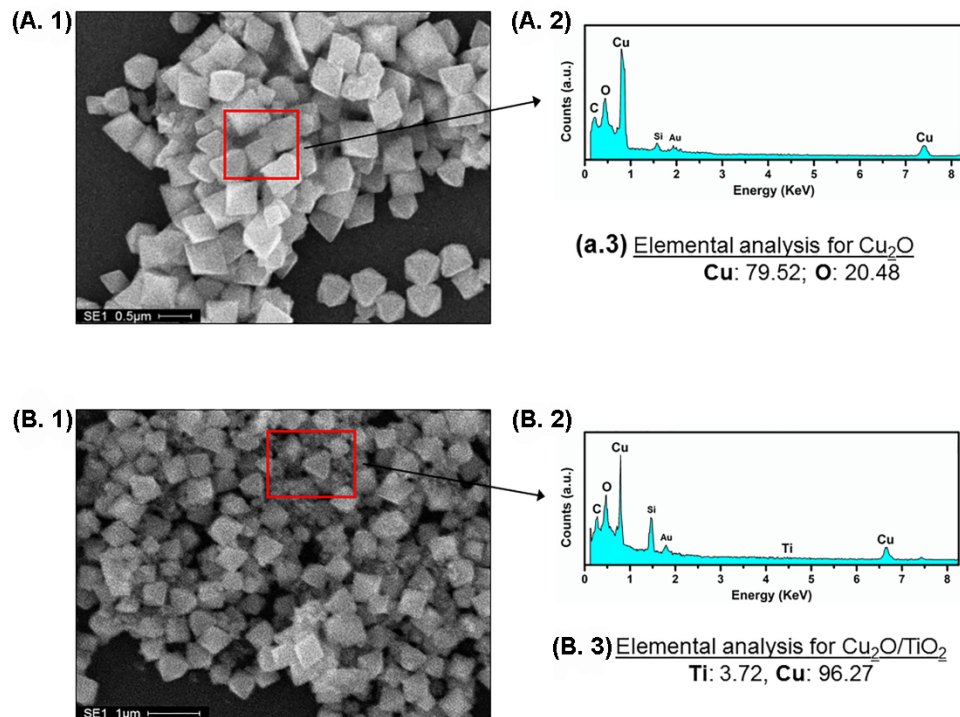
Figure S5.1 (1) SEM images, (2) EDS spectra for the region indicated by the arrow and (3) elemental analysis by EDS that result on the place marked by the colored cross in the expressed in weight percent (wt.%) for Cu₂O octahedra (panel A) and Cu₂O/TiO₂ composite (panel B).

XPS analysis and curve fitting of the Ti2p peaks

The experimental spectra and curve fit are shown with black hollow points and red solid lines, respectively. The peaks are centered at 458.31 and 464.19 eV for Ti $2p_{3/2}$ and Ti $2p_{1/2}$, respectively, which indicates the tetravalent state of Ti in both cases.[182]
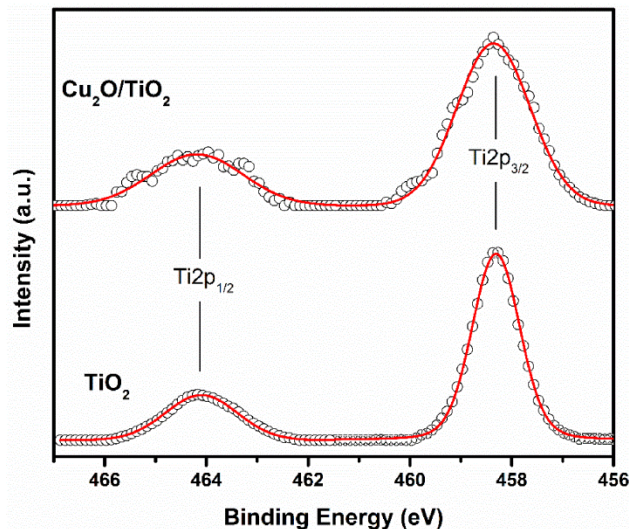
Figure S5.2 High resolution spectra in the region of Ti2*p* in (upper) Cu_2O/TiO_2 composite and (lower) TiO_2.

XPS analysis and curve fitting of the O1s peak

For the Cu_2O, the small peak centered at 529.7 eV may be attributed at oxygen in the CuO lattice,[199] while the peak at 531.3 eV corresponds to lattice oxygen O^{2-} and -OH groups in the Cu_2O phase.[181, 199]

The peaks centered at 529.6, 531.95 and 533.36 eV in the TiO_2 spectra may be attributed to lattice oxygen O^{2-}, hydroxyl groups and water molecules adsorbed, respectively.[183-184]

Based on these assignations, the lowest binding energy of O1s peak in Cu_2O/TiO_2 spectra at 530.01 eV can be mostly ascribed to oxygen O^{2-} in the lattice of TiO_2. The peak centered at 532.08 eV could be assigned as oxygen O^{2-} and -OH groups in the Cu_2O and -OH groups on TiO_2 surface. The last peak at 533.63 eV is presumably due to water molecules adsorbed on the surface of TiO_2 and Cu_2O.
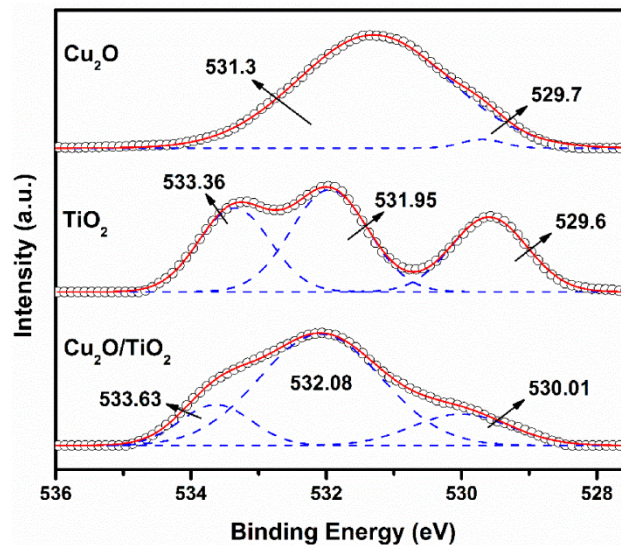
Figure S5.3 High resolution spectrum in the region of O1*s* in (upper) Cu_2O octahedra, (middle) TiO_2 nanoparticles and (lower) Cu_2O/TiO_2 composite. The graph shows the experimental spectrum (black hollow points), the components obtained from the adjustment (blue dash line) and the total fit obtained from the sum of the components (red solid line).

Optical bandgaps
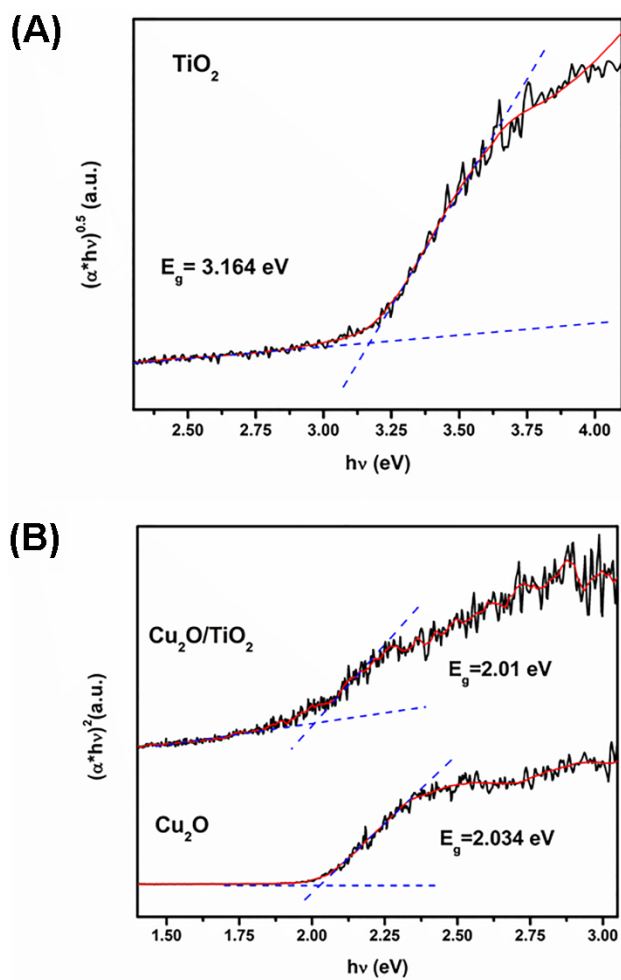
Figure S5.4 Tauc plots $(F(R) \times h\nu)^n$ vs $h\nu$ for (A) TiO_2 and (B) for (upper) Cu_2O/TiO_2 composite and (lower) Cu_2O octahedra; considering n= 0.5 and n= 2 for indirect and direct semiconductor, respectively.

XPS core level and valence spectra of samples and determination of the band positions in the photocatalysis
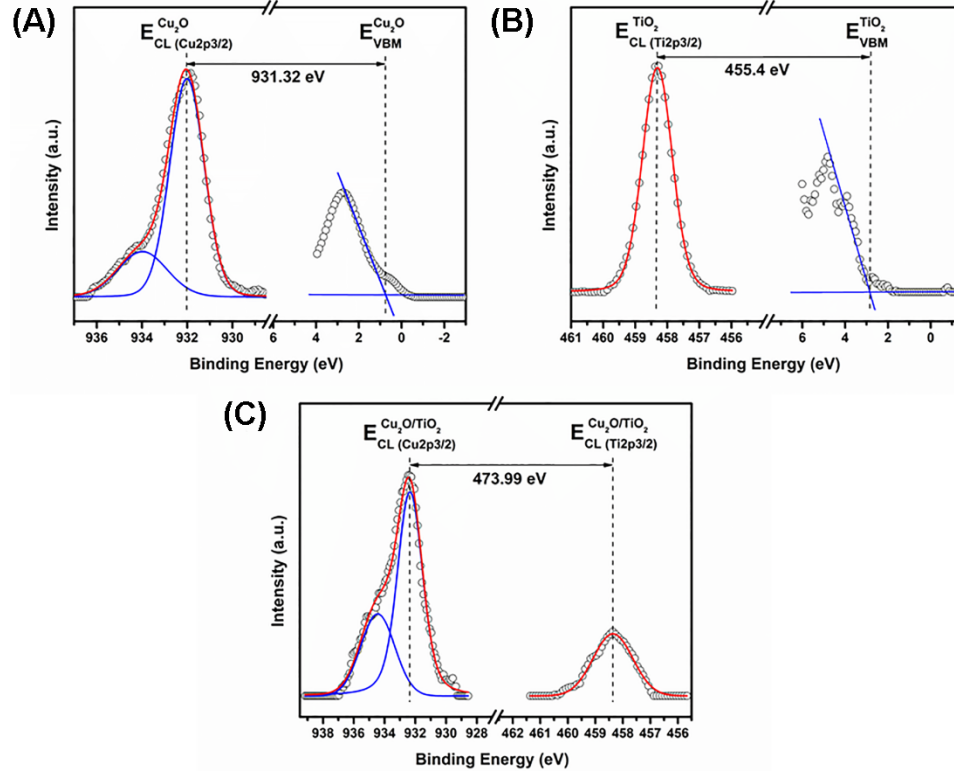
Figure S5.5 XPS core level and valence spectra from (A) Cu₂O octahedra, (B) pure TiO₂ and (C) Cu₂O/TiO₂ heterostructure. In the XPS spectrums, the experimental data points are shown with circles, and the fitted components obtained using a Voigt-type functions are shown in blue. The global fit is shown in red.

Construction of energy diagram

To construct the band diagram of pure materials (before contact) and the composite from UPS data, the position of the valence band maximum is obtained from Eq. (1):

$$E_{\text{VB}} = E_{\text{F}} - X \tag{1}$$

where E_F is the energy of the Fermi level and X is obtained from the extrapolation of the onsets in the UPS spectrum. The Fermi level needed in Eq. (1) is equivalent to the negative value for the work function ($E_F = -\Phi$), and can be calculated using Eq. (2):

$$\boldsymbol{\Phi} = hv - E_{SO} \tag{2}$$

In Eq. (2) hv = 10.2 eV represents the energy of the monochromatic ionizing light and E_{SO} is the secondary electron onset, which is obtained from the linear extrapolation of the UPS spectrum indicated above. Then, the conduction band minimum potential can be readily calculated applying Eq. (3):

$$E_{CB} = E_F + E_{BG} - X \tag{3}$$

where the bandgap energy E_{BG} is obtained by DRUV measurements. The results are summarized in the Table S5.

Table S5.1 Band energies of Cu_2O, TiO_2 and Cu_2O/TiO_2 composite calculated from the combination of results obtained by DRUV, UPS and XPS spectroscopies.

	E_{BG} (eV)	E_F (eV)	E_{VB} (eV)	E_{CB} (eV)	ΔE_{VBO} (eV)	ΔE_{CBO} (eV)
Cu_2O	2.034	0.26	0.76	-1.27	--	--
TiO_2	3.16	-0.38	2.59	-0.57	--	--
Cu_2O/TiO_2	2.01[#]	0.04	2.55[¥]	-1.39 [§]	1.93	0.81

* All quantities are referred to NHE.
[#] Apparent E_{BG} of Cu_2O in Cu_2O/TiO_2 composite.
[¥] The valence band maximum potential of TiO_2 in Cu_2O/TiO_2 composite.
[§] The conduction band minimum potential of Cu_2O in Cu_2O/TiO_2 composite.

Determination of CO evolution rates and analysis of products obtained during UV-visible irradiation of Cu_2O/TiO_2
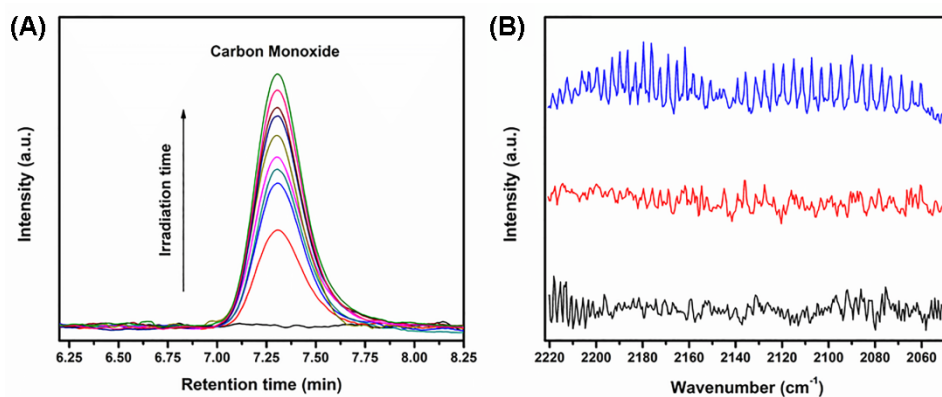
Figure S5.6 (A) Temporal evolution of CO peak monitored by GC obtained during the UV-visible irradiation of Cu_2O/TiO_2 and (B) Detection of CO formed in the gas phase by FTIR for 24 hours of irradiation of Cu_2O/TiO_2 in presence of (blue line) CO_2 and (red line) argon; and (black line) in presence of CO_2 and dark conditions for 24 hours.

Effect of UV-visible irradiation on photocatalysts evidenced by XPS
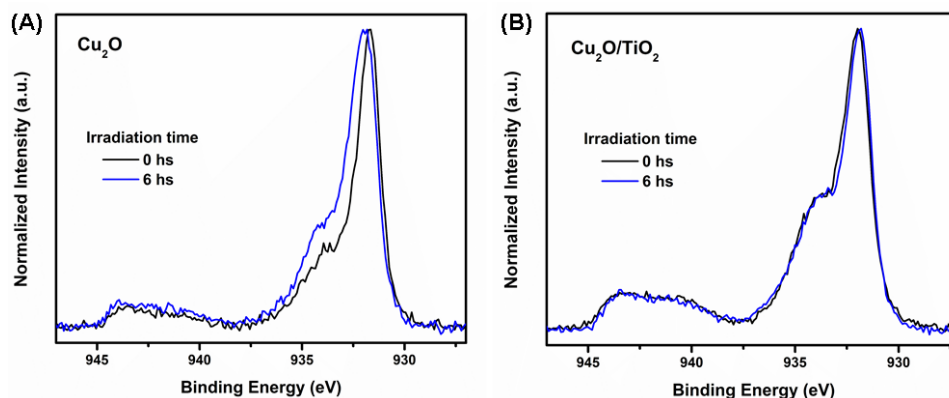
Figure S5.7 Normalized XPS spectra of the photocatalysts obtained for different irradiation times in the presence of CO_2 for (A) Cu_2O and (B) Cu_2O/TiO_2 composite.

Quantification of photogenerated HO radicals on the surface of UV-visible irradiated Cu_2O/TiO_2

The formation of hydroxyl radicals (HO$^•$) on the surface of irradiated Cu_2O/TiO_2 was quantified using the coumarin fluorescence method with a Lumina Fluorescence Spectrometer (Thermo Scientific) using excitation at λ_{exc} = 332 nm. While coumarin is a poorly fluorescent molecule, it is an excellent probe to quantify [HO$^•$] trapped in the produced 7-hydroxycoumarin:

7-Hydroxycoumarin has a characteristic fluorescent signal at λ_{em} = 456 nm,[173] which is proportional to the formed [HO$^•$].[174] The experimental procedure followed the same steps

140

of the photoreduction experiments, except that 30 mg of coumarin (Alfa Aesar, 98.0%) were deposited on top of the 30 mg of nanocomposite thin film for a 1:1 mass ratio.[168] Each data point corresponds to individual irradiation experiments at times of 0, 1, 2, and 3 h. Controls in the dark and with Cu_2O alone were also performed. Samples were extracted with 51 mL of water,[168] centrifuged at 4400 rpm for 5 min, and forced through a filter (Acrodisc 0.2 μm pore size; Pall Corp.) to quantify by standard addition the 7-hydroxycoumarin (Acros, 98.5%) produced.
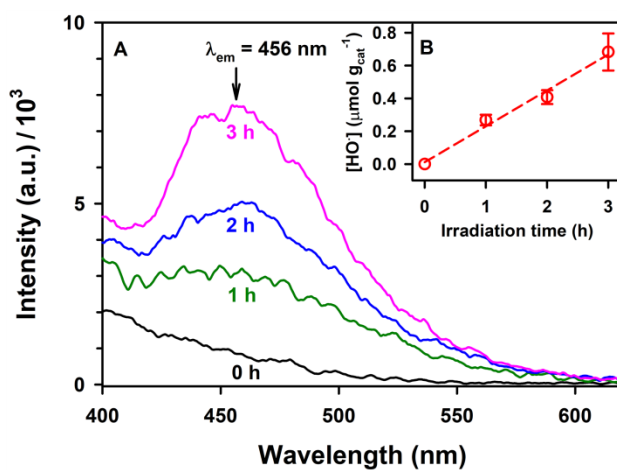
Figure S5.8 (A) Fluorescence spectra of extracted Cu_2O/TiO_2 during irradiation at $\lambda \geq$ 305 nm; (B) Production of HO$^\bullet$ from panel A.

Chapter 6. Conclusions

6.1 Conclusions

Heterogeneous photocatalysis has become an area of comprehensive study during the past several decades because of its great potential for solving the problems of environmental pollution and the world energy crisis by using renewable solar energy. In this work, ZnS has been demonstrated as a model semiconductor to study two photocatalytic reactions: 1) CO_2 reduction to $HCOO^-$ (Chapter 2); 2) fumarate reduction to succinate (Chapter 3) in the presence of Na_2S under irradiation.[18, 200] The lifetime of redox carriers on the surface of photoexcited ZnS has been characterized to remain active for 10 ms for electron transfer and 215 ms for the loss of oxidizing holes during the photoreduciton of CO_2 in the presence of Na_2S on ZnS.[200] The time scales of electron transfer and hole loss for the reduction of fumarate to succinate were 11 and 29 times faster than the corresponding values for CO_2 reduction under the identical conditions, indicating the structure of adsorbed reactive species regulated the lifetime of surface-active center of photoexcited ZnS.[18, 200] The photoreduction of CO_2 in aqueous suspension of ZnS with sodium sulfide hole scavenger directly consumed dissolved CO_2 as the reactive species.[200] In the case of fumaric acid, the monoprotic acid was the adsorbed species that accepts two electrons.[18]

The produced central metabolite succinate was utilized later during a synthetic study of zinc-rich sauconite clay (Chapter 4).[23] A Zn-rich clay sauconite has been successfully synthesized at 90 ºC and 1 atm on a short time scale with sodium succinate as the catalyst.[23] As a limiting reagent, succinate facilitated the incorporation of two aluminum atoms into the tetrahedral layers, which is essential for crystallization.[23] This work has

also illustrated the self-catalytic power of clay minerals and the mechanism of prebiotic central metabolites catalyzing their formation.[23]

In Chapter 5, the design of a Z-scheme heterostructured nanocomposite has provided an effective way to reduce CO_2 by avoiding the fast recombination of photogenerated electron-hole pairs.[201] Cu_2O/TiO_2 photocatalyst has been synthesized by a solvothermal method that deposited TiO_2 on the surface of octahedral Cu_2O.[201] The Cu_2O/TiO_2 nanocomposite exhibited a 2-times higher quantum efficiency of $CO(g)$ production than pure Cu_2O for photoreduction of CO_2 under irradiation at $\lambda \geq 305$ nm in the presence of water vapor.[201] The heterojunction structure facilitated the charge separation at the interface between p-type Cu_2O and n-type TiO_2 and greatly extended the lifetime of charge carriers.[201] A Z-scheme transfer mechanism has been proposed and further confirmed by the band alignment and the detection of $HO^\bullet$.[201] The study of reusability and XPS analysis has proven that TiO_2 prevents the photocorrosion of Cu_2O.[201]

6.2 Future Directions

An emerging area of research should be focused on developing novel materials with heterojunctions for photocatalysts with low cost and better stability. Hematite (α-Fe_2O_3) is an important nontoxic multifunctional material of low production cost and it has high thermal stability under ambient conditions.[202-204] Due to its unique properties, α-Fe_2O_3 can be used for catalytic purposes, gas-sensing, optical devices, lithium-ion batteries, and electromagnetic devices.[202-204] As a photocatalyst, α-Fe_2O_3 with a band gap $E_{BG} \sim 2.2$ eV,[205] has been used to degrade organic dyes such as Congo red in water treatment applications.[206] While laboratory synthesis typically generates α-Fe_2O_3 particles of

diameter 170 nm-2 μm,[207] commercially available amorphous superfine catalyst with a

diameter of 3 nm and high surface area should be an attractive material for catalytic

applications.[208-209] Nanocatalysts made of α-Fe_2O_3 have only been shown to catalyze the

oxidation of either CO or CH_4 to CO_2 in presence of O_2 at temperature above 100 °C.[210-211] Thus, the use of the materials to drive the photocatalytic reductions appears interesting

when combined with calcination to improve its crystallinity,[212] and phototcatalytic

activity. However, single semiconductor photocatalysts undergoes rapid recombination of

photogenerated electron-hole pairs, limiting significantly the energy-conversion

efficiency.[213-214]

Effective strategies for improving photocatalytic activity and visible light absorption

have been proposed by combining the semiconductor properties of two (i.e., *p* and *n*-

type) materials[213-214] or introducing structural modifications by doping with a metal.[215]

For example, *p-n* heterostructure Cu_2O/TiO_2 semiconductor has been proved to facilitate

the separation of the photogenerated charge carriers.[216] In addition, if calcination is

performed in the presence of K_2O, the alkali oxide should be deposited on the surface of

α-Fe_2O_3. Iron oxide catalyst doped with potassium displays higher catalytic activity for

ethylbenzene dehydrogenation because the alkali metals promotes electron transfer at the

solid-gas interface.[217] In the future study, a photocatalyst for CO_2 reduction can be made

by combining *p*-type α-Fe_2O_3 with *n*-type K_2O to provide enhanced 1) stability, 2)

absorption of visible light, and 3) photocatalytic activity relative to their pure

counterparts.[218-219] While *p-n* type heterojunctions have been used for photocatalytic

oxidations,[218-219] its application to drive photoreductions under Z-scheme systems deserve

to be explored further.[24, 220] It would be particularly interesting to vary the photon flux, the molar ratio of $CO_2 : H_2O$, and the amount of potassium present in the photocatalyst.

The study of self-catalytic power of clay minerals should be carried out in the future by adding sauconite as seed at 90 °C under ambient pressure for 20 h. This study should observe the nucleation stage during the formation of clay. Samples at 0, 1, 2, 6, and 20 h should be compared and characterized by TEM, EDS, XRD, and FTIR, and measurements of TSA and CEC. These promising experiments together with the work of heterogeneous photocatalysis will provide new directions and tremendous opportunities for developing a new generation of catalysts.

References

1. Quintero, J. C. C.; Xu, Y.-J., *Heterogeneous Photocatalysis: From Fundamentals to Green Applications*. 1st ed.; Springer: Berlin, 2015; p 416.

2. Jackson, R. B.; Canadell, J. G.; Le Quéré, C.; Andrew, R. M.; Korsbakken, J. I.; Peters, G. P.; Nakicenovic, N., Reaching peak emissions. *Nat. Clim. Change* **2016,** *6*, 7-10.

3. IPCC, *Climate Change 2007: Impacts, Adaption and Vulnerability. Contribution of Working Group II to the Fourth Assessment Report of the Intergovernmental Panel on Climate Change* **2007,** *Chapter 6* (Cambridge University Press: Cambridge).

4. Kisch, H., Semiconductor photocatalysis for chemoselective radical coupling reactions. *Acc. Chem. Res.* **2017,** *50*, 1002-1010.

5. Fan, W.; Zhang, Q.; Wang, Y., Semiconductor-based nanocomposites for photocatalytic H_2 production and CO_2 conversion. *Phys. Chem. Chem. Phys.* **2013,** *15*, 2632-2649.

6. Kamat, P. V., Manipulation of charge transfer across semiconductor interface. A criterion that cannot be ignored in photocatalyst design. *J. Phys. Chem. Lett.* **2012,** *3*, 663-672.

7. Li, W., Electrocatalytic reduction of CO_2 to small organic molecule fuels on metal catalysts. In *Advances in CO_2 Conversion and Utilization*, ACS Publications: 2010; pp 55-76.

8. Habisreutinger, S. N.; Schmidt- Mende, L.; Stolarczyk, J. K., Photocatalytic reduction of CO_2 on TiO_2 and other semiconductors. *Angew. Chem. Int. Ed.* **2013,** *52*, 7372-7408.

9. Zhou, R.; Guzman, M. I., CO_2 reduction under periodic illumination of ZnS. *J. Phys. Chem. C* **2014,** *118*, 11649-11656.

10. Ma-Hock, L.; Brill, S.; Wohlleben, W.; Farias, P.; Chaves, C.; Tenório, D.; Fontes, A.; Santos, B.; Landsiedel, R.; Strauss, V., Short term inhalation toxicity of a liquid aerosol of $CdS/Cd(OH)_2$ core shell quantum dots in male Wistar rats. *Toxicol. Lett.* **2012,** *208*, 115-124.

11. Zhang, X. V.; Ellery, S. P.; Friend, C. M.; Holland, H. D.; Michel, F.; Schoonen, M. A.; Martin, S. T., Photodriven reduction and oxidation reactions on colloidal semiconductor particles: Implications for prebiotic synthesis. *J. Photochem. Photobiol.* **2007,** *185*, 301-311.

12. Kuwabata, S.; Nishida, K.; Tsuda, R.; Inoue, H.; Yoneyama, H., Photochemical reduction of carbon dioxide to methanol using ZnS microcrystallite as a photocatalyst in the presence of methanol dehydrogenase. *J. Electrochem. Soc.* **1994,** *141*, 1498-1503.

13. Guzman, M. I., Abiotic photosynthesis: From prebiotic chemistry to metabolism. In *Origins of Life: The Primal Self-Organization*, 1 st ed.; Springer: Berlin, 2011; p 366.

14. Zhang, X. V.; Martin, S. T., Driving parts of Krebs cycle in reverse through mineral photochemistry. *J. Am. Chem. Soc.* **2006,** *128*, 16032-16033.

15. Guzman, M. I.; Martin, S. T., Oxaloacetate-to-malate conversion by mineral photoelectrochemistry: Implications for the viability of the reductive tricarboxylic

acid cycle in prebiotic chemistry. *International Journal of Astrobiology* **2008,** *7*, 271-278.

16. Guzman, M. I.; Martin, S. T., Prebiotic metabolism: production by mineral photoelectrochemistry of α-ketocarboxylic acids in the reductive tricarboxylic acid cycle. *Astrobiology* **2009,** *9*, 833-842.

17. Guzman, M. I.; Martin, S. T., Photo-production of lactate from glyoxylate: How minerals can facilitate energy storage in a prebiotic world. *Chem. Commun.* **2010,** *46*, 2265-2267.

18. Zhou, R.; Guzman, M. I., Photocatalytic reduction of fumarate to succinate on ZnS mineral surfaces. *J. Phys. Chem. C* **2016,** *120*, 7349-7357.

19. Essington, M. E., *Soil and Water Chemistry: An Integrative Approach*. 2nd ed.; CRC press: 2015.

20. Lehmann, J.; Kleber, M., The contentious nature of soil organic matter. *Nature* **2015,** *528*, 60-68.

21. Schumann, D.; Hartman, H.; Eberl, D. D.; Sears, S. K.; Hesse, R.; Vali, H., Formation of replicating saponite from a gel in the presence of oxalate: Implications for the formation of clay minerals in carbonaceous chondrites and the origin of life. *Astrobiology* **2012,** *12*, 549-561.

22. Hashizume, H., Role of clay minerals in chemical evolution and the origins of life. In *Clay Minerals in Nature-Their Characterization, Modification and Application*, 1st ed.; InTech: 2012; p 312.

23. Zhou, R.; Basu, K.; Hartman, H.; Matocha, C. J.; Sears, S. K.; Vali, H.; Guzman, M. I., Catalyzed synthesis of zinc clays by prebiotic central metabolites. *Sci. Rep.* **2017,** *7*, 533.

24. Wang, J.-C.; Zhang, L.; Fang, W.-X.; Ren, J.; Li, Y.-Y.; Yao, H.-C.; Wang, J.-S.; Li, Z.-J., Enhanced photoreduction CO_2 activity over direct Z-scheme α-Fe_2O_3/Cu_2O heterostructures under visible light irradiation. *ACS Appl. Mater. Interfaces* **2015,** *7*, 8631-8639.

25. Park, H.; Ou, H.-H.; Kang, U.; Choi, J.; Hoffmann, M. R., Photocatalytic conversion of carbon dioxide to methane on TiO_2/CdS in aqueous isopropanol solution. *Catal. Lett.* **2016,** *266*, 153-159.

26. Wang, Y.; Wang, Q.; Zhan, X.; Wang, F.; Safdar, M.; He, J., Visible light driven type II heterostructures and their enhanced photocatalysis properties: a review. *Nanoscale* **2013,** *5*, 8326-8339.

27. Zhou, P.; Yu, J.; Jaroniec, M., All- solid- state Z- scheme photocatalytic systems. *Adv. Mater.* **2014,** *26*, 4920-4935.

28. Yin, W.; Bai, L.; Zhu, Y.; Zhong, S.; Zhao, L.; Li, Z.; Bai, S., Embedding metal in the interface of a p-n heterojunction with a stack design for superior Z-scheme photocatalytic hydrogen evolution. *ACS Appl. Mater. Interfaces* **2016,** *8*, 23133-23142.

29. Katsumata, H.; Sakai, T.; Suzuki, T.; Kaneco, S., Highly efficient photocatalytic activity of g-C_3N_4/Ag_3PO_4 hybrid photocatalysts through Z-scheme photocatalytic mechanism under visible light. *Ind. Eng. Chem. Res.* **2014,** *53*, 8018-8025.

30. Handoko, A. D.; Tang, J., Controllable proton and CO_2 photoreduction over Cu_2O with various morphologies. *Int. J. Hydrogen Energy* **2013,** *38*, 13017-13022.

31. Zhang, Q.; Gao, T.; Andino, J. M.; Li, Y., Copper and iodine co-modified TiO_2 nanoparticles for improved activity of CO_2 photoreduction with water vapor. *Appl. Catal. B: Environ.* **2012,** *123*, 257-264.

32. Li, Y.; Wang, W.-N.; Zhan, Z.; Woo, M.-H.; Wu, C.-Y.; Biswas, P., Photocatalytic reduction of CO_2 with H_2O on mesoporous silica supported Cu/TiO_2 catalysts. *Appl. Catal. B: Environ.* **2010,** *100*, 386-392.

33. Chen, J.; Shen, S.; Guo, P.; Wang, M.; Wu, P.; Wang, X.; Guo, L., In-situ reduction synthesis of nano-sized Cu_2O particles modifying $g\text{-}C_3N_4$ for enhanced photocatalytic hydrogen production. *Appl. Catal. B: Environ.* **2014,** *152*, 335-341.

34. Aguirre, M. E.; Zhou, R.; Eugene, A. J.; Guzman, M. I.; Grela, M. A., Cu_2O/TiO_2 heterostructures for CO_2 reduction through a direct Z-scheme: protecting Cu_2O from photocorrosion. *Appl. Catal. B* **2017**, 217, 485-493.

35. Kumar, B.; Llorente, M.; Froehlich, J.; Dang, T.; Sathrum, A.; Kubiak, C. P., Photochemical and photoelectrochemical reduction of CO_2. *Annu. Rev. Phys. Chem.* **2012,** *63*, 541-569.

36. Costentin, C.; Robert, M.; Saveant, J.-M., Catalysis of the electrochemical reduction of carbon dioxide. *Chem. Soc. Rev.* **2013,** *42*, 2423-2436.

37. Boston, D. J.; Xu, C.; Armstrong, D. W.; MacDonnell, F. M., Photochemical reduction of carbon dioxide to methanol and formate in a homogeneous system with pyridinium catalysts. *J. Am. Chem. Soc.* **2013,** *135*, 16252-16255.

38. Guzman, M. I.; Martin, S. T., Prebiotic metabolism: Production by mineral photoelectrochemistry of α-ketocarboxylic acids in the reductive tricarboxylic acid cycle. *Astrobiology* **2009,** *9*, 833-842.

39. Artero, V.; Fontecave, M., Solar fuels generation and molecular systems: Is it homogeneous or heterogeneous catalysis? *Chem. Soc. Rev.* **2013,** *42*, 2338-2356.

40. de Richter, R. K.; Ming, T. Z.; Caillol, S., Fighting global warming by photocatalytic reduction of CO_2 using giant photocatalytic reactors. *Renew. Sust. Energ. Rev.* **2013,** *19*, 82-106.

41. Hoffmann, M. R.; Moss, J. A.; Baum, M. M., Artificial photosynthesis: Semiconductor photocatalytic fixation of CO_2 to afford higher organic compounds. *Dalton Trans.* **2011,** *40*, 5151-5158.

42. Eggins, B. R.; Robertson, P. K. J.; Murphy, E. P.; Woods, E.; Irvine, J. T. S., Factors affecting the photoelectrochemical fixation of carbon dioxide with semiconductor colloids. *J. Photoch. Photobio. A* **1998,** *118*, 31-40.

43. Nakaoka, Y.; Nosaka, Y., Electron spin resonance study of radicals produced by photoirradiation on quantized and bulk ZnS particles. *Langmuir* **1997,** *13*, 708-713.

44. Wenzhen, L., Electrocatalytic reduction of CO_2 to small organic molecule fuels on metal catalysts. In *Advances in CO_2 Conversion and Utilization*, American Chemical Society: 2010; Vol. 1056, pp 55-76.

45. Xu, Y.; Schoonen, M. A. A., The absolute energy positions of conduction and valence bands of selected semiconducting minerals. *Am. Miner.* **2000,** *85*, 543-556.

46. Kanemoto, M.; Shiragami, T.; Pac, C.; Yanagida, S., Semiconductor photocatalysis. Effective photoreduction of carbon dioxide catalyzed by ZnS quantum crystallites with low density of surface defects. *J. Phys. Chem.* **1992,** *96*, 3521-3526.

47. Zhang, X. V.; Ellery, S. P.; Friend, C. M.; Holland, H. D.; Michel, F. M.; Schoonen, M. A. A.; Martin, S. T., Photodriven reduction and oxidation reactions on colloidal

semiconductor particles: Implications for prebiotic syntheis. *J. Photoch. Photobio. A* **2007,** *185*, 301-311.

48. Feigl, C.; Russo, S. P.; Barnard, A. S., Safe, stable and effective nanotechnology: Phase mapping of ZnS nanoparticles. *J. Mater. Chem.* **2010,** *20*, 4971-4980.

49. Yanagida, S.; Ishimaru, Y.; Miyake, Y.; Shiragami, T.; Pac, C. J.; Hashimoto, K.; Sakata, T., Semiconductor photocatalysis .7. ZnS-catalyzed photoreduction of aldehydesand related derivatives - 2-electron-transfer reduction and relationship with spectroscopic properties. *J. Phys. Chem.* **1989,** *93*, 2576-2582.

50. Kirby, B., *Micro- and Nanoscale Fluid Mechanics: Transport in Microfluidic Devices*. Cambridge University Press: 2010; p 536.

51. Delgado, A. V.; Gonzalez-Caballero, F.; Hunter, R. J.; Koopal, L. K.; Lyklema, J., Measurement and interpretation of Electrokinetic phenomena. *J. Colloid Interf. Sci.* **2007,** *309*, 194-224.

52. Kisch, H., On the problem of comparing rates or apparent quantum yields in heterogeneous photocatalysis. *Angew. Chem. Int. Edit.* **2010,** *49*, 9588-9589.

53. Kuhn, H. J.; Braslavsky, S. E.; Schmidt, R., Chemical actinometry. *Pure Appl. Chem.* **2004,** *76*, 2105-2146.

54. Hatchard, C. G.; Parker, C. A., A new chemical actinometer. II Potasium ferrioxalate as a standard chemical actinometer. *Proc. R. Soc.* **1956,** *A235*, 518-536.

55. Wolf, H. P.; Bohning, J. J.; Schnieper, P. A.; Weiss, K., Apparatus for the measurement of quantum yields and rates of photochemical reactions. *Photochem. Photobiol.* **1967,** *6*, 321-329.

56. Serpone, N., Relative photonic efficiencies and quantum yields in heterogeneous photocatalysis. *J. Photoch. Photobio. A* **1997,** *104*, 1-12.

57. Nilsen, W. G., Raman spectrum of cubic ZnS. *Phys. Rev.* **1969,** *182*, 838-850.

58. Becker, W. G.; Bard, A. J., Photoluminescence and photoinduced oxygen adsorption of colloidal zinc sulfide dispersions. *J. Phys. Chem.* **1983,** *87*, 4888-4893.

59. House, J. E.; House, K. A., *Descriptive Inorganic Chemistry*. 2nd ed.; Elsevier: San Diego, 2010; p 592.

60. Katagiri, A.; Arai, H.; Takehara, Z., Mechanism of the electro- oxidation of sulfite catalyzed by copper ion. *J. Electrochem. Soc.* **1995,** *142*, 2899-2905.

61. Standard Reference Database 69: The NIST Chemistry WebBook. Mallard, W. G.; Linstrom, P. J., Eds. National Institute of Standards and Technology: http://webbook.nist.gov. Gaithersburg, MD, 2000; Vol. 2012.

62. Millero, F. J.; Graham, T. B.; Huang, F.; Bustos-Serrano, H.; Pierrot, D., Dissociation constants of carbonic acid in seawater as a function of salinity and temperature. *Mar. Chem.* **2006,** *100*, 80-94.

63. Atkins, P.; De Paula, J., *Elements of Physical Chemistry*. 6th ed.; W. H. Freeman: New York, 2013; p 630.

64. Brosillon, S.; Lhomme, L.; Vallet, C.; Bouzaza, A.; Wolbert, D., Gas phase photocatalysis and liquid phase photocatalysis: interdependence and influence of substrate concentration and photon Flow on degradation reaction kinetics. *Appl. Catal. B* **2008,** *78*, 232-241.

65. Emeline, A. V.; Ryabchuk, V.; Serpone, N., Factors affecting the efficiency of a photocatalyzed process in aqueous metal-oxide dispersions: Prospect of

distinguishing between two kinetic models. *J. Photoch. Photobio. A* **2000,** *133*, 89-97.

66. Ciucci, F.; de Falco, C.; Guzman, M. I.; Lee, S.; Honda, T., Chemisorption on semiconductors: The role of quantum corrections on the space charge regions in multiple dimensions. *Appl. Phys. Lett.* **2012,** *100*, 183106.

67. Rossetti, R.; Hull, R.; Gibson, J. M.; Brus, L. E., Excited electronic states and optical spectra of ZnS and CdS crystallites in the $\cong$ 15 to 50 Å size range: Evolution from molecular to bulk semiconducting properties. *J. Chem. Phys.* **1985,** *82*, 552-559.

68. Zhang, X. V.; Martin, S. T.; Friend, C. M.; Schoonen, M. A. A.; Holland, H. D., Mineral-assisted pathways in prebiotic synthesis: Photoelectrochemical reduction of carbon(+IV) by manganese sulfide. *J. Am. Chem. Soc.* **2004,** *126*, 11247-11253.

69. Henglein, A.; Gutiérrez, M., Photochemistry of colloidal metal sulfides. 5. Fluorescence and chemical reactions of ZnS and ZnS/CdS co-colloids. *Berich. Bunsen. Gesell.* **1983,** *87*, 852-858.

70. Mills, A.; Le Hunte, S., An overview of semiconductor photocatalysis. *J. Photoch. Photobio. A* **1997,** *108*, 1-35.

71. Cornu, C. J. G.; Colussi, A. J.; Hoffmann, M. R., Time scales and pH dependences of the redox processes determining the photocatalytic efficiency of TiO_2 nanoparticles from periodic illumination experiments in the stochastic regime. *J. Phys. Chem. B* **2003,** *107*, 3156-3160.

72. Bard, A. J.; Faulkner, L. R., *Electrochemical Methods: Fundamentals and Applications*. Wiley: 2000.

73. Zhao, J.; Holmes, M. A.; Osterloh, F. E., Quantum confinement controls photocatalysis: A free energy analysis for photocatalytic proton reduction at CdSe nanocrystals. *ACS Nano* **2013,** *7*, 4316-4325.

74. Mohamed, H. H.; Bahnemann, D. W., The role of electron transfer in photocatalysis: Fact and fictions. *Appl. Catal. B: Environ.* **2012,** *128*, 91-104.

75. Scott, D. W.; McCullough, J. P.; Kruse, F. H., Vibrational assignment and force constants of S_8 from a normal-coordinate treatment. *J. Mol. Spectrosc.* **1964,** *13*, 313-320.

76. Denzler, D.; Olschewski, M.; Sattler, K., Luminescence studies of localized gap states in colloidal ZnS nanocrystals. *J. Appl. Phys.* **1998,** *84*, 2841-2845.

77. Stumm, W.; Morgan, J. J., *Aquatic Chemistry*. 3rd ed.; John Wiley & Sons: New York, 1996; p 1022.

78. Board, A. J.; Parsons, R.; Jordan, J., *Standard Potentials in Aqueous Solution*. 1st ed.; CRC Press: New York, 1985; p 848.

79. Morel, F. M. M.; Hering, J. G., *Principles and Applications of Aquatic Chemistry*. John Wiley & Sons: New York, 1993; p 588.

80. Habisreutinger, S. N.; Schmidt-Mende, L.; Stolarczyk, J. K., Photocatalytic reduction of CO_2 on TiO_2 and other semiconductors. *Angew. Chem. Int. Edit.* **2013,** *52*, 7372-7408.

81. Hisatomi, T.; Kubota, J.; Domen, K., Recent advances in semiconductors for photocatalytic and photoelectrochemical water splitting. *Chem. Soc. Rev.* **2014,** *43*, 7520-7535.

82. Park, H.; Ou, H.-H.; Colussi, A. J.; Hoffmann, M. R., Artificial photosynthesis of C1–C3 hydrocarbons from water and CO_2 on titanate nanotubes decorated with nanoparticle elemental copper and CdS quantum dots. *J. Phys. Chem. A* **2015,** *119,* 4658-4666.

83. White, J. L.; Baruch, M. F.; Pander Iii, J. E.; Hu, Y.; Fortmeyer, I. C.; Park, J. E.; Zhang, T.; Liao, K.; Gu, J.; Yan, Y.; Shaw, T. W.; Abelev, E.; Bocarsly, A. B., Light-driven heterogeneous reduction of carbon dioxide: Photocatalysts and photoelectrodes. *Chem. Rev.* **2015,** *115,* 12888-12935.

84. Guzman, M. I., Abiotic Photosynthesis: From Prebiotic Chemistry to Metabolism. In *Origins of Life: The Primal Self-Organization*, Egel, R.; Lankenau, D.-H.; Mulkidjanian, A. Y., Eds. Springer Berlin Heidelberg: 2011; pp 85-105.

85. Guzman, M. I.; Martin, S. T., Oxaloacetate-to-malate conversion by mineral photoelectrochemistry: Implications for the viability of the reductive tricarboxylic acid cycle in prebiotic chemistry. *Int. J. Astrobiol.* **2008,** *7,* 271-278.

86. Zimmer, C., How and where did life on Earth arise? *Science* **2005,** *309,* 89-89.

87. Mulkidjanian, A. Y., On the origin of life in the Zinc world: 1. Photosynthesizing, porous edifices built of hydrothermally precipitated zinc sulfide as cradles of life on Earth. *Biol. Direct* **2009,** *4,* 1-39.

88. Mulkidjanian, A. Y.; Galperin, M. Y., On the origin of life in the Zinc world. 2. Validation of the hypothesis on the photosynthesizing zinc sulfide edifices as cradles of life on Earth. *Biol. Direct* **2009,** *4,* 1-37.

89. Hörner, G.; Johne, P.; Künneth, R.; Twardzik, G.; Roth, H.; Clark, T.; Kisch, H., Heterogeneous photocatalysis, part XIX. Semiconductor type A photocatalysis: role of substrate adsorption and the nature of photoreactive surface sites in zinc sulfide catalyzed C–C coupling reactions. *Chem.-Eur. J.* **1999,** *5,* 208-217.

90. Nelson, D. L.; Cox, M., *Lehninger Principles of Biochemistry*. 4rd ed.; W. H. Freeman: New York, 2004; p 1130.

91. Hatchard, C. G.; Parker, C. A., A new sensitive chemical actinometer. II. Potassium ferrioxalate as a standard chemical actinometer. *Proc. R. Soc. A* **1956,** *235,* 518-536.

92. Williams, R.; Labib, M. E., Zinc sulfide surface chemistry: An electrokinetic study. *J. Colloid Interf. Sci.* **1985,** *106,* 251-254.

93. Becker, W. G.; Bard, A. J., Photoluminescence and photoinduced oxygen adsorption of colloidal zinc sulfide dispersions. *J. Phys. Chem.* **1983,** *87,* 4888-4893.

94. Senger, B.; Voegel, J. C.; Schaaf, P., Irreversible adsorption of colloidal particles on solid substrates. *Colloids Surface A* **2000,** *165,* 255-285.

95. Aslam, M.; Mulla, I. S.; Vijayamohanan, K., Hydrophobic organization of monolayer-protected Au clusters on thiol-functionalized Au(111) surfaces. *Langmuir* **2001,** *17,* 7487-7493.

96. Ahmed, R.; Zhao, L.; Mozer, A. J.; Will, G.; Bell, J.; Wang, H., Enhanced electron lifetime of CdSe/CdS quantum dot (QD) sensitized solar cells using ZnSe core–shell structure with efficient regeneration of quantum dots. *J. Phys. Chem. C* **2015,** *119,* 2297-2307.

97. Mohamed, H. H.; Bahnemann, D. W., The role of electron transfer in photocatalysis: Fact and fictions. *Appl. Catal. B-Environ.* **2012,** *128,* 91-104.

98. Emeline, A. V.; Ryabchuk, V. K.; Serpone, N., Dogmas and Misconceptions in Heterogeneous Photocatalysis. Some Enlightened Reflections. *J. Phys. Chem. B* **2005,** *109*, 18515-18521.

99. Kisch, H., *Semiconductor Photocatalysis: Principles and Applications*. John Wiley & Sons: Weinheim, Germany, 2014.

100. Wang, M.; Zhang, Q.; Hao, W.; Sun, Z., Surface stoichiometry of zinc sulfide and its effect on the adsorption behaviors of xanthate. *Chem. Cent. J.* **2011,** *5*, 73.

101. Sun, Z.; Forsling, W.; Rönngren, L.; Sjöberg, S., Surface reactions in aqueous metal sulfide systems. 1. Fundamental surface reactions of hydrous PbS and ZnS. *Int. J. Miner. Process.* **1991,** *33*, 83-93.

102. Rönngren, L.; Sjöberg, S.; Sun, Z.; Forsling, W.; Schindler, P., Surface reactions in aqueous metal sulfide systems: 2. Ion exchange and acid/base reactions at the $ZnSH_2O$ interface. *J. Colloid Interface Sci.* **1991,** *145*, 396.

103. Pearson, R. G. j., Hard and soft acids and bases, HSAB, part 1: Fundamental principles. *J. Chem. Educ.* **1968,** *45*, 581.

104. Brown, C. J., The crystal structure of fumaric acid. *Acta Crystallogr.* **1966,** *21*, 1-5.

105. Bednowitz, A. L.; Post, B., Direct determination of the crystal structure of β-fumaric acid. *Acta Crystallogr.* **1966,** *21*, 566-571.

106. Miehlich, B.; Savin, A.; Stoll, H.; Preuss, H., Results obtained with the correlation energy density functionals of Becke and Lee, Yang and Parr. *Chem. Phys. Lett.* **1989,** *157*, 200-206.

107. Lee, C.; Yang, W.; Parr, R. G., Development of the Colle-Salvetti correlation-energy formula into a functional of the electron density. *Phys. Rev. B* **1988,** *37*, 785.

108. McLean, A. D.; Chandler, G. S., Contracted Gaussian basis sets for molecular calculations. I. Second row atoms, Z = 11−18. *J. Chem. Phys.* **1980,** *72*, 5639-5648.

109. Krishnan, R. B. J. S.; Binkley, J. S.; Seeger, R.; Pople, J. A., Self- consistent molecular orbital methods. XX. A basis set for correlated wave functions. *J. Chem. Phys.* **1980,** *72*, 650-654.

110. Zimmer, C., How and where did life on Earth arise? *Science* **2005,** *309*, 89-89.

111. Hartman, H., Speculations on origin and evolution of metabolism. *J. Mol. Evol.* **1975,** *4*, 359-370.

112. Wächtershäuser, G., Evolution of the first metabolic cycles. *Proc. Natl. Acad. Sci. U.S.A.* **1990,** *87*, 200-204.

113. Morowitz, H. J.; Kostelnik, J. D.; Yang, J.; Cody, G. D., The origin of intermediary metabolism. *Proc. Natl. Acad. Sci. U.S.A.* **2000,** *97*, 7704-7708.

114. Smith, E.; Morowitz, H. J., Universality in intermediary metabolism. *Proc. Natl. Acad. Sci. U.S.A.* **2004,** *101*, 13168-13173.

115. Zhou, R.; Guzman, M. I., Photocatalytic reduction of fumarate to succinate on ZnS mineral surfaces. *J. Phys. Chem. C* **2016,** *120*, 7349–7357.

116. Essington, M. E., *Soil and Water Chemistry: An Integrative Approach*. CRC press: 2015; p 656.

117. Ruiz-Mirazo, K.; Briones, C.; de la Escosura, A., Prebiotic systems chemistry: New perspectives for the origins of life. *Chem. Rev.* **2014,** *114*, 285-366.

118. Cairns-Smith, A. G.; Hartman, H., Clay Minerals and the Origin of Life. Cambridge University Press: Cambridge, 1986; p 193.

119. Vogels, R. J. M. J.; Kloprogge, J. T.; Geus, J. W., Synthesis and characterization of saponite clays. *Am. Mineral.* **2005,** *90*, 931-944.

120. Pillar, E. A.; Camm, R. C.; Guzman, M. I., Catechol oxidation by ozone and hydroxyl radicals at the air–water interface. *Environ. Sci. Technol.* **2014,** *48*, 14352-14360.

121. Pillar, E. A.; Zhou, R.; Guzman, M. I., Heterogeneous oxidation of catechol. *J. Phys. Chem. A* **2015,** *119*, 10349-10359.

122. Eugene, A. J.; Xia, S.-S.; Guzman, M. I., Aqueous photochemistry of glyoxylic acid. *J. Phys. Chem. A* **2016,** *120*, 3817-3826.

123. Siffert, B., The role of organic complexing agents. In *Clay Minerals and the Origin of Life*, Cairns-Smith, A. G.; Hartman, H., Eds. Cambridge University Press: Cambridge, 1986; pp 75-78.

124. Vogels, R. J. M. J.; Kloprogge, J. T.; Geus, J. W., Catalytic activity of synthetic saponite clays: effects of tetrahedral and octahedral composition. *J. Catal.* **2005,** *231*, 443-452.

125. Higashi, S.; Miki, K.; Komarneni, S., Hydrothermal synthesis of Zn-smectites. *Clays Clay Miner.* **2002,** *50*, 299-305.

126. Pavia, D.; Lampman, G.; Kriz, G.; Vyvyan, J., *Introduction to spectroscopy*. 4th ed.; Brooks/Cole: Belmont, CA, 2008; p 752.

127. Drever, J. I., The preparation of oriented clay mineral specimens for X-ray diffraction analysis by filter-membrane peel technique. *Am. Mineral.* **1973,** *58*, 553-554.

128. Heilman, M.; Carter, D.; Gonzalez, C., The ethylene glycol monoethyl ether (EGME) technique for determining soil-surface area. *Soil Sci.* **1965,** *100*, 409-413.

129. Hendershot, W. H.; Duquette, M., A simple barium chloride method for determining cation exchange capacity and exchangeable cations. *Soil Sci. Soc. Am. J.* **1986,** *50*, 605-608.

130. Dixon, J. B.; Schulze, D. G., *Soil Mineralogy with Environmental Applications*. 1st ed.; Soil Sci. Soc. Am.: 2002; p 866.

131. Kremer, J. R.; Mastronarde, D. N.; McIntosh, J. R., Computer visualization of three-dimensional image data using IMOD. *J. Struct. Biol.* **1996,** *116*, 71-76.

132. Pettersen, E. F.; Goddard, T. D.; Huang, C. C.; Couch, G. S.; Greenblatt, D. M.; Meng, E. C.; Ferrin, T. E., UCSF Chimera—A visualization system for exploratory research and analysis. *J. Comput. Chem.* **2004,** *25*, 1605-1612.

133. Faust, G. T., Thermal analysis and X-ray studies of sauconite and some zinc minerals of the same paragenetic association. *Am. Mineral.* **1951,** *36*, 795-822.

134. Shao, H.; Pinnavaia, T. J., Synthesis and properties of nanoparticle forms saponite clay, cancrinite zeolite and phase mixtures thereof. *Microporous Mesoporous Mater.* **2010,** *133*, 10-17.

135. Yokoyama, S.; Tamura, K.; Hatta, T.; Nemoto, S.; Watanabe, Y.; Yamada, H., Synthesis and characterization of Zn-substituted saponite (sauconite). *Clay Sci.* **2006,** *13*, 75-80.

136. Nakakuki, T.; Fujimura, K.; Aisawa, S.; HiraharaI, H., Synthesis and physicochemical properties of Zn-hectorite. *Clay Sci.* **2004,** *12*, 285-291.

137. Wilkins, R.; Ito, J., Infrared spectra of some synthetic talcs. *Am. Mineral.* **1967,** *52*, 1649-1661.

138. Madejová, J.; Komadel, P., Baseline studies of the clay minerals society source clays: Infrared methods. *Clays Clay Miner.* **2001,** *49*, 410-432.

139. Buhl, J.-C.; Stief, F.; Fechtelkord, M.; Gesing, T. M.; Taphorn, U.; Taake, C., Synthesis, X-ray diffraction and MAS NMR characteristics of nitrate cancrinite $Na_{7.6}[AlSiO_4]_6(NO_3)_{1.6}(H_2O)_2$. *J. Alloys Comp.* **2000,** *305*, 93-102.

140. Madejová, J.; Sekeráková, l.; Bizovská, V.; Slaný, M.; L.;, a., Near-infrared spectroscopy as an effective tool for monitoring the conformation of alkylammonium surfactants in montmorillonite interlayers. *Vib. Spectrosc.* **2016,** *84*, 44-52.

141. Li, Y.; Cai, J.; Song, M.; Ji, J.; Bao, Y., Influence of organic matter on smectite illitization: A comparison between red and dark mudstones from the Dongying Depression, China. *Am. Mineral.* **2016,** *101*, 134-145.

142. Dixon, J. B.; Weed, S. B.; Dinauer, R. C., *Minerals in Soil Environments*. 2nd ed.; Soil Sci. Soc. Am.: 1989.

143. Farmer, V. C.; Fraser, A. R.; Tait, J. M., Characterization of the chemical structures of natural and synthetic aluminosilicate gels and sols by infrared spectroscopy. *Geochim. Cosmochim. Ac.* **1979,** *43*, 1417-1420.

144. Vali, H.; Bachmann, L., Ultrastructure and flow behavior of colloidal smectite dispersions. *J. Colloid Interface Sci.* **1988,** *126*, 278-291.

145. Tenorio Arvide, M. G.; Mulder, I.; Barrientos Velazquez, A. L.; Dixon, J. B., Smectite clay adsorption of Aflatoxin vs. octahedral composition as indicated by FTIR. *Clays Clay Miner.* **2008,** *56*, 571-578.

146. *CRC Handbook of Chemistry and Physics*. 93rd ed.; CRC Press/Taylor and Francis: Boca Raton, Fl., **2013**; p 2664.

147. Standard Reference Database 69: The NIST Chemistry WebBook. Mallard, W. G.; Linstrom, P. J., Eds. National Institute of Standards and Technology: http://webbook.nist.gov. Gaithersburg, MD, 2000; Vol. 2012.

148. Vogels, R. J. M. J.; Kloprogge, J. T.; Geus, J. W.; Beers, A. W. F., Synthesis and characterization of saponite clays: Part 2. Thermal stability. *Am. Mineral.* **2005,** *90* (5-6), 945-953.

149. Klug, H. P.; Alexander, L. E., *X-ray diffraction procedures*. 2nd ed.; Wiley-Interscience: 1954; p 966.

150. Izumi, Y., Recent advances in the photocatalytic conversion of carbon dioxide to fuels with water and/or hydrogen using solar energy and beyond. *Coord. Chem. Rev.* **2013,** *257*, 171-186.

151. Chang, X.; Wang, T.; Gong, J., CO_2 photo-reduction: Insights into CO_2 activation and reaction on surfaces of photocatalysts. *Energy Environ. Sci.* **2016,** *9*, 2177-2196.

152. Sato, S.; Arai, T.; Morikawa, T., Toward solar-driven photocatalytic CO_2 reduction using water as an electron donor. *Inorg. Chem.* **2015,** *54*, 5105-5113.

153. Sahara, G.; Ishitani, O., Efficient photocatalysts for CO_2 reduction. *Inorg. Chem.* **2015,** *54*, 5096-5104.

154. Benson, E. E.; Kubiak, C. P.; Sathrum, A. J.; Smieja, J. M., Electrocatalytic and homogeneous approaches to conversion of CO_2 to liquid fuels. *Chem. Soc. Rev.* **2009,** *38*, 89-99.

155. Schneider, J.; Jia, H.; Muckerman, J. T.; Fujita, E., Thermodynamics and kinetics of CO_2, CO, and H^+ binding to the metal centre of CO_2 reduction catalysts. *Chem. Soc. Rev.* **2012,** *41*, 2036-2051.

156. Agarwal, J.; Fujita, E.; Schaefer III, H. F.; Muckerman, J. T., Mechanisms for CO production from CO_2 using reduced rhenium tricarbonyl catalysts. *J. Am. Chem. Soc.* **2012,** *134*, 5180-5186.

157. Morris, A. J.; Meyer, G. J.; Fujita, E., Molecular approaches to the photocatalytic reduction of carbon dioxide for solar fuels. *Acc. Chem. Res.* **2009,** *42*, 1983-1994.

158. Takeda, H.; Koike, K.; Inoue, H.; Ishitani, O., Development of an efficient photocatalytic system for CO_2 reduction using rhenium(I) complexes based on mechanistic studies. *J. Am. Chem. Soc.* **2008,** *130*, 2023-2031.

159. Gholamkhass, B.; Mametsuka, H.; Koike, K.; Tanabe, T.; Furue, M.; Ishitani, O., Architecture of supramolecular metal complexes for photocatalytic CO_2 reduction: Ruthenium−rhenium Bi-and tetranuclear complexes. *Inorg. Chem.* **2005,** *44*, 2326-2336.

160. Dhakshinamoorthy, A.; Navalon, S.; Corma, A.; Garcia, H., Photocatalytic CO_2 reduction by TiO_2 and related titanium containing solids. *Energy Environ. Sci.* **2012,** *5*, 9217-9233.

161. Wardman, P., Reduction potentials of one- electron couples involving free radicals in aqueous solution. *J. Phys. Chem. Ref. Data* **1989,** *18*, 1637-1755.

162. Chen, S.; Cao, T.; Gao, Y.; Li, D.; Xiong, F.; Huang, W., Probing surface structures of CeO_2, TiO_2, and Cu_2O nanocrystals with CO and CO_2 chemisorption. *J. Phys. Chem. C* **2016,** *120*, 21472-21485.

163. Levy, I. K.; Brusa, M. A.; Aguirre, M. E.; Custo, G.; San Román, E.; Litter, M. I.; Grela, M. A., Exploiting electron storage in TiO_2 nanoparticles for dark reduction of As(v) by accumulated electrons. *Phys. Chem. Chem. Phys.* **2013,** *15*, 10335-10338.

164. de Jongh, P. E.; Vanmaekelbergh, D.; Kelly, J. J., Cu_2O: A catalyst for the photochemical decomposition of water? *Chem. Commun.* **1999**, 1069-1070.

165. Paracchino, A.; Laporte, V.; Sivula, K.; Grätzel, M.; Thimsen, E., Highly active oxide photocathode for photoelectrochemical water reduction. *Nat. Mater.* **2011,** *10*, 456-461.

166. Xu, H.; Ouyang, S.; Liu, L.; Wang, D.; Kako, T.; Ye, J., Porous-structured Cu_2O/TiO_2 nanojunction material toward efficient CO_2 photoreduction. *Nanotechnology* **2014,** *25*, 165402.

167. Huang, L.; Peng, F.; Wang, H.; Yu, H.; Li, Z., Preparation and characterization of Cu_2O/TiO_2 nano–nano heterostructure photocatalysts. *Catal. Commun.* **2009,** *10*, 1839-1843.

168. Wang, J.-C.; Zhang, L.; Fang, W.-X.; Ren, J.; Li, Y.-Y.; Yao, H.-C.; Wang, J.-S.; Li, Z.-J., Enhanced photoreduction CO_2 activity over direct Z-scheme α-Fe_2O_3/Cu_2O heterostructures under visible light irradiation. *ACS Appl. Mater. Interfaces* **2015,** *7*, 8631-8639.

169. Sekizawa, K.; Maeda, K.; Domen, K.; Koike, K.; Ishitani, O., Artificial Z-scheme constructed with a supramolecular metal complex and semiconductor for the photocatalytic reduction of CO_2. *J. Am. Chem. Soc.* **2013,** *135*, 4596-4599.

170. Maeda, K., Z-scheme water splitting using two different semiconductor photocatalysts. *ACS Catal.* **2013,** *3*, 1486-1503.

171. Zhang, D.-F.; Zhang, H.; Guo, L.; Zheng, K.; Han, X.-D.; Zhang, Z., Delicate control of crystallographic facet-oriented Cu_2O nanocrystals and the correlated adsorption ability. *J. Mater. Chem.* **2009,** *19*, 5220-5225.

172. Liu, L.; Yang, W.; Li, Q.; Gao, S.; Shang, J. K., Synthesis of Cu_2O nanospheres decorated with TiO_2 nanoislands, their enhanced photoactivity and stability under visible light illumination, and their post-illumination catalytic memory. *ACS Appl. Mater. Interfaces* **2014,** *6*, 5629-5639.

173. Xiang, Q.; Yu, J.; Wong, P. K., Quantitative characterization of hydroxyl radicals produced by various photocatalysts. *J. Colloid Interface Sci.* **2011,** *357*, 163-167.

174. Louit, G.; Foley, S.; Cabillic, J.; Coffigny, H.; Taran, F.; Valleix, A.; Renault, J. P.; Pin, S., The reaction of coumarin with the OH radical revisited: hydroxylation product analysis determined by fluorescence and chromatography. *Radiat. Phys. Chem.* **2005,** *72*, 119-124.

175. Liu, L.; Yang, W.; Sun, W.; Li, Q.; Shang, J. K., Creation of $Cu_2O@TiO_2$ composite photocatalysts with p–n heterojunctions formed on exposed Cu_2O facets, their energy band alignment study, and their enhanced photocatalytic activity under illumination with visible light. *ACS Appl. Mater. Interfaces* **2015,** *7*, 1465-1476.

176. Pan, L.; Zou, J.-J.; Zhang, T.; Wang, S.; Li, Z.; Wang, L.; Zhang, X., Cu_2O film via hydrothermal redox approach: morphology and photocatalytic performance. *J. Phys. Chem. C* **2013,** *118*, 16335-16343.

177. Xu, Y.; Wang, H.; Yu, Y.; Tian, L.; Zhao, W.; Zhang, B., Cu_2O nanocrystals: surfactant-free room-temperature morphology-modulated synthesis and shape-dependent heterogeneous organic catalytic activities. *J. Phys. Chem. C* **2011,** *115*, 15288-15296.

178. Yuan, G. Z.; Hsia, C. F.; Lin, Z. W.; Chiang, C.; Chiang, Y. W.; Huang, M. H., Highly facet- dependent photocatalytic properties of Cu_2O crystals established through the formation of Au- decorated Cu_2O heterostructures. *Chem. Eur. J.* **2016,** *22*, 12548-12556.

179. Li, K.; An, X.; Park, K. H.; Khraisheh, M.; Tang, J., A critical review of CO_2 photoconversion: Catalysts and reactors. *Catal. Today* **2014,** *224*, 3-12.

180. Poulston, S.; Parlett, P.; Stone, P.; Bowker, M., Surface oxidation and reduction of CuO and Cu_2O studied using XPS and XAES. *Surf. Interface Anal.* **1996,** *24*, 811-820.

181. Platzman, I.; Brener, R.; Haick, H.; Tannenbaum, R., Oxidation of polycrystalline copper thin films at ambient conditions. *J. Phys. Chem. C* **2008,** *112*, 1101-1108.

182. Logar, M.; Bračko, I.; Potočnik, A.; Jančar, B. t., Cu and CuO/titanate nanobelt based network assemblies for enhanced visible light photocatalysis. *Langmuir* **2014,** *30*, 4852-4862.

183. Erdem, B.; Hunsicker, R. A.; Simmons, G. W.; Sudol, E. D.; Dimonie, V. L.; El-Aasser, M. S., XPS and FTIR surface characterization of TiO_2 particles used in polymer encapsulation. *Langmuir* **2001,** *17*, 2664-2669.

184. Braun, A.; Aksoy Akgul, F.; Chen, Q.; Erat, S.; Huang, T.-W.; Jabeen, N.; Liu, Z.; Mun, B. S.; Mao, S. S.; Zhang, X., Observation of substrate orientation-dependent

oxygen defect Filling in thin $WO_3-\delta$/TiO_2 pulsed laser-deposited films with in situ XPS at high oxygen pressure and temperature. *Chem. Mater.* **2012,** *24*, 3473-3480.

185. Li, Z.; Cong, S.; Xu, Y., Brookite vs anatase TiO_2 in the photocatalytic activity for organic degradation in water. *ACS Catal.* **2014,** *4*, 3273-3280.

186. Buha, J., Solar absorption and microstructure of C-doped and H-co-doped TiO_2 thin films. *J. Phys. D: Appl. Phys.* **2012,** *45*, 385305.

187. Yin, M.; Wu, C.-K.; Lou, Y.; Burda, C.; Koberstein, J. T.; Zhu, Y.; O'Brien, S., Copper oxide nanocrystals. *J. Am. Chem. Soc.* **2005,** *127*, 9506-9511.

188. Lu, W.; Gao, S.; Wang, J., One-pot synthesis of Ag/ZnO self-assembled 3D hollow microspheres with enhanced photocatalytic performance. *J. Phys. Chem. C* **2008,** *112*, 16792-18600.

189. Kraut, E.; Grant, R.; Waldrop, J.; Kowalczyk, S., Precise determination of the valence-band edge in X-ray photoemission spectra: Application to measurement of semiconductor interface potentials. *Phys. Rev. Lett.* **1980,** *44*, 1620.

190. Sharma, B. L.; Purohit, R. K., *Semiconductor Heterojunctions*. 1st ed.; Pergamon Press: Oxford-New York-Toronto-Sydney, 2015; Vol. 5, p 216.

191. Bera, A.; Dey, S.; Pal, A. J., Band mapping across a pn-junction in a nanorod by scanning tunneling microscopy. *Nano Lett.* **2014,** *14*, 2000-2005.

192. Siol, S.; Hellmann, J. C.; Tilley, S. D.; Graetzel, M.; Morasch, J.; Deuermeier, J.; Jaegermann, W.; Klein, A., Band alignment engineering at Cu_2O/ZnO heterointerfaces. *ACS Appl. Mater. Interfaces* **2016,** *8*, 21824-21831.

193. Pastor, E.; Pesci, F. M.; Reynal, A.; Handoko, A. D.; Guo, M.; An, X.; Cowan, A. J.; Klug, D. R.; Durrant, J. R.; Tang, J., Interfacial charge separation in Cu_2O/RuO_x as a visible light driven CO_2 reduction catalyst. *Phys. Chem. Chem. Phys.* **2014,** *16*, 5922-5926.

194. QingáLu, G., Enhanced photocatalytic hydrogen evolution by prolonging the lifetime of carriers in ZnO/CdS heterostructures. *Chem. Commun.* **2009**, 3452-3454.

195. Berger, T.; Sterrer, M.; Diwald, O.; Knözinger, E.; Panayotov, D.; Thompson, T. L.; Yates, J. T., Light-induced charge separation in anatase TiO_2 particles. *J. Phys. Chem. B* **2005,** *109*, 6061-6068.

196. Freund, H.-J.; Roberts, M. W., Surface chemistry of carbon dioxide. *Surf. Sci. Rep.* **1996,** *25*, 225-273.

197. Indrakanti, V. P.; Kubicki, J. D.; Schobert, H. H., Photoinduced activation of CO_2 on Ti-based heterogeneous catalysts: Current state, chemical physics-based insights and outlook. *Energy Environ. Sci.* **2009,** *2*, 745-758.

198. Tran, P. D.; Wong, L. H.; Barber, J.; Loo, J. S., Recent advances in hybrid photocatalysts for solar fuel production. *Energy Environ. Sci.* **2012,** *5*, 5902-5918.

199. Teo, J. J.; Chang, Y.; Zeng, H. C., Fabrications of hollow nanocubes of Cu_2O and Cu via reductive self-assembly of CuO nanocrystals. *Langmuir* **2006,** *22*, 7369-7377.

200. Zhou, R.; Guzman, M. I., CO_2 reduction under periodic illumination of ZnS. *J. Phys. Chem. C* **2014,** *118*, 11649-11656.

201. Aguirre, M. E.; Zhou, R.; Eugene, A. J.; Guzman, M. I.; Grela, M. A., Cu_2O/TiO_2 heterostructures for CO_2 reduction through a direct Z-scheme: Protecting Cu_2O from photocorrosion. *Appl. Catal. B* **2017**, 217, 485-493.

202. Sun, L.; Han, X.; Liu, K.; Yin, S.; Chen, Q.; Kuang, Q.; Han, X.; Xie, Z.; Wang, C., Template-free construction of hollow α-Fe$_2$O$_3$ hexagonal nanocolumn particles with an exposed special surface for advanced gas sensing properties. *Nanoscale* **2015,** *7*, 9416-9420.

203. Li, D.; Zhang, Y.; Xu, J.; Jin, H.; Jin, D.; Hong, B.; Peng, X.; Wang, P.; Ge, H.; Wang, X., Nanocasting synthesis and gas-sensing behavior of hematite nanowires. *Physica E* **2016,** *84*, 395-400.

204. Zhang, X.; Niu, Y.; Li, Y.; Li, Y.; Zhao, J., Preparation and thermal stability of the spindle α-Fe$_2$O$_3$@SiO$_2$ core–shell nanoparticles. *J. Solid State Chem* **2014,** *211*, 69-74.

205. Mishra, M.; Chun, D.-M., α-Fe$_2$O$_3$ as a photocatalytic material: a review. *Appl Catal A.* **2015,** *498*, 126-141.

206. Sundaramurthy, J.; Kumar, P. S.; Kalaivani, M.; Thavasi, V.; Mhaisalkar, S. G.; Ramakrishna, S., Superior photocatalytic behaviour of novel 1D nanobraid and nanoporous α-Fe$_2$O$_3$ structures. *RSC Adv.* **2012,** *2*, 8201-8208.

207. Yang, S.; Xu, Y.; Sun, Y.; Zhang, G.; Gao, D., Size-controlled synthesis, magnetic property, and photocatalytic property of uniform α-Fe$_2$O$_3$ nanoparticles via a facile additive-free hydrothermal route. *CrystEngComm* **2012,** *14*, 7915-7921.

208. Li, P.; Miser, D. E.; Rabiei, S.; Yadav, R. T.; Hajaligol, M. R., The removal of carbon monoxide by iron oxide nanoparticles. *Appl Catal B.* **2003,** *43*, 151-162.

209. Townsend, T. K.; Sabio, E. M.; Browning, N. D.; Osterloh, F. E., Photocatalytic water oxidation with suspended alpha-Fe$_2$O$_3$ particles-effects of nanoscaling. *Energy Environ Sci* **2011,** *4*, 4270-4275.

210. Walker, J. S.; Straguzzi, G. I.; Manogue, W. H.; Schuit, G. C. A., Carbon monoxide and propene oxidation by iron oxides for auto-emission control. *J. Catal.* **1988,** *110*, 298-309.

211. Li, P.; Miser, D. E.; Rabiei, S.; Yadav, R. T.; Hajaligol, M. R., The removal of carbon monoxide by iron oxide nanoparticles. *Appl Catal B* **2003,** *43*, 151-162.

212. Dang, S. N.; Lu, S. X.; Xu, W. G.; Sa, J., Dark-degradation of reactive brilliant blue X-BR in aqueous solution using α-Fe$_2$O$_3$. *J. Non-Cryst. Solids* **2008,** *354*, 5018-5021.

213. Wang, M.; Han, J.; Hu, Y.; Guo, R.; Yin, Y., Carbon-incorporated NiO/TiO$_2$ mesoporous shells with *p-n* heterojunctions for efficient visible light photocatalysis. *ACS Appl. Mater. Interfaces* **2016,** *8*, 29511-29521.

214. Yin, W.; Bai, L.; Zhu, Y.; Zhong, S.; Zhao, L.; Li, Z.; Bai, S., Embedding metal in the interface of a *p-n* heterojunction with a stack design for Superior Z-Scheme photocatalytic hydrogen evolution. *ACS Appl. Mater. Interfaces* **2016,** *8*, 23133-23142.

215. Lu, M.; Pichat, P., *Photocatalysis and water purification: from fundamentals to recent applications*. 1 st ed.; John Wiley & Sons: New Jersey, 2013; p 438.

216. Yang, L.; Luo, S.; Li, Y.; Xiao, Y.; Kang, Q.; Cai, Q., High efficient photocatalytic degradation of p-nitrophenol on a unique Cu$_2$O/TiO$_2$ pn heterojunction network catalyst. *Environ. Sci. Technol.* **2010,** *44*, 7641-7646.

217. Hirano, T., Roles of potassium in potassium-promoted iron oxide catalyst for dehydrogenation of ethylbenzene. *Appl. Catal.* **1986,** *26*, 65-79.

218. Liang, N.; Wang, M.; Jin, L.; Huang, S.; Chen, W.; Xu, M.; He, Q.; Zai, J.; Fang, N.; Qian, X., Highly efficient $Ag_2O/Bi2O_2CO_3$ *p-n* heterojunction photocatalysts with improved visible-light responsive activity. *ACS Appl. Mater. Interfaces* **2014,** *6*, 11698-11705.

219. He, Z.; Shi, Y.; Gao, C.; Wen, L.; Chen, J.; Song, S., $BiOCl/BiVO_4$ *p–n* heterojunction with enhanced photocatalytic activity under visible-light irradiation. *J. Phys. Chem. C* **2013,** *118*, 389-398.

220. Wang, J.-C.; Yao, H.-C.; Fan, Z.-Y.; Zhang, L.; Wang, J.-S.; Zang, S.-Q.; Li, Z.-J., Indirect Z-scheme $BiOI/g-C_3N_4$ photocatalysts with enhanced photoreduction CO_2 activity under visible light irradiation. *ACS Appl. Mater. Interfaces* **2016,** *8*, 3765-3775.

VITA

Ruixin Zhou

Educational Institutions Attended and Degrees Awarded

- Murray State University (U.S.A.)   2008–2011
    - *Master of Science in Chemistry*

- Harbin Medical University (China)   2003–2007
    - *Bachelor of Pharmacy*

Professional Positions at the University of Kentucky

- Teaching Assistant for:
    - Analytical Chemistry (Fall 2014, 2015, 201, and Spring 2014 and 2016)
    - General Chemistry Lab 1(Fall 2012 and 2013)
    - General Chemistry Lab 2 (Fall 2011and Spring 2012)

- Research Assistant   2012-2017

Scholastic and Professional Honors

- Research Challenge Trust Fund Fellowship, University of Kentucky, 2016 – 2017.
- Research Challenge Trust Fund Fellowship, University of Kentucky, 2015 – 2016.
- Outstanding Teaching Assistant Award, Department of Chemistry, University of Kentucky, 2016.
- Global Outreach Scholarship, Murray State University, 2008 –2011.
- Co-mentored the research experience of two undergraduate students (Michele Kuceki 2015 and Kayvon Ghayoumi 2015-2016).
- Designed and demonstrated the chromatographic separation of extracted chromophores at Science Summer Camp for middle school students, Lexington, KY. August 2013 and July 2014.
- Designed and demonstrated the use of dyes as colorants at Winburn's Science Night for 6-8 grade students. Winburn Middle School, Lexington, KY. January 23, 2014
- Performed low temperature and fluorescent experiments at the National Chemistry Week Demonstration Show, University of Kentucky, Lexington, KY, October, 23, 2013.

Professional Publications

- Aguirre, M. E.; Zhou, R.; Eugene, A. J.; Guzman, M. I.; Grela, M. A.Cu_2O/TiO_2 heterostrucures for CO_2 reduction through a direct Z-scheme: protecting Cu_2O from photocorrosion. A*ppl. Catal. B: Environ.,* **2017**, 217, 485-493.
- Zhou, R.; Basu, K., Hartman, H.; Matocha, C.; Sears, S. K.; Vali, H.; Guzman, M. I. Catalyzed synthesis of zinc clay by prebiotic central metabolites. *Sci. Rep.,* **2017**, *7*, 533.

- Zhou, R.; Guzman, M. I., Photocatalytic reduction of fumarate to succinate on ZnS mineral surfaces. *J. Phys. Chem. C,* **2016,** *120*, 7349-7357.
- Pillar, E. A.; Zhou, R.; Guzman, M. I., Heterogeneous oxidation of catechol. *J. Phys. Chem. A,* **2015,** *119*, 10349-10359.
- Zhou, R.; Guzman, M. I., CO_2 reduction under periodic illumination of ZnS. *J. Phys. Chem. C,* **2014,** *118*, 11649-11656.
- Aguirre, M. E.; **Zhou, R.**; Eugene. A. J.; Guzman, M. I.; Grela. M. A., Poster title: *Protecting Cu_2O from photocorrosion during CO_2 reduction through a direct Z-scheme in Cu_2O/TiO_2 heterostructures.* Ohio Ohotochemical Society (OoPS) Meeting, Oregon, OH, May 19, 2017.
- Aguirre, M. E.; **Zhou, R.**; Eugene. A. J.; Guzman, M. I.; Grela. M. A., Poster title: *Protecting Cu_2O from photocorrosion during CO_2 reduction through a direct Z-scheme in Cu_2O/TiO_2 heterostructures.* Naff Symposium. Lexington, KY. March 31, 2017.
- Aguirre, M. E.; **Zhou, R.**; Eugene. A. J.; Guzman, M. I.; Grela. M. A., Poster title: *Protecting Cu_2O from photocorrosion during CO_2 reduction through a direct Z-scheme in Cu_2O/TiO_2 heterostructures.* 6th Annual Sustainability Forum, University of Kentucky, Lexington, KY. November 20, 2016.
- **Zhou, R.**; Guzman, M. I., Talk title: *Reusable mineral ZnS for photocatalytic reduction of fumarate to succinate.* American Chemical Society Central Regional Meeting. Covington, KY. May 18, 2016.
- **Zhou, R.**; Guzman, M. I., Poster title: *Photocatalytic reduction of fumarate to succinate on ZnS mineral surfaces.* Naff Symposium. Lexington, KY. April 29, 2016.
- **Zhou, R.**; Guzman, M. I., Talk title: *CO_2 reduction under periodic illumination of ZnS.* The International Chemical Congress of Pacific Basin Societies. Honolulu, HI. December 17, 2015.
- **Zhou, R.**; Guzman, M. I., Talk title: *Photocatalytic reduction of fumarate to succinate on ZnS mineral surfaces.* 251th American Chemical Society National Meeting. Boston, MA. August 20, 2015.
- **Zhou, R.**; Guzman, M. I., Poster title: *Photocatalytic reduction of fumarate to succinate on ZnS mineral surfaces.* Kentucky's Established Program to Stimulate Competitive Research Conference. Lexington, KY. May 29, 2015.
- **Zhou, R.**; Guzman, M. I., Poster title: *Photochemical reduction of CO_2 on sphalerite.* Naff Symposium. Lexington, KY. April 25, 2014.
- **Zhou, R.**; Guzman, M. I., Poster title: *Photochemical reduction of CO_2 on sphalerite (ZnS) mineral surfaces.* American Chemical Society Southeastern Regional Meeting. Atlanta, GA. November 6, 2013.
- **Zhou, R.**; Guzman, M. I., Poster title: *Photochemical reduction of CO_2 on sphalerite mineral surfaces.* Naff Symposium. Lexington, KY. April 12, 2013.